Asynchronous Time Difference of Arrival Positioning System and Implementation

by

Shuai He
B.Sc., Shanghai JiaoTong University, 2007
M.Sc., University of Victoria, 2009

A Dissertation Submitted in Partial Fulfillment of the
Requirements for the Degree of

DOCTOR OF PHILOSOPHY

in the Department of Electrical and Computer Engineering

Asynchronous Time Difference of Arrival Positioning System and Implementation

by

Shuai He
B.Sc., Shanghai JiaoTong University, 2007
M.Sc., University of Victoria, 2009

Supervisory Committee

Dr. Xiaodai Dong, Supervisor
(Department of Electrical and Computer Engineering)

Dr. Wu-Sheng Lu, Departmental Member
(Department of Electrical and Computer Engineering)

Dr. Jianping Pan, Outside Member
(Department of Computer Science)

Supervisory Committee

Dr. Xiaodai Dong, Supervisor
(Department of Electrical and Computer Engineering)

Dr. Wu-Sheng Lu, Departmental Member
(Department of Electrical and Computer Engineering)

Dr. Jianping Pan, Outside Member
(Department of Computer Science)

ABSTRACT

In this thesis, a complete localization system using asynchronous time difference of arrival (A-TDOA) technique has been thoroughly studied from concept to implementation. The work spans from a proposal of a new A-TDOA system deployment and modeling, through a derivation of the achievable estimation bound, to estimation algorithms development, to a hardware realization, and ultimately to measurements conducted in realistic radio environments.

The research begins with a new deployment of an A-TDOA localization system. Compared to the conventional time of arrival (TOA) and time difference of arrival (TDOA) systems, it does not require clock synchronization within the network, which enables a flexible and fast deployment. When deployed in the simplest form, it can effectively reduce system complexity and cost, whereas if all anchor nodes are equipped with full transmit and receive capability, the A-TDOA system can achieve superior performance using a novel receiver re-selection technique.

Determining the physical position of a target node in a noisy environment is critical. In this thesis, two novel algorithms, namely, a two-step and a constrained least squares (CLS) algorithms, are proposed offering excellent accuracy and the best trade-off between complexity and precision respectively. The two-step algorithm exploits the advantages of the semi-definite programming (SDP) and the Taylor method, i.e., global convergence and high precision, to achieve superior performance. The CLS algorithm significantly reduces the computation complexity while achieving good accuracy.

Despite extensive research efforts on ranging and localization modeling and simulation, knowledge about practical implementations is limited. For the first time, a complete prototype based on A-TDOA technique is implemented in hardware. All sub-systems are developed from scratch and undergone significant modifications for improved reliability. The design objective is low cost and low complexity, and therefore a non-coherent receiver architecture was adopted. The target node design is based on receive and re-transmit technique and is prototyped in analog domain to avoid clock offset and skews. The implemented system has been extensively tested in an outdoor and indoor radio environments. The accuracy obtained are 20.7 cm and 15.2 cm respectively. Comparison with the literature published up to date proves the excellent quality of the design and implementation. To better understand the localization accuracy, the error sources due to thermal noise, hardware limitation, radio propagation channel and clock jitter are identified and investigated. Mitigation methods are proposed to reduce errors.

Contents

List of Tables

List of Figures

ACKNOWLEDGEMENTS

I am deeply grateful to my supervisor, Prof. Xiaodai Dong. She is an outstanding researcher with broad knowledge, sharp intuition, and grand vision. Prof. Dong is also a great mentor. She is very patient and gives me lots of freedom to explore the field by myself. Under her guidance, I was able to learn the fundamental lessons of being a researcher: finding valuable problems, investigating innovative ideas and presenting meaningful results. Her inspiration and warm personality have won my highest respect and trust.

I would like to specially thank Prof. Wu-Sheng Lu, for his inspiration and enlightening discussions on a wide variety of topics. His invaluable insight on my research work has helped me make significant improvements on this dissertation work. He is very attentive, responsive, always has the best interests of his students at heart.

I also feel very grateful to other committee members, Prof. Jianping Pan, and Prof. Hai Lin. I thank them for serving on my qualifying exam and dissertation committees. Their suggestions have greatly improved my dissertation work.

Most importantly, none of this would have been possible without the unwavering support from my family. In spite of being separated by the vast Pacific Ocean, my parents have always inspired me with courage, strength and love. My dearest wife has shared with me all the sweets and bitters of life here, and has never failed to believe in me. I feel exceptionally favored to have you. Last but not the least, I would like to dedicate this Ph.D. thesis to my lovely child, He Yi, who is the pride and joy of my life.

He Shuai

DEDICATION

To my beloved family.

Chapter 1

Introduction

As far as outdoor localization is concerned, Global Positioning System (GPS) is arguably the most widely used technology. The GPS is a space-based navigation system that provides location and time information to anywhere on or near the Earth where there is an unobstructed line of sight to four or more GPS satellites. It can typically provide good location estimation within a few meters. However, in indoor and dense urban environments, localization has always been a more challenging problem for several reasons. First of all, the GPS signal is usually not strong enough to penetrate concretes which are the basic building materials for most buildings, making it almost completely useless in an indoor environment. Secondly, in a dense urban environment, due to the blockage of the direct line of sight (LOS) signal from the GPS satellite, the signal is significantly corrupted which constrains its usefulness to open environments. Thirdly, the GPS accuracy is typically on the order of meters, whereas in applications where objects or human beings need to be tracked relatively accurately, the GPS may lead to erroneous subsequent decisions which can cause dreadful disaster.

Position information brings enormous benefits to many real-life applications ranging from cargo tracking, tourist guiding, emergency evacuation, to countless usage scenarios. As mobile devices become ubiquitous, contextual awareness applications have become popular and the indoor positioning system (IPS) has gained significant attention. IPS locates people or objects inside a building using various technologies, such as radio waves, magnetic fields, acoustic signals or other sensory information collected by a smart phone device or a specific mobile device. In order to illustrate this better, let us consider a few application examples benefiting from using a high accuracy localization system.

- Example 1: Museum and airport navigation

  A mobile multimedia guide system can be deployed to offer detailed background information based on the current location of the user. The mobile device calculates continuously the visitor position and displays the current location as well as surrounding exhibition information. The visitor can then choose which exhibits one would like to learn more about. With the IPS, the visitor always remains in control and can explore the exhibition according to his or her own interests.

  Similar idea applies to airport navigations. Based on their current position, travelers know how long it would take to walk to the gate, and how to reach the gate. In addition, the airport can monitor the mobile traffic for crowd control, staff management and alerts, and the airlines can locate passengers giving them a push notification to start walking towards the gate just in time to prevent delays.

- Example 2: Operation optimization

  Imagine a twenty storey building where employees could be anywhere. For such an environment indoor positioning might be the only way to keep operations running smoothly: find a free meeting room, find free workspaces, find your colleague, and get the estimated arrival time on a colleague that is running late and so on. A company can also look into the behavior of their employees to improve the work environment and discover what places in the office are used the most and which areas are rarely used to optimize the space.

- Example 3: Emergency evacuation and rescue

  During an emergency event such as earthquake, fire or tornado, rescuers need to know how many people are affected and exactly where they are located. Simply knowing there are many shoppers in a mall or travelers in an airport is not enough; in an emergency, real-time information on precisely where in the building each individual is situated can make a life-or-death difference. With location information, more risk can be eliminated as people can be guided or directed through safe passageways to reach shelter or to exit the facility. In a situation such as a chemical spill when the facility needs to be vacated, there is a huge value in knowing if anyone is still inside the building, who and where

they are, and who has safely evacuated, along with the ability to help those who need guidance in finding a safe way out.

1.1 Localization Basics

Localization generally requires several objects with known locations (anchors) and distance or angle measurements between these anchors and the object to be localized (target node). Anchors may be placed at fixed locations and their coordinates may have been pre-configured, or they may have special hardware to learn their locations from a location server, such as the GPS.

For estimating the location of an unknown node, traditional localization methods generally use distance or angle measurements between the anchor and the target node or a combination of the two measurements. Two well-known localization techniques are angulation and lateration. Angulation locates an object by computing angles relative to multiple reference points, whereas lateration estimates the position of an object by measuring its distances from multiple reference points. Lateration is widely used in various localization systems and is also employed by the GPS system.

In a localization system, angle and distance measurements are usually collected by one of the following methods:

- Received Signal Strength (RSS)
- Angle of Arrival (AOA)
- Time of Arrival (TOA)
- Time Difference of Arrival (TDOA)
- Two-way Ranging

The details of these methods are presented in Section 2.1 and here we only provide a brief introduction. The RSS method is based on converting the propagation loss, which is the difference between the transmitted and the received signal power, into a distance estimate. RSS assumes the propagation property of the medium is already known. The AOA method measures the angle between the propagation path of the signal and a reference direction. The TDOA method uses the time difference between the arrival of two signals and the TOA approach calculates the distance between anchor and target nodes.

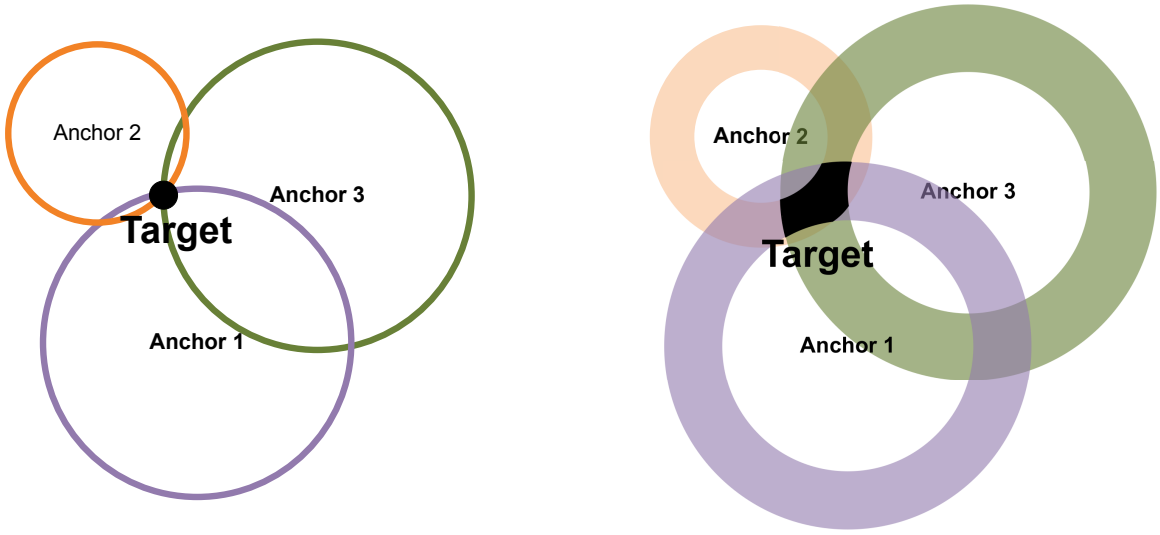

Figure 1.1: A positioning system with (left) and without (right) measurement error.

Due to the imperfect implementation of location sensing systems, lack of bandwidth, thermal noise and interference, multipath of the radio propagation channel and the drift of the clocks, there are always errors associated with measurements of location related metrics. Fig. 1.1 gives a simple example demonstrating a positioning system with and without measurement error. When there is no measurement error, an object can be uniquely identified at the intersecting point of three circles, which are determined by three reference points with known coordinates and distance from its position to the target. Whereas if the distance measurement is erroneous, rather than the target being located at a single point at the intersection of the circles, it can be located anywhere in the dark shaded region.

To obtain an estimate of target location in the presence of measurement errors, a variety of direct and iterative positioning algorithms have been developed. These algorithms solve the problem by formulating a localization problem into a set of nonlinear equations. There are mainly two types of estimators that can be used to solve the nonlinear equations: one is linear and the other is nonlinear. The linear approach converts the problem into a set of linear equations, so that least squares technique can be applied. The implementation complexity is low and global convergence is ensured. The nonlinear approach directly solves the problem using nonlinear least squares (NLS) or maximum likelihood (ML) estimators. Optimum estimation performance can be obtained; however, sufficiently precise initial estimates are required for global convergence [1]. Chapter 4 provides great details of the commonly used

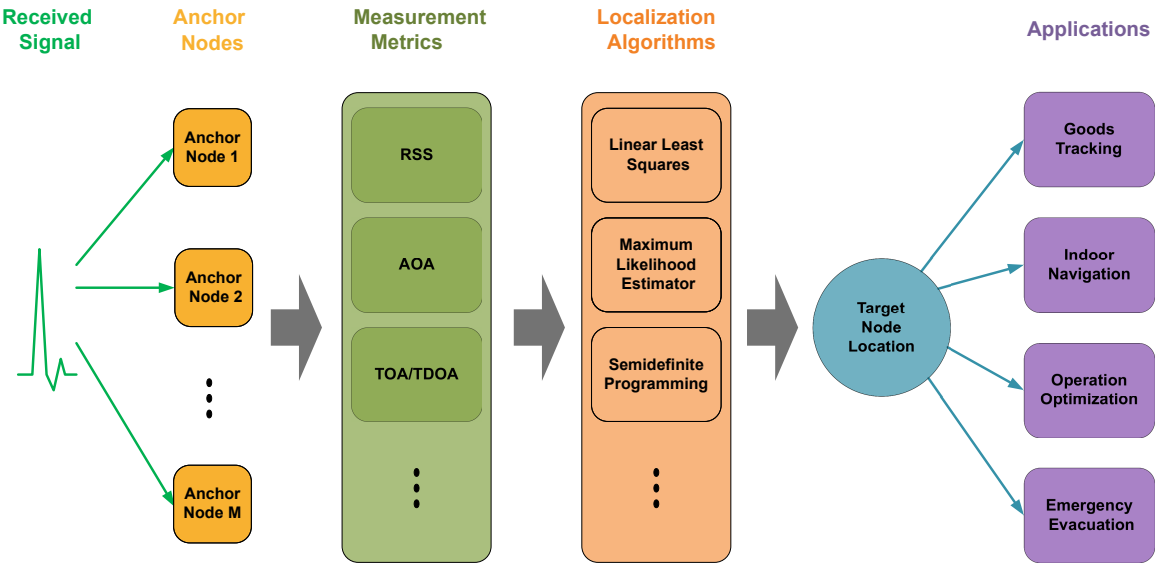

Figure 1.2: Functional block diagram of a wireless localization system.

estimators.

Fig. 1.2 illustrates the functional block diagram of a wireless localization system. The main elements of the system are a number of location sensing devices that measure metrics related to the relative position of a target node with respect to a known anchor node, and a positioning algorithm that processes metrics reported by location sensing elements to estimate the location coordinates of a target node. The location metrics may indicate the approximate AOA of the signal or the approximate distance derived by RSS, TOA and TDOA measurements between a target node and anchor nodes. The estimated target node location can then be used as an input to many high level networking tasks and applications.

1.2 Motivations

There are many applications that can benefit from accurate positioning that are not supported by current technologies such as GPS. Examples include assets tracking in warehouses, emergency services such as firefighter tracking and evacuation navigation, as well as robotic mapping and etc. These applications strongly affect requirements in designing an accurate localization system: low cost and low power consumption are compulsory. It must be low cost mainly due the large volume of the tags to be deployed, and must be low power consumption so that the battery operated tags

can operate hours to days. Among these applications, the emergency service is the most challenging. An emergency happens unexpectedly and needs immediate action to minimize the loss of life and property. Accurate information from the emergency site is very essential in order to successfully execute any response or rescue operation. Therefore, rapid and post deployment of a localization system is extremely important and necessary. This drives an additional design challenge, i.e., asynchronous network and wireless backbone infrastructure.

In the literature, substantial research on wireless location techniques has been presented. However, not as much research pertaining to localization in an asynchronous network has been conducted, and even less on the practical implementation and evaluation of a real system in a real environment.

Traditional TOA localization systems demonstrated that high accuracy can be achieved with perfectly synchronized clocks among anchor and target nodes. However, high accuracy clock synchronization is extremely challenging especially in a wireless network. Oscillators with low jitter and high frequency stability can be used in the target and anchor nodes to minimize clock jitter and drifting, yet it typically is costly, power consuming, and physically large. For example, an oven controlled crystal oscillator (OCXO) achieves the best frequency stability possible from a crystal, and the short term frequency stability is typically $1e^{-12}$ over a few seconds, while the long term stability is limited to around $1e^{-8}$ per year due to aging. Converting frequency accuracy to time, in one hour, the OCXO drifts about 3.6 ns which is on the same order of an high accuracy localization system's allowable error (1 ns timing error causes about 30 cm ranging error). If we consider one year, it drifts about 315 ms which is too much to be useful for an RF based localization system. To take advantage of the short term stability offered by an OCXO, the target and anchor nodes clocks must be calibrated (synchronized) before each use, which makes it highly impractical. In addition, an OCXO consumes 1 to 3 W of power and weights 200 to 500 grams, which prevents it from being powered by a portable battery pack.

To relax the clock synchronization difficulty of a target-anchor node pair in an TOA system, the TDOA localization system is introduced. It, however, comes along with a requirement to establish a wired infrastructure providing synchronous clocks to all the anchor nodes. This characteristic makes the TDOA localization system feasible in a static environment where wired anchor are installed to fixed positions and untouched thereafter. Nonetheless, it cannot be rapidly deployed to a new environment if an emergency occurs.

Two-way ranging technique avoids all clock synchronizations which makes it very practical to use. In a two-way ranging system, an anchor node transmits a packet to a target node, which replies by an acknowledgment packet to the anchor node after a response delay τ_d. The round trip time (RTT) at the anchor node is then determined by $\tau_{RTT} = 2 \cdot \tau_p + \tau_d$, where τ_p is the propagation delay that directly relates to the ranging between the two nodes. The two-way ranging eliminates the error due to imperfect synchronization between nodes, yet this approach is sensitive to clock non-idealities as pointed out in [2] and [3]. Propagation delay is typically on the order of tens of ns while the response delay can be of a few microseconds due to bit synchronization and channel estimation delays. Therefore a small clock offset between the target and anchor nodes could cause a large error due to τ_d. Generally, the further down in the communication protocol stack to draw the response delay, the smaller the time variation.

After extensively studied the existing wireless localization techniques and the implemented prototypes available, we have decided to develop a complete asynchronous time difference of arrival (A-TDOA) localization system which offers the following features:

- Asynchronous: no clock synchronization required among target and anchor nodes.
- Fast and post deployment: system can be deployed whenever and wherever needed.
- High accuracy: sub-meter accuracy can be achieved in real radio environments.
- Low cost and low power consumption: large amount of battery operated tags can be deployed.

These features enable the A-TDOA localization system to fulfill the requirement of many location aware applications, including the emergency service that most systems cannot support.

It is important to emphasize that to achieve the goal of developing a complete system offering above features, we take a top-down systematic methodology to first develop an A-TDOA localization system model, then theoretically study the limits (the best accuracy it can offer). After that, we derive two estimation algorithms tailored for A-TDOA system. Subsequently, a prototype was implemented from scratch

and undergone extensive modification and improvement, following which experiments were conducted and performance was evaluated in real radio environments. Ultimately and most importantly, we analyze the error sources in retrospect, and provide mitigation approaches for future improvement.

1.3 Contributions

This research work made valuable contributions to a new asynchronous TDOA localization system, from concept to implementation. The main contributions are summarized below.

- Proposed a new A-TDOA localization scheme.

  We have proposed a new A-TDOA localization scheme that avoids clock synchronization requirement. The A-TDOA technique neither requires clock synchronization between target and anchor nodes nor wired infrastructure among anchor nodes, which are necessary for TOA and TDOA systems respectively. This greatly simplifies the system deployment and can be widely used in the sensor network based localization systems. In addition, it supports rapid and post deployment of a localization system such that it can be readily usable in an emergency situation. Finally, we have also proposed a receiver re-selection technique that can significantly improve the estimation accuracy.

- Derived a distance dependent Cramer-Rao lower bound (CRLB) for the A-TDOA system.

  A practical CRLB has been derived for the A-TDOA system. The CRLB is useful for comparing the fundamental performance of different localization techniques. It also serves as a benchmark to evaluate an estimator's accuracy. We model the received signal's signal to noise ratio (SNR) as a distance dependent parameter to derive a more accurate and more practical lower bound for the A-TDOA system, as well as the conventional TOA and TDOA systems.

- Proposed a two-step (SDP + Taylor) algorithm and a constrained linear squares (CLS) algorithm to estimate the target position in the A-TDOA system.

  Two novel location estimators are proposed to achieve superior estimation performance and low complexity respectively. The two-step algorithm combines

the SDP method and the Taylor method to ensure the global convergence and achieve superior accuracy. The two-step estimator can be applied in applications where accuracy is the most critical. The CLS algorithm obtains relatively good performance while keeps the computational complexity low, also the convergence speed is fast. These properties are very useful in real-time systems and mobile devices where battery life and computational capability is limited. Extensive simulation has been conducted to demonstrate that both estimators are robust regardless of the target node location and the measurement error magnitude.

- Implemented an A-TDOA system prototype, and conducted extensive measurements to evaluate the performance.

  A prototype has been developed for the A-TDOA system with a low cost and low power consumption architecture. The complete design include anchor Tx, anchor Rx, target, as well as an ultra-wide bandwidth antenna. The prototype has been built from scratch using discrete components, and has undergone great amount of modification and optimizations. The implemented prototype was evaluated in different radio environments, and a good positioning accuracy is achieved. Most importantly, localization errors due to thermal noise, hardware limitation, and radio propagation channel are investigated, and mitigation methods are proposed to further improve the performance.

1.4 Notations

The notation used in this thesis is described as follows. Bold upper case symbols denote matrices and bold lower case symbols denote vectors. The $\mathbf{0}_{m\times n}$ is the $m \times n$ zero matrix, $\mathbf{I}_m$ is the $m \times m$ identity matrix. $(\cdot)^T$ denotes vector transpose operator and $\|\mathbf{x}\|$ represents the 2-norm of a vector $\mathbf{x}$. For two symmetric matrices $\mathbf{A}$ and $\mathbf{B}$, $\mathbf{A} \succeq \mathbf{B}$ means that $\mathbf{A} - \mathbf{B}$ is positive semidefinite. Let $\mathbf{x} = [x, y]^T$ and $\mathbf{x}_i = [x_i, y_i]^T, i = 1, 2, \cdots, M$ be the coordinate of the target node and anchor nodes respectively. M is the number of anchor nodes with $M \geq 3$ for two dimensional positioning.

1.5 Organization of the Manuscript

The rest of the thesis is organized as follows.

Chapter 2 provides an overview of the commonly used conventional localization methods, and presents a new asynchronous TDOA localization system model.

Chapter 3 concentrates on the estimation bounds of the TOA, TDOA and A-TDOA localization systems. The trade-offs between synchronization requirement and accuracy performance are studied and demonstrated through Cramer-rao lower bound.

Chapter 4 introduces two new position estimation algorithms designed for the A-TDOA localization system. One is a two-step algorithm that combines the SDP and Taylor method to achieve global convergence as well as superior accuracy, and the other is a CLS method that has low complexity and fast convergence while maintaining good performance. Simulation results under different ranging error conditions are presented to showcase the excellent performance of the two new algorithms.

Chapter 5 presents an A-TDOA localization platform and experimentally characterized performance in a variety of radio environments. The platform is developed from scratch and undergone significant updates for improved reliability. In addition, the error source due to noise, hardware limitation and radio propagation channel are studied and mitigation methods are provided.

Finally, Chapter 6 provides concluding remarks and an outlook on future research directions.

Chapter 2

Localization Techniques

As introduced in Chapter 1, there are three basic properties that enable distance and direction measurement from the analysis of specific physical characteristics of radio signals: received signal strength, angle of arrival, and time of arrival (TOA/TDOA/two-way ranging) [4]. A classification of these methods is summarized in Fig. 2.1. Note that this classification does not prevent designs using hybrid measurements for better accuracy performance and system flexibility [5]. In this Chapter, a detailed description of these conventional methods is first provided, followed by an introduction to the new asynchronous TDOA localization system.

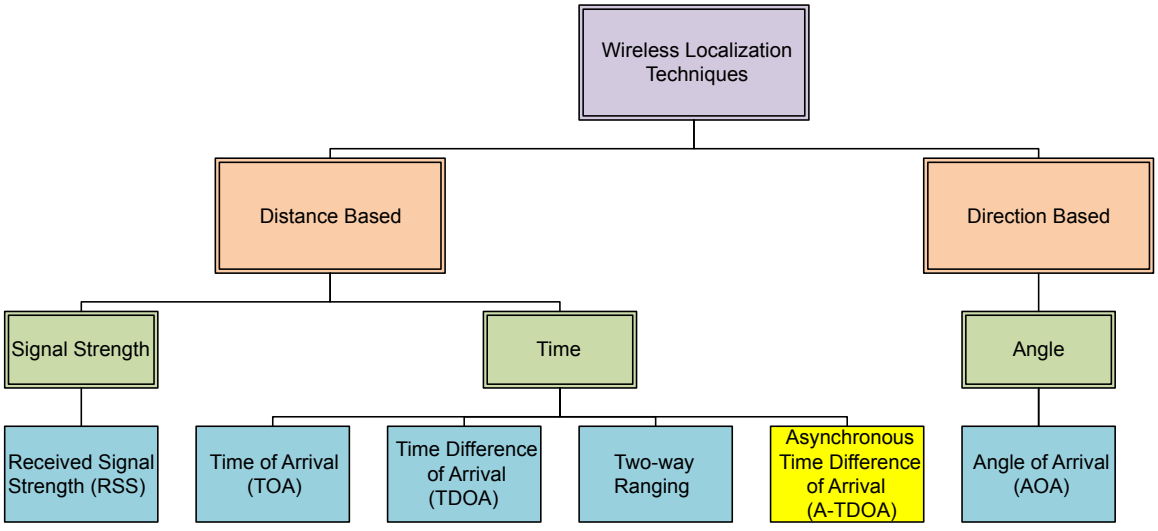

Figure 2.1: Classification of the wireless localization techniques.

2.1 Conventional Localization Methods

The conventional localization system designs are mostly based on point-to-point distance and angle measurements to identify nodes' coordinates. In the following subsections, we provide a detailed introduction and literature review of the commonly used localization methods, including:

- Received Signal Strength
- Time of Arrival
- Time Difference of Arrival
- Two-way Ranging
- Angle of Arrival

2.1.1 Received Signal Strength Systems

As the distance of a radio link increases, the received signal strength will reduce correspondingly. In free space, the received signal power is determined by

$$P(d) = P_0 - 20\log_{10}\frac{d}{d_0}, \tag{2.1}$$

where P_0 is the received power (in dBm) at a short reference distance d_0, and d is the distance between the transmit and the receive device. Such relationship conveys information about the range between an anchor node and a target node and can therefore be used in a localization system [6–10].

Since many consumer electronic devices have the ability to measure received signal power, the RSS based localization system becomes an economic solution because the existing infrastructure can be reused easily [11–13]. However, ranging accuracy of the RSS technique is highly dependent on the channel parameters and the distance between the two nodes. The indoor wireless channel is extremely complicated, which can cause significant fluctuations in RSS even over short distance. Therefore it is difficult to infer distance from RSS without a detailed model of the physical environment. To overcome the uncertainty of RSS, widely observed statistic model is applied to describe radio propagation path loss. In [14], the amended received signal strength

is related to the distance d with

$$P(d) = P_0 - 10 \cdot \beta \cdot \log_{10}\frac{d}{d_0}, \tag{2.2}$$

where β is the radio path-loss factor (also called the fading factor or attenuation), typically between 2 and 6.

2.1.2 Time of Arrival Systems

Different from the RSS and AOA method, time based localization method, including TOA, TDOA and two-way TOA ranging, is able to exploit the fine delay resolution property of a wideband signal and has the greatest potential for providing high accuracy location estimation.

Many high-accuracy localization systems rely on time of arrival measurements of RF signals to achieve precise ranging [15–20]. The methodology is simple: given the signal propagation speed, the elapsed time from signal emitter to a receiver indicates the distance between them. However, in order to obtain a TOA measurement, it is required that the anchors and target are precisely synchronized [18]. That is, the anchor node needs to know the exact time stamp when the signal is sent from the target node. Assume at time t_0 a pulse is emitted from the target node, and at time t_i, it is received by one of the anchor nodes. The distance between the two can be calculated by $d = c \times (t_i - t_0)$, where c is the speed of light. This equation can also be written as

$$\|\mathbf{x} - \mathbf{x}_i\| = c \cdot (t_i - t_0)\,, \text{ for all } i \in \{1, 2, 3, ...\} \tag{2.3}$$

Geometrically, eq. (2.3) represents several circles with their center at x_i and radii of $c \cdot (t_i - t_0)$. It is obvious that with three anchor nodes, the target node can be located at the intersection of the three circles. Fig. 2.2 shows a simple geometric arrangement for determining the location of a target node, which is located on the same two dimension plane as anchor nodes 1, 2 and 3. The coordinates of anchor nodes are known in advance, and the distances between the target node and anchor nodes are found by multiplying the measured signal propagation time between each anchor node and the target by the speed of light. Solving (2.3), we can obtain the coordinate of the target node easily. However, distance measurements are subject to various causes of imprecision, among them noise, channel interference, multipath, and imprecise clocks. These imprecision can result in that the circles do not cross at one point. Therefore,

it is necessary to apply signal processing methods to decide the estimated location coordinates. The algorithms to estimate the target node coordinates will be described in detail in Chapter 4.

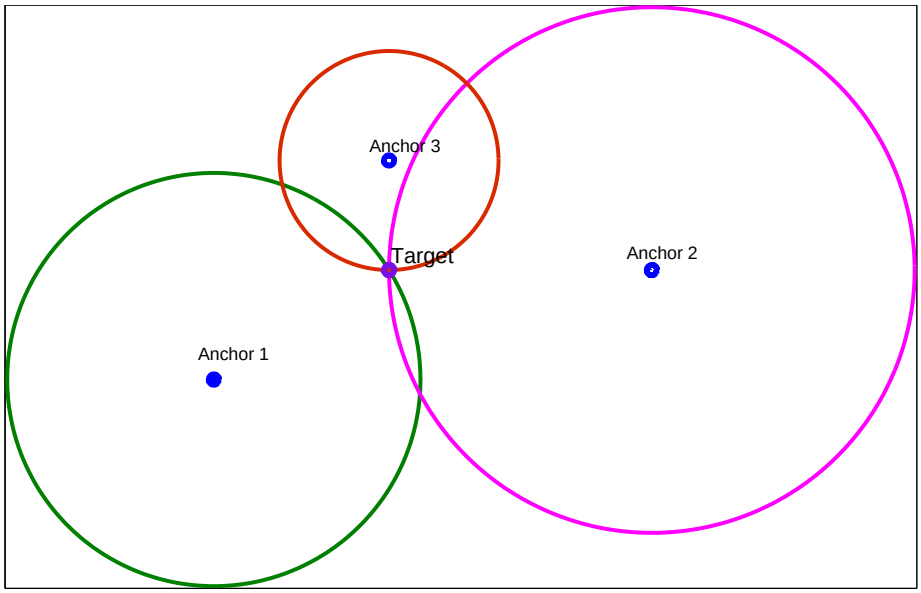

Figure 2.2: An example of a TOA positioning system.

Conceptually simple, measuring TOA for radio signals is extremely challenging in several aspects.

- The extremely fast speed of light.
- The relatively short distance among sensor nodes in a network.
- The hardware constraints of sensor nodes that prohibits timing with ultra-high resolution.
- The stringent requirement on clock frequency and phase synchronization between anchor and target nodes.

The time domain resolution of the signal determines the localization accuracy of the system. Two mostly used technologies for TOA systems are ultra wideband (UWB) [21] impulse and direct-sequence spread spectrum (DSSS) [22], both of which have very fine time resolution. The DSSS technology is widely used in GPS for many years [23]. The UWB systems, with bandwidth of more than 500 MHz, have attracted considerable attention especially for indoor localization applications in recent years

[24]. It has been shown that the UWB signal is not seriously affected by multipath fading [24], which is because of the narrow pulse shape in the time domain that allows differentiation among delayed replicas as shown in Fig. 2.3. From this figure, we can observe that the signal peak can be clearly identified along the time line. However, integrating such a system on sensor nodes is quite challenging, because it demands highly sophisticated hardware and software designs to provide accurate edge detection and precise timing.

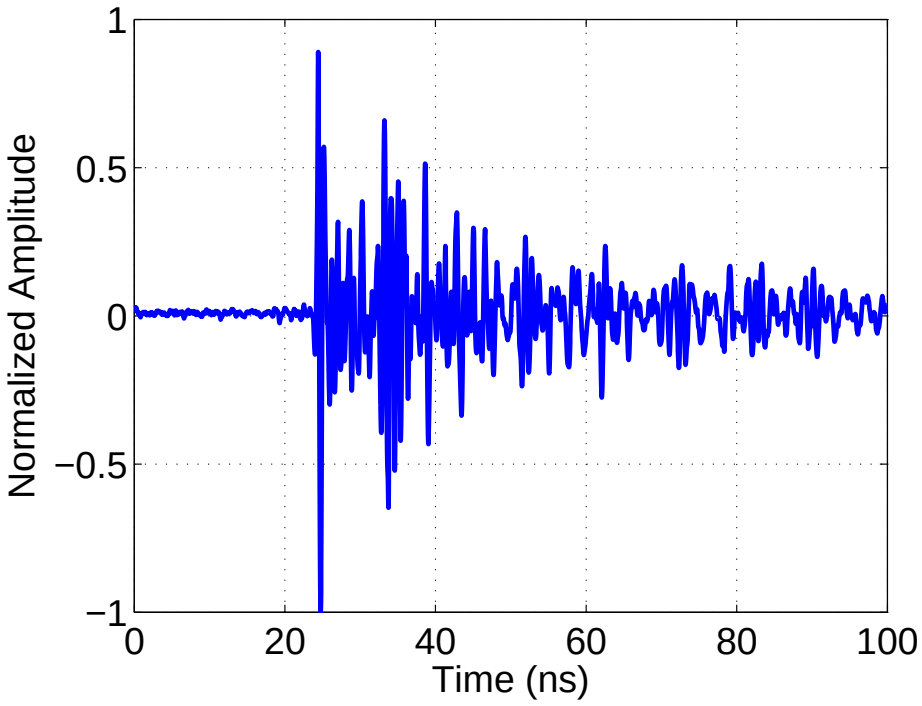

Figure 2.3: An example of an UWB signal.

2.1.3 Time Difference of Arrival Systems

Instead of measuring the time of flight of a transmission between a target node and an anchor node, TDOA measures the difference in the times of flight between a target node and a pair of fixed anchor nodes [25–30]. Clock synchronization is required only on the anchor nodes side. The TDOA system needs at least three fixed terminals for a two-dimensional location problem and at least four fixed terminals to estimate three-dimensional coordinates.

The target node transmits a pulse at time instant t_0 that is received at anchor

node 1 at t_1, at anchor node 2 at t_2, and at anchor node i at t_i. The clocks of anchor nodes are synchronized, but not the target node clock. Thus, t_0 is unknown to the anchor nodes. The time difference of arrival, namely $(t_2 - t_1)$, $(t_3 - t_2)$ and so on can be measured and the difference of the distances between any two anchor nodes and the target can be written as

$$\|\mathbf{x} - \mathbf{x}_i\| - \|\mathbf{x} - \mathbf{x}_j\| = c \cdot (t_i - t_j)\,, \text{ for all } i, j \in \{1, 2, 3, ...\}\,, \text{ and } i \neq j. \tag{2.4}$$

It can be seen from (2.4) that the locus of points has a constant difference from the two foci, anchor node i and j, and this describes a hyperbola. The geometric model for estimating position coordinates using TDOA is the intersection of hyperbolas, in two dimensions, and the intersection of hyperboloids in three dimensions. This is shown in Fig. 2.4.

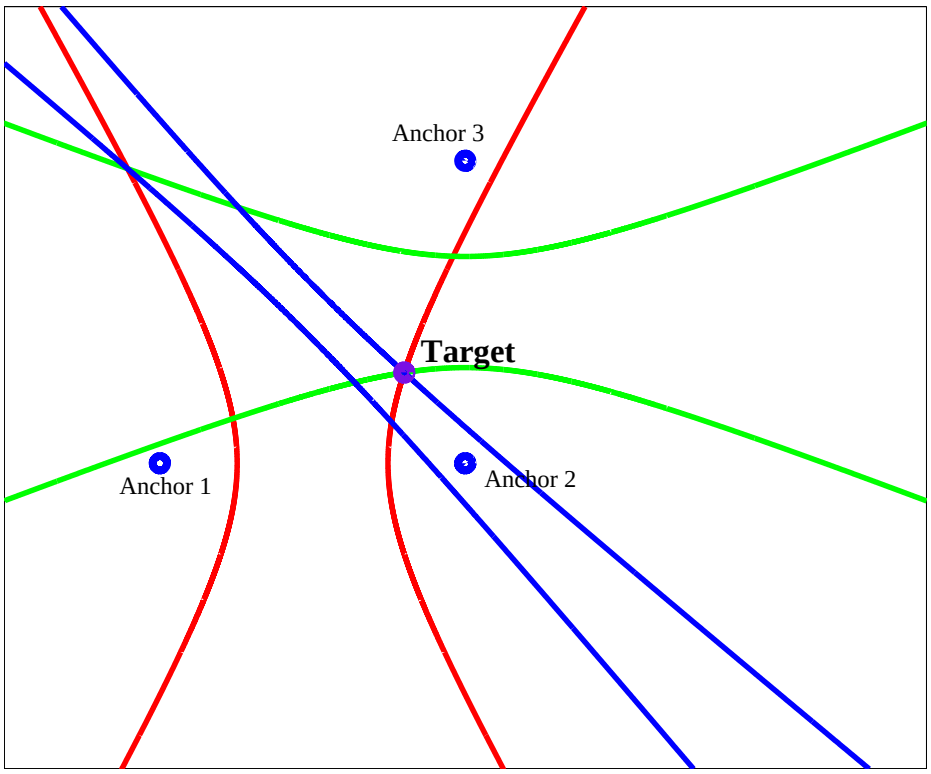

Figure 2.4: An example of a TDOA positioning system.

The total number of TDOA measurements, K, obtainable from M anchor nodes is

$$K = \frac{M!}{2 \cdot (M-2)!}. \tag{2.5}$$

The number of independent TDOA measurements obtainable from M anchor nodes is $M-1$. All of the independent values in a set are based on at least one measurement of time of arrival between an anchor node and target that is not used in any other measurement in the set. It is often considered sufficient to include only the independent TDOA in the location estimation process [31]. However, in a noisy environment additional pairs of measurements that are not independent according to the above criterion may be added for redundancy, since the noise that is not correlated between those pairs gives them a degree of independence [32].

2.1.4 Two-way Ranging Systems

The TOA method demands perfect synchronization between anchor and target nodes, which is not practical in real networks. In order to avoid the impact of imperfect synchronization, the two-way ranging method is also commonly used [33–36]. The two-way ranging has been standardized in IEEE 802.15.4a [37] which is an amendment to IEEE 802.15.4 to provide high precision ranging and positioning capability. In two-way ranging, the system estimates the signal round-trip time (RTT) without a common clock source, as shown in Fig. 2.5.

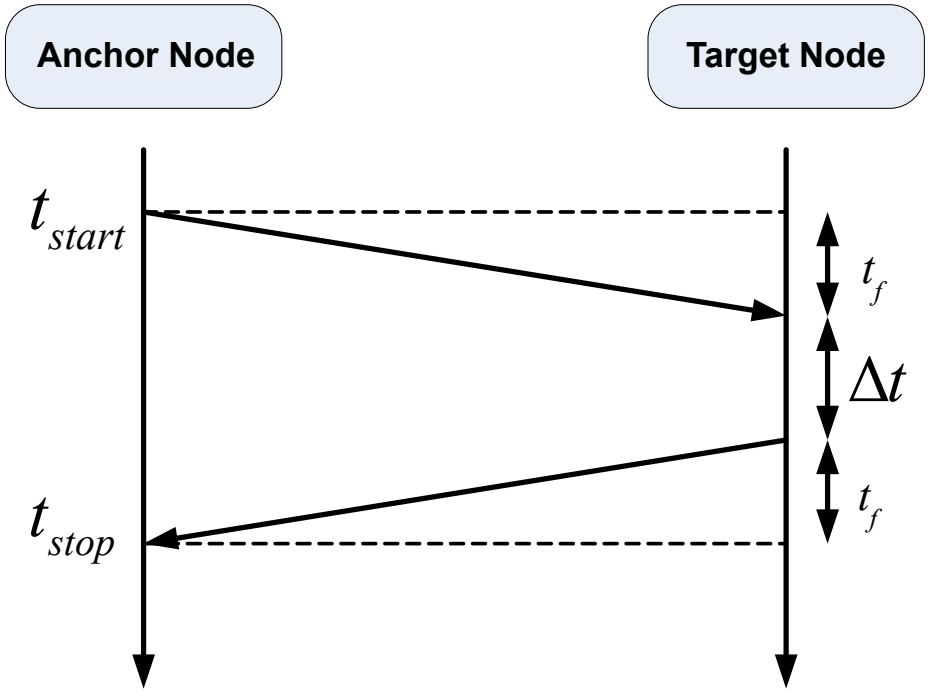

Figure 2.5: Two-way ranging scheme.

The two-way ranging technique requires the anchor and target nodes to exchange at least two packets. In Fig. 2.5, the anchor node starts a ranging measurement by sending a ranging packet to target node at time t_{start}. The target node receives the packet from anchor node, and replies with a second packet, after a known delay Δt. The packet is then received by anchor node at time t_{stop}. Then the distance between anchor and target can be calculated as:

$$d = \frac{t_{stop} - t_{start} - \Delta t}{2} \cdot c, \tag{2.6}$$

where c is the speed of light.

Although the two-way ranging method greatly relaxes the synchronization requirement between an anchor and target node, it still faces challenges of target node timing resolution. The processing delay in a target node is usually on the order of micro-seconds while the time of flight between two nodes is on the order of nano-seconds. Therefore slight clock drift on the target node can cause dramatic timing error. This requires the target node to be equipped with high speed and high accuracy clocks and processors [38].

2.1.5 Angle of Arrival Systems

Apart from using distance estimates, angular estimates can also be used in a localization system [39–43]. The angle of arrival data are typically gathered using antenna arrays [44], which allows a receiver to determine the direction of a transmitter. At the concept level, AOA is not a new idea. Phased array radars and smart antennas, which function based on the AOA methodology, have been widely used in military and civil applications [45, 46]. However, the use of AOA for localization in wireless networks is not a trivial "technology transfer" when considered from the perspective of a practical system. This is because angles are simply much harder and more expensive to measure than distance for sensor nodes with tremendous constraints in cost, form factor and energy. For example, the need of spatial separation between antennas is difficult to be accommodated in small sized nodes. The advantage though, is that it does not require cooperation with the target nor stringent receiver timing.

To perform localization with AOA, the angles between sensor nodes and multiple anchors are measured. Given the position information of anchors, sensor nodes' location coordinates can be easily calculated with geometrical methods. Detailed de-

scriptions about the basics of AOA-based localization in wireless sensor networks can be found in [47].

The accuracy of AOA measurements is affected by a combination of factors, including the directivity of signal emitter and receiver, multi-path reflections, background noise, and etc [24]. Many AOA designs depend on a LOS path from the transmitter to the receiver [47]. Furthermore, a multipath component may appear as a signal arriving from an entirely different direction, leading to large errors in angle estimation. To overcome those difficulties, researchers have investigated many robust designs that help to reduce AOA measurement noise as well as its impact to localization results [48, 49].

2.2 Asynchronous Time Difference of Arrival Systems

The TOA and TDOA methods exploit the fine delay resolution property of wideband signals and has great potential for providing high accuracy location estimation. However, both methods face a major challenge, that is, synchronization is required among the clocks of the involved nodes with a timing accuracy proportional to the desired localization precision. Efforts have been made in the literature to relax the synchronization requirements, and two common methods are two-way ranging and elliptical localization [50–52].

The elliptical localization system starts with an anchor transmitter (Tx) emitting a pulse, and upon arrival, the pulse is re-transmitted by the target node. An anchor receiver (Rx) captures two pulses in a row, one from the anchor Tx and the other from the target. The time difference between the two received signals can be measured, and together with the knowledge of the anchor Tx and Rx positions, the sum of the distances between the target and the two anchor nodes can be calculated. Hence, the target node lies on the trajectory of an ellipse with anchor Tx and anchor Rx as the two foci. Several elliptical localization systems have been studied in the literature [50–52]. These systems work in a similar manner and they differ in one or two respects. The system deployment in [50] has a designated anchor Tx emitting an ultra-wideband pulse, and three anchor Rx nodes to perform the time difference arrival measurements. Wang *et al.* [51] proposed an asymmetric trip ranging protocol and the system deployment is similar to [50] but it involves a timing logic at the

target node, which suffers from clock non-idealities. In [52], a distributed localization scheme is proposed, and it uses the target node to measure the TDOA. Due to the cost and power constraints on the target node, low-performance clocks are normally employed which limits the accuracy. In this section, we present a new elliptical localization system, namely, an A-TDOA positioning system. The A-TDOA system's deployment is different from [50] in that there is no need for a designated anchor Tx. Rather, the proposed simplest deployment contains one anchor Rx and three anchor Tx. A more comprehensive setup contains four transceiver anchors, each of which can be dynamically configured into a Tx or Rx in order to minimize estimation error by performing novel receiver re-selection.

An A-TDOA localization system consists of a number of nodes. The anchor node that initiates the pulse transmission is called anchor Tx, and the one that receives the pulse is called anchor Rx. In an A-TDOA system, there are multiple anchor Tx nodes and one anchor Rx node. Let $\mathbf{x} = [x, y]^T$ and $\mathbf{x}_i = [x_i, y_i]^T, i = 1, 2, ..., M$ be the coordinates of the target node and anchor nodes respectively, where M is the number of anchor nodes with $M \geq 3$ for two dimensional positioning. Without loss of generality, let anchor Rx be at $\mathbf{x_1}$, and anchor Tx be positioned at $\mathbf{x_i}$, $i = 2, 3, ..., M$.

Fig. 2.6 demonstrates the signal flow and the system timing. At time t_{AT}, anchor Tx transmits a pulse that is received at the target node at time t_{TR} and at anchor Rx at time t_{ARD}. As soon as the target node receives the pulse from anchor Tx, it retransmits it immediately. The retransmitted signal then reaches anchor Rx at time t_{ARR}. Ultimately, anchor Rx will receive two pulses in a row: one is from anchor Tx and the other is from the target node.

The time difference measured at anchor Rx can be written as

$$(t_{ARR} - t_{ARD}) \cdot c = \|\mathbf{x} - \mathbf{x}_i\| + \|\mathbf{x} - \mathbf{x}_1\| - \|\mathbf{x}_i - \mathbf{x}_1\| + n_i,\ i = 2, 3, ..., M, \quad (2.7)$$

where n_i is a zero mean measurement error. Eqn (2.7) exhibits the beauty of the A-TDOA system that the time difference $(t_{ARR} - t_{ARD})$ is measured at and only at anchor Rx. Therefore, no clock synchronization is required among anchor Rx, anchor Tx and the target node. The use of the backbone cables which are mandatory in conventional TDOA positioning systems can now be avoided.

An example system layout is shown in Fig. 2.7. Three anchor Tx nodes and one anchor Rx node constitute the infrastructure. The solid lines indicate the direct radio paths between the anchor Tx nodes and the anchor Rx node, and the dashed lines

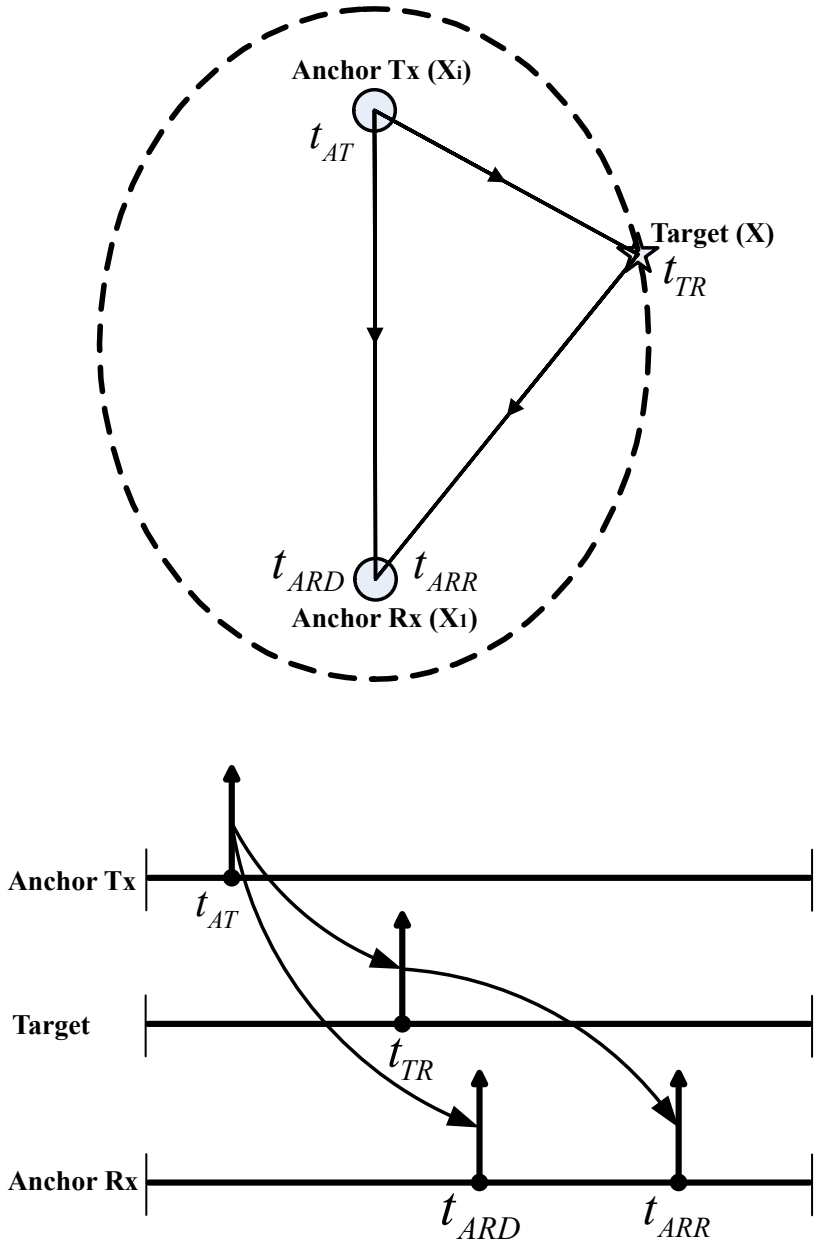

Figure 2.6: A-TDOA localization system signal flow and timing diagram.

indicate the retransmitted radio paths.

Rearranging Eqn (2.7) as

$$(t_{ARR} - t_{ARD}) \cdot c + \|\mathbf{x}_i - \mathbf{x}_1\| = \|\mathbf{x} - \mathbf{x}_i\| + \|\mathbf{x} - \mathbf{x}_1\| + n_i,\ i = 2, 3, ..., M, \quad (2.8)$$

it demonstrates that the sum of the distances from $\mathbf{x}$ to two fixed anchor nodes $\mathbf{x_i}$ and

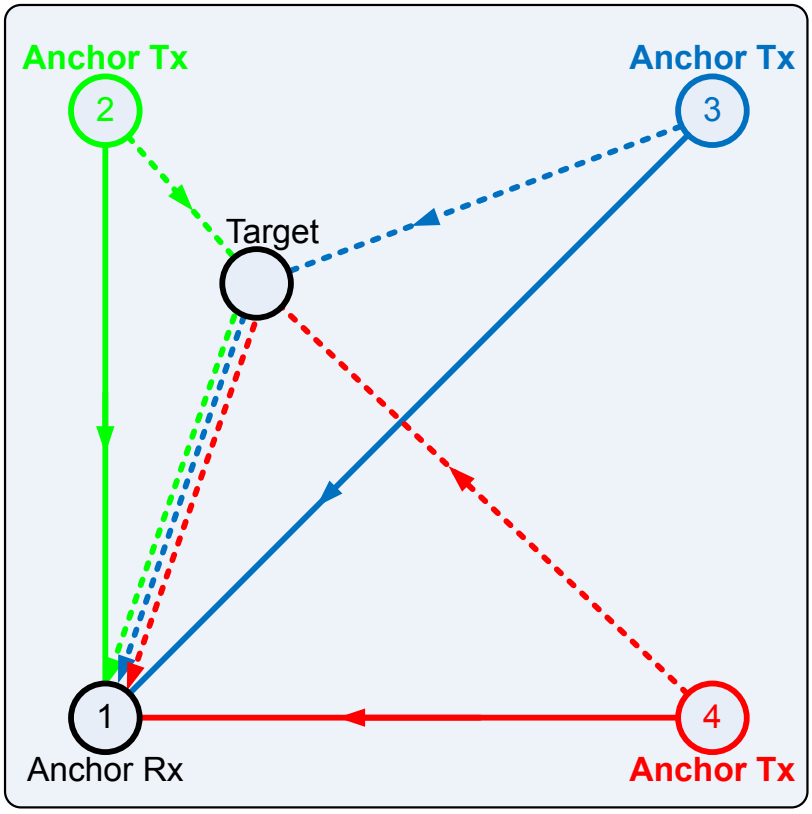

Figure 2.7: An example of an A-TDOA system layout.

$\mathbf{x_1}$ is a constant $\|\mathbf{x}_i - \mathbf{x}_1\|$ plus a distance difference which is measurable. Therefore, the target node must lie on the trajectory of an ellipse with anchor Tx and anchor Rx as the two foci. Fig. 2.8 illustrates the ellipse trajectory on which a target node is located.

2.2.1 Localization Techniques Comparison

A comparison of the aforementioned localization techniques are summarized in Table. 2.1. These systems mainly differ in synchronization level and implementation complexity. The highest accuracy can be achieved when system clocks are synchronized, and this will be mathematically proven in Chapter 3. The A-TDOA system achieves relatively good accuracy with very low complexity, by making a trade-off between synchronization and accuracy.

Table 2.1: Comparison of various positioning techniques.

Localization Technique	Synchronization Method	Synchronization Complexity	Accuracy	Implementation Complexity
RSS	Asynchronous	Not required	Low	Low. Can be easily implemented to the existing systems.
AOA	Asynchronous	Not required	Low	High. Antenna array is costly and complex.
TOA	Wireless Synchronous	High	High	High. High accuracy synchronization over the air is hard to achieve.
TDOA	Wireline Synchronous	Medium	High	Medium. Cable connected back-bone is required.
Two-way	Asynchronous	Not required	Medium	Medium. Requires clock offset mitigation techniques.
A-TDOA	Asynchronous	Not required	Medium	Low. Easy to implement.

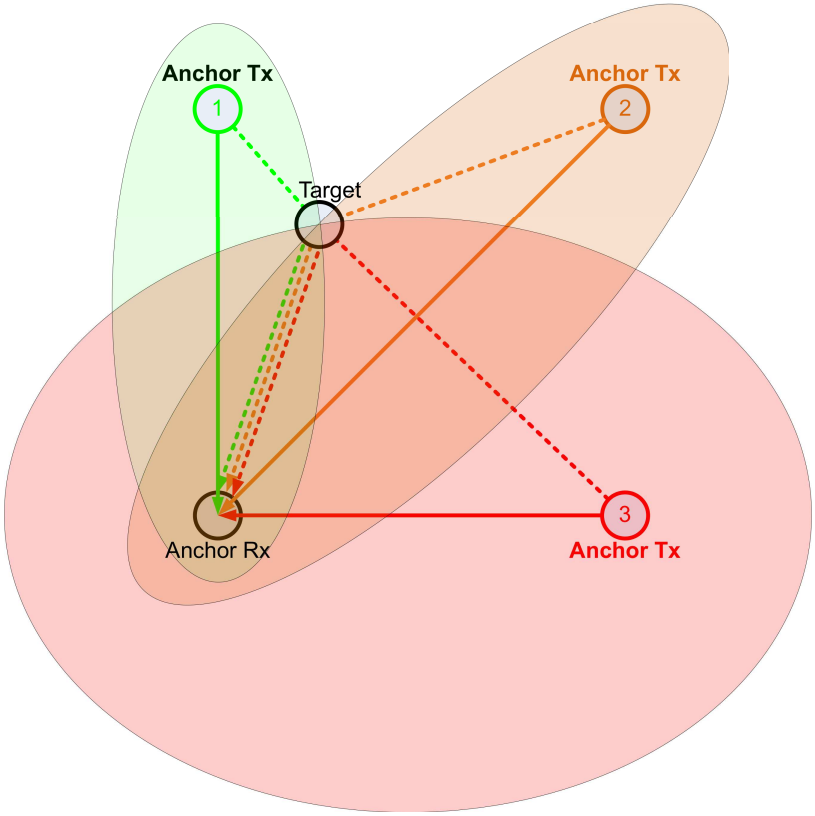

Figure 2.8: Ellipse trajectory of the A-TDOA system.

Chapter 3

Localization Bound

Cramer-Rao lower bound (CRLB) is commonly used for providing a lower bound on an estimator's mean square error (MSE). It establishes a fundamental limit on the achievable localization accuracy, and it serves as a benchmark for any unbiased location estimator. The CRLB can also be used to rule out infeasible estimators.

Previous work [53] [54] derive CRLB based on modeling range estimates as being corrupted by zero mean Gaussian noise . These works made an assumption that the variance of the range estimate is not dependent on the actual node pair distance. As a matter of fact, signal power decays as the propagation distance increases in practical situation. In an indoor environment, the path loss exponent can vary from 2 to 6 [55], and the signal power decays 20 to 60 dB as the propagation distance increases by a decade. This results in a significant received signal power variation. Given a constant thermal noise level, the received signal power variation results in a change in SNR, which in turn determines the achievable localization accuracy [54]. To reflect the SNR change, we follow a similar approached used in [56] to model noise variance as a distance dependent parameter. Such modeling is applied throughout this thesis, particularly in Chapter 3 and Chapter 4.

In this Chapter, we derive a distance dependent CRLB for A-TDOA localization systems. Since the path loss exponent is more significant in indoor environments, the new CRLB offers a more accurate lower bound. Most importantly, the new CRLB provides more insights into the impact of geometric configuration of anchor nodes on the localization accuracy. We also derive distance dependent CRLB for TOA and TDOA systems, so we can compare these three localization systems' best achievable performance.

3.1 Cramer-Rao Lower Bound Basics

When the probability density function (PDF) is viewed as a function of the unknown parameter, it is termed the likelihood function. Intuitively, the "sharpness" of the likelihood function determines how accurately we can estimate the unknown parameter. To quantify this notion observe that the sharpness is effectively measured by the negative of the second derivative of the logarithm of the likelihood function at its peak. This is the curvature of the log-likelihood function [57]. A measure of the curvature is referred to as the Fisher information:

$$\mathbf{F}(\theta) = -\mathbb{E}\left[\frac{\partial^2 \ln p(\mathbf{d};\boldsymbol{\theta})}{\partial \boldsymbol{\theta}^2}\right], \tag{3.1}$$

where $\mathbf{d}$ is a vector of the measurement observations, and $\boldsymbol{\theta}$ is a vector parameter $[\theta_1, \theta_2, \ldots, \theta_n]^T$ we wish to estimate.

The Cramer-Rao lower bound states that the variance of any unbiased estimator $\hat{\boldsymbol{\theta}}$ must satisfy

$$\text{var}\left(\hat{\boldsymbol{\theta}}\right) \geq \frac{1}{F\left(\boldsymbol{\theta}\right)} = \frac{1}{-\mathbb{E}\left[\frac{\partial^2 \ln p(\boldsymbol{d};\boldsymbol{\theta})}{\partial \boldsymbol{\theta}^2}\right]}, \tag{3.2}$$

where the derivative is evaluated at the true value of $\boldsymbol{\theta}$ and the expectation is taken with respect to $p(\boldsymbol{d};\boldsymbol{\theta})$. The expectation acknowledges the fact that the likelihood function, which depends on $\mathbf{d}$, is itself a random variable. The larger the quantity in Fisher information, the smaller the variance of the estimator. Or in other words, the more information, the lower the bound. According to [57], the CRLB is found as the $[\mathrm{i}_{th}, \mathrm{i}_{th}]$ element of the inverse of the Fisher information matrix:

$$\text{var}\left(\widehat{\theta_{\mathrm{i}}}\right) \geq \left[\mathrm{F}^{-1}\left(\boldsymbol{\theta}\right)\right]_{\mathrm{ii}}. \tag{3.3}$$

3.2 Distance Dependent CRLB for A-TDOA Localization Systems

In this section, we derive the distance dependent CRLB for a A-TDOA localization system. We first denote anchor nodes positions as $\mathbf{x}_i = [x_i, y_i]^T, i = 1, 2, ..., N$, and target node position as $\mathbf{x} = [x, y]^T$. The measured distance difference between a

direct path and a re-transmitted path can be written as

$$r_i = d_i + n_i, \;\; i = 2, 3, ..., M, \tag{3.4}$$

where d_i is the true distance difference of arrival

$$d_i = \|\mathbf{x} - \mathbf{x_i}\| + \|\mathbf{x} - \mathbf{x_1}\| - \|\mathbf{x_i} - \mathbf{x_1}\| \tag{3.5}$$

and $n_i \sim \mathcal{N}(0, \sigma_i^2)$ is a zero mean Gaussian error, whose variance is modeled as

$$\sigma_i^2 = K_E(\|\mathbf{x} - \mathbf{x_i}\| + \|\mathbf{x} - \mathbf{x_1}\|)^\beta + K_E(\|\mathbf{x_i} - \mathbf{x_1}\|)^\beta. \tag{3.6}$$

In (3.6), K_E is a proportionality constant to capture the combined physical layer effect on the range estimate and β is the path loss exponent. Compared to TOA noise variance, the A-TDOA system's noise variance is significantly higher, due to that the extra signal transmission scheme is involved. As described in Section 3.1, we first derive the Fisher information matrix. The probability density function for r_i is given by

$$f\left(r_i|d_i\right) = \frac{1}{\sqrt{2\pi\sigma_i^2}} \exp\left(-\frac{(r_i - d_i)^2}{2\sigma_i^2}\right). \tag{3.7}$$

The log-likelihood function can then be expressed as

$$\begin{aligned} \ln f\left(r|\mathbf{x}\right) = \quad & -\frac{1}{2}\ln\left(2\pi K_E\right) \\ & -\frac{1}{2}\ln\left[(\|\mathbf{x} - \mathbf{x_i}\| + \|\mathbf{x} - \mathbf{x_1}\|)^\beta + (\|\mathbf{x_i} - \mathbf{x_1}\|)^\beta\right] \\ & -\frac{1}{2K_E}\frac{(\|\mathbf{x} - \mathbf{x_i}\| + \|\mathbf{x} - \mathbf{x_1}\| - \|\mathbf{x_i} - \mathbf{x_1}\| - r)^2}{(\|\mathbf{x} - \mathbf{x_i}\| + \|\mathbf{x} - \mathbf{x_1}\|)^\beta + (\|\mathbf{x_i} - \mathbf{x_1}\|)^\beta} \end{aligned} \tag{3.8}$$

For the sake of simpler expression, we denote

$$A = -\frac{1}{2}\ln\left[(\|\mathbf{x} - \mathbf{x_i}\| + \|\mathbf{x} - \mathbf{x_1}\|)^\beta + (\|\mathbf{x_i} - \mathbf{x_1}\|)^\beta\right], \tag{3.9}$$

and

$$B = -\frac{1}{2K_E}\frac{(\|\mathbf{x} - \mathbf{x_i}\| + \|\mathbf{x} - \mathbf{x_1}\| - \|\mathbf{x_i} - \mathbf{x_1}\| - r)^2}{(\|\mathbf{x} - \mathbf{x_i}\| + \|\mathbf{x} - \mathbf{x_1}\|)^\beta + (\|\mathbf{x_i} - \mathbf{x_1}\|)^\beta}. \tag{3.10}$$

To derive the FIM, we need to calculate the second derivative of the likelihood function and then apply the expectation operation. Below we present the final results:

$$\begin{aligned}\mathbb{E}\left[\frac{\partial^2 A}{\partial \mathbf{x}^2}\right] = \quad & \frac{\beta^2 \cdot \left[\|\mathbf{x}-\mathbf{x_i}\| + \|\mathbf{x}-\mathbf{x_1}\|\right]^{2\beta-2} \cdot \left(\frac{x-x_1}{\|\mathbf{x}-\mathbf{x_1}\|} + \frac{x-x_i}{\|\mathbf{x}-\mathbf{x_i}\|}\right)^2}{2 \cdot \left[\left(\|\mathbf{x}-\mathbf{x_i}\| + \|\mathbf{x}-\mathbf{x_1}\|\right)^{\beta} + \|\mathbf{x_i}-\mathbf{x_1}\|^{\beta}\right]^2} \\ & + \frac{\beta \cdot \left(\|\mathbf{x}-\mathbf{x_i}\| + \|\mathbf{x}-\mathbf{x_1}\|\right)^{\beta-1} \cdot \left[\frac{(x-x_1)^2}{\|\mathbf{x}-\mathbf{x_1}\|^3} + \frac{(x-x_i)^2}{\|\mathbf{x}-\mathbf{x_i}\|^3} - \frac{1}{\|\mathbf{x}-\mathbf{x_1}\|} - \frac{1}{\|\mathbf{x}-\mathbf{x_i}\|}\right]}{2 \cdot \left[\left(\|\mathbf{x}-\mathbf{x_i}\| + \|\mathbf{x}-\mathbf{x_1}\|\right)^{\beta} + \|\mathbf{x_i}-\mathbf{x_1}\|^{\beta}\right]} \\ & + \frac{\beta\left(\beta-1\right) \cdot \left(\|\mathbf{x}-\mathbf{x_i}\| + \|\mathbf{x}-\mathbf{x_1}\|\right)^{\beta-2} \cdot \left(\frac{x-x_1}{\|\mathbf{x}-\mathbf{x_1}\|} + \frac{x-x_i}{\|\mathbf{x}-\mathbf{x_i}\|}\right)^2}{2 \cdot \left[\left(\|\mathbf{x}-\mathbf{x_i}\| + \|\mathbf{x}-\mathbf{x_1}\|\right)^{\beta} + \|\mathbf{x_i}-\mathbf{x_1}\|^{\beta}\right]}\end{aligned} \tag{3.11}$$

$$\begin{aligned}\mathbb{E}\left[\frac{\partial^2 B}{\partial \mathbf{x}^2}\right] = \quad & \frac{\beta\left(\beta-1\right) \cdot \left(\|\mathbf{x}-\mathbf{x_i}\| + \|\mathbf{x}-\mathbf{x_1}\|\right)^{\beta-2} \cdot \left(\frac{x-x_1}{\|\mathbf{x}-\mathbf{x_1}\|} + \frac{x-x_i}{\|\mathbf{x}-\mathbf{x_i}\|}\right)^2 \cdot \sigma_i^2}{2 \cdot K_E \cdot \left[\left(\|\mathbf{x}-\mathbf{x_i}\| + \|\mathbf{x}-\mathbf{x_1}\|\right)^{\beta} + \|\mathbf{x_i}-\mathbf{x_1}\|^{\beta}\right]^2} \\ & - \frac{\beta^2 \cdot \left(\|\mathbf{x}-\mathbf{x_i}\| + \|\mathbf{x}-\mathbf{x_1}\|\right)^{2\beta-2} \cdot \left(\frac{x-x_1}{\|\mathbf{x}-\mathbf{x_1}\|} + \frac{x-x_i}{\|\mathbf{x}-\mathbf{x_i}\|}\right)^2 \cdot \sigma_i^2}{K_E \cdot \left[\left(\|\mathbf{x}-\mathbf{x_i}\| + \|\mathbf{x}-\mathbf{x_1}\|\right)^{\beta} + \|\mathbf{x_i}-\mathbf{x_1}\|^{\beta}\right]^3} \\ & - \frac{\beta \cdot \left(\|\mathbf{x}-\mathbf{x_i}\| + \|\mathbf{x}-\mathbf{x_1}\|\right)^{\beta-1} \cdot \sigma_i^2 \cdot \left[\frac{(x-x_1)^2}{\|\mathbf{x}-\mathbf{x_1}\|^3} + \frac{(x-x_i)^2}{\|\mathbf{x}-\mathbf{x_i}\|^3} - \frac{1}{\|\mathbf{x}-\mathbf{x_1}\|} - \frac{1}{\|\mathbf{x}-\mathbf{x_i}\|}\right]}{2 \cdot K_E \cdot \left[\left(\|\mathbf{x}-\mathbf{x_i}\| + \|\mathbf{x}-\mathbf{x_1}\|\right)^{\beta} + \|\mathbf{x_i}-\mathbf{x_1}\|^{\beta}\right]^2} \\ & - \frac{\left(\frac{x-x_1}{\|\mathbf{x}-\mathbf{x_1}\|} + \frac{x-x_i}{\|\mathbf{x}-\mathbf{x_i}\|}\right)^2}{K_E \cdot \left[\left(\|\mathbf{x}-\mathbf{x_i}\| + \|\mathbf{x}-\mathbf{x_1}\|\right)^{\beta} + \|\mathbf{x_i}-\mathbf{x_1}\|^{\beta}\right]}\end{aligned} \tag{3.12}$$

To simplify above expressions, we denote

$$g_i = \left(\|\mathbf{x}-\mathbf{x_i}\| + \|\mathbf{x}-\mathbf{x_1}\|\right)^{\beta} + \|\mathbf{x_i}-\mathbf{x_1}\|^{\beta} \tag{3.13a}$$

$$f_{xxi} = \left(\frac{x-x_1}{\|\mathbf{x}-\mathbf{x_1}\|} + \frac{x-x_i}{\|\mathbf{x}-\mathbf{x_i}\|}\right)^2 \tag{3.13b}$$

$$f_{yyi} = \left(\frac{y-y_1}{\|\mathbf{x}-\mathbf{x_1}\|} + \frac{y-y_i}{\|\mathbf{x}-\mathbf{x_i}\|}\right)^2 \tag{3.13c}$$

$$f_{xyi} = \left(\frac{x-x_1}{\|\mathbf{x}-\mathbf{x_1}\|} + \frac{x-x_i}{\|\mathbf{x}-\mathbf{x_i}\|}\right)\cdot\left(\frac{y-y_1}{\|\mathbf{x}-\mathbf{x_1}\|} + \frac{y-y_i}{\|\mathbf{x}-\mathbf{x_i}\|}\right) \tag{3.13d}$$

$$p_i = \|\mathbf{x}-\mathbf{x_i}\| + \|\mathbf{x}-\mathbf{x_1}\| \tag{3.13e}$$

$$s_{xxi} = \frac{(x-x_1)^2}{\|\mathbf{x}-\mathbf{x_1}\|^3} + \frac{(x-x_i)^2}{\|\mathbf{x}-\mathbf{x_i}\|^3} - \frac{1}{\|\mathbf{x}-\mathbf{x_1}\|} - \frac{1}{\|\mathbf{x}-\mathbf{x_i}\|} \tag{3.13f}$$

$$s_{yyi} = \frac{(y-y_1)^2}{\|\mathbf{x}-\mathbf{x_1}\|^3} + \frac{(y-y_i)^2}{\|\mathbf{x}-\mathbf{x_i}\|^3} - \frac{1}{\|\mathbf{x}-\mathbf{x_1}\|} - \frac{1}{\|\mathbf{x}-\mathbf{x_i}\|} \tag{3.13g}$$

$$s_{xyi} = \frac{(x-x_1)(y-y_1)}{\|\mathbf{x}-\mathbf{x_1}\|^3} + \frac{(x-x_i)(y-y_i)}{\|\mathbf{x}-\mathbf{x_i}\|^3} - \frac{1}{\|\mathbf{x}-\mathbf{x_1}\|} - \frac{1}{\|\mathbf{x}-\mathbf{x_i}\|}, \tag{3.13h}$$

and therefore

$$\mathbb{E}\left[\frac{\partial^2 A}{\partial \mathbf{x}^2}\right] + \mathbb{E}\left[\frac{\partial^2 B}{\partial \mathbf{x}^2}\right] = -\frac{\beta^2 \cdot {p_i}^{2\beta-2} \cdot f_{xxi}}{2g_i^2} - \frac{\beta \cdot {p_i}^{\beta-1} \cdot s_{xxi}}{2g_i} - \frac{f_{xxi}}{K_E g_i} \tag{3.14a}$$

$$\mathbb{E}\left[\frac{\partial^2 A}{\partial \mathbf{y}^2}\right] + \mathbb{E}\left[\frac{\partial^2 B}{\partial \mathbf{y}^2}\right] = -\frac{\beta^2 \cdot {p_i}^{2\beta-2} \cdot f_{yyi}}{2g_i^2} - \frac{\beta \cdot {p_i}^{\beta-1} \cdot s_{yyi}}{2g_i} - \frac{f_{yyi}}{K_E g_i} \tag{3.14b}$$

$$\mathbb{E}\left[\frac{\partial^2 A}{\partial \mathbf{x}\partial \mathbf{y}}\right] + \mathbb{E}\left[\frac{\partial^2 B}{\partial \mathbf{x}\partial \mathbf{y}}\right] = -\frac{\beta^2 \cdot {p_i}^{2\beta-2} \cdot f_{xyi}}{2g_i^2} - \frac{\beta \cdot {p_i}^{\beta-1} \cdot s_{xyi}}{2g_i} - \frac{f_{xyi}}{K_E g_i}. \tag{3.14c}$$

Ultimately, $[F(\boldsymbol{\theta})]$ in the FIM can be written as:

$$[F(\mathbf{x})]_{11} = \sum_{i=1}^{N}\left[\frac{\beta^2 \cdot {p_i}^{2\beta-2} \cdot f_{xxi}}{2g_i^2} + \frac{\beta \cdot {p_i}^{\beta-1} \cdot s_{xxi}}{2g_i} + \frac{f_{xxi}}{K_E g_i}\right] \tag{3.15a}$$

$$[F(\mathbf{x})]_{22} = \sum_{i=1}^{N}\left[\frac{\beta^2 \cdot {p_i}^{2\beta-2} \cdot f_{yyi}}{2g_i^2} + \frac{\beta \cdot {p_i}^{\beta-1} \cdot s_{yyi}}{2g_i} + \frac{f_{yyi}}{K_E g_i}\right] \tag{3.15b}$$

$$[F(\mathbf{x})]_{12} = [F(\mathbf{x})]_{21} = \sum_{i=1}^{N}\left[\frac{\beta^2 \cdot {p_i}^{2\beta-2} \cdot f_{xyi}}{2g_i^2} + \frac{\beta \cdot {p_i}^{\beta-1} \cdot s_{xyi}}{2g_i} + \frac{f_{xyi}}{K_E g_i}\right] \tag{3.15c}$$

The A-TDOA CRLB is shown in Fig. 3.1. The x- and y- axis indicate the target node coordinate, and the z- axis is the mean square position error expressed in dB (for

instance, -20 dB corresponds to $\sqrt{10^{-20/10}} = 0.1$ m). The minimum error variance is evaluated at each coordinate in a 100×100 area. Four anchor nodes are located at (0, 0), (0, 100), (100, 0) and (100, 100). The path loss exponent β is set to 4 to capture a realistic radio propagation channel. The path loss exponent β is set to 4 to capture a realistic radio propagation channel. The constant K_E is set to $\frac{\sigma_0^2}{(50\sqrt{2})^\beta}$, so that when the target node is at the center, i.e., coordinate (50, 50), the noise variance from the target node to any anchor node is $K_E \cdot \|\mathbf{x} - \mathbf{x}_i\|^\beta = \frac{\sigma_0^2}{(50\sqrt{2})^\beta} \cdot (50\sqrt{2})^\beta = \sigma_0^2$. We used $\sigma_0 = 0.1$ m in the simulation.

It is obvious that the position estimation error close to the anchor Rx node (coordinate (0, 0)) is much smaller than other positions, largely due to that the noise variance is smaller when the target node is close to the anchor Rx. Therefore, when multiple transceiver anchor nodes are available in the system, the anchor Rx node can be chosen as the one closest to the target node to minimize the estimation error. We refer to this method as "receiver re-selection". This method requires the system to have a-priori knowledge of an approximate target node position. This a-priori knowledge can easily be obtained by using a localization algorithm that achieves global convergence to estimate approximate coordinates of the target node. This position estimate can then be used to re-select the receiver node. Given the updated receiver node and approximate target node coordinates as an initial guess, a high accuracy algorithm can then be applied to give superb performance. Fig. 3.2 demonstrates the improved CRLB by selecting a proper anchor Rx node such that the CRLB becomes minimal.

A comparison of TOA, TDOA, and A-TDOA system's CRLB is shown in Fig. 3.3. It is observed that the TOA system achieves the lowest MSE, which is less than -14 dB (approximately 0.2 m). The TDOA system's MSE is about 1 dB higher than TOA system. It is obvious that the A-TDOA CRLB is about 8 dB higher than TOA and TDOA CRLB. This is largely due to the extra signal transmission scheme involved in the localization process, that is, it requires both direct path and re-transmitted path signal for localization and the compound noise power is significantly higher than TOA and TDOA systems. Nevertheless, although the A-TDOA system signaling is slightly complicated and the performance is poorer, it worths the effort to relax the more difficult clock synchronization requirement and therefore provides great potential for practical use.

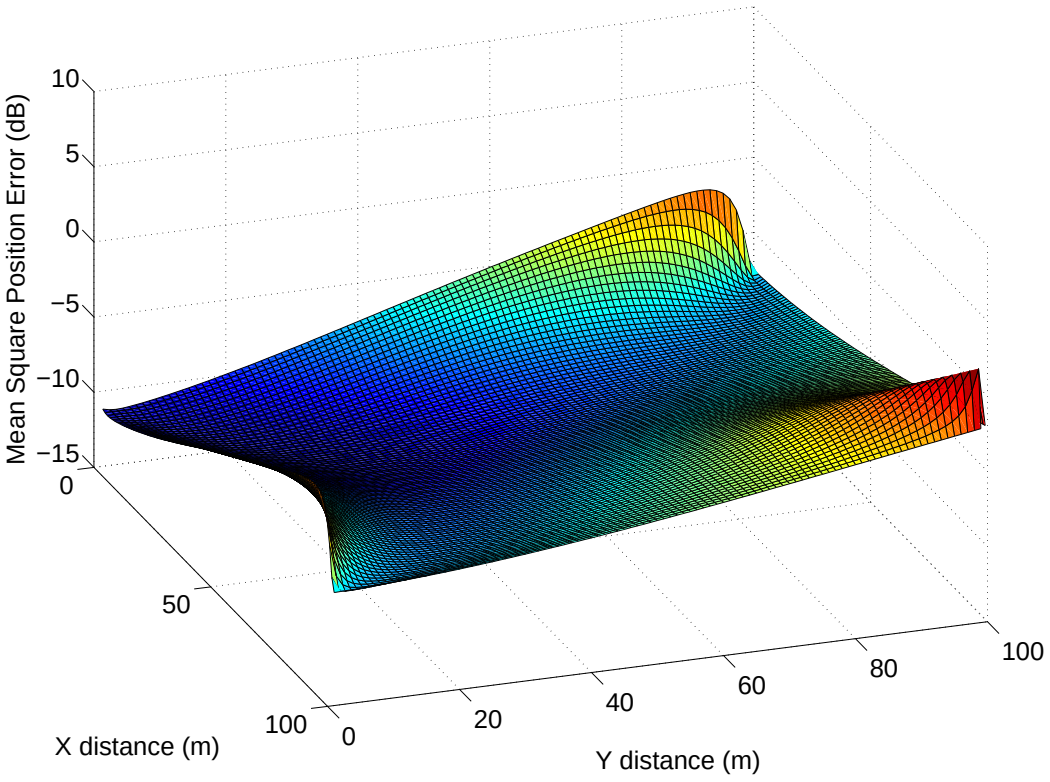

Figure 3.1: The CRLB of an A-TDOA localization system.

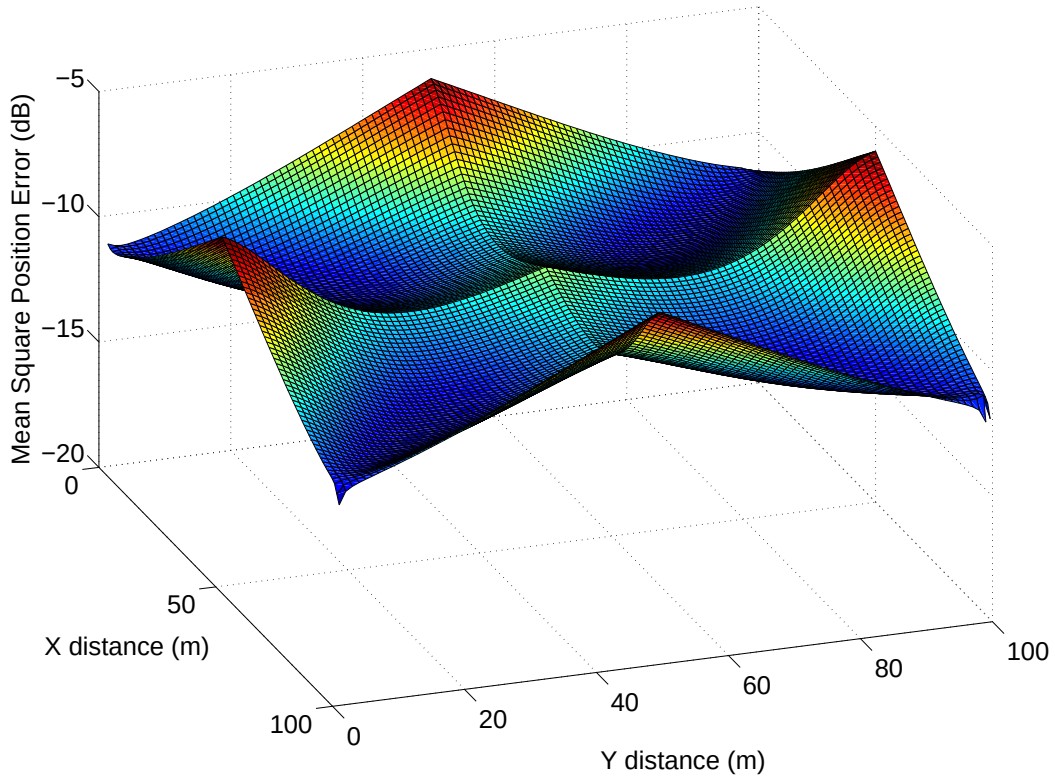

Figure 3.2: The CRLB of an A-TDOA localization system with receiver re-selection.

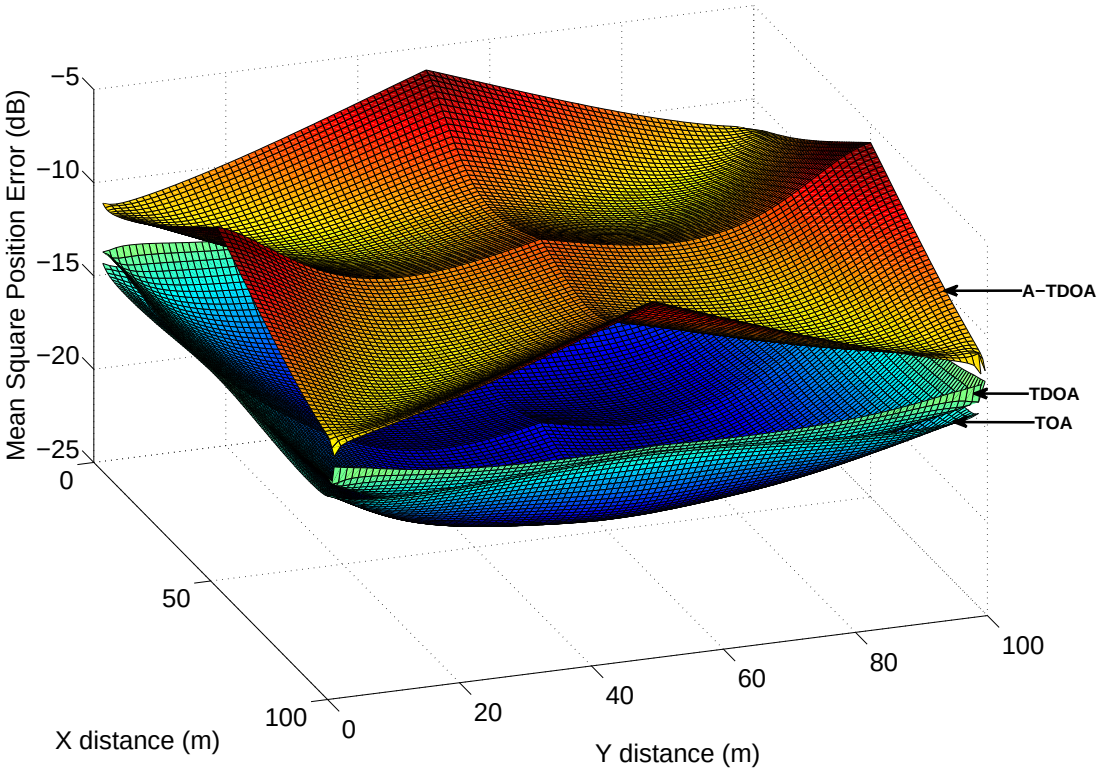

Figure 3.3: Comparison of the TOA, TDOA, and A-TDOA system CRLB.

Chapter 4

A-TDOA Localization Algorithms

The essence of any wireless localization technologies is to measure the location dependent parameters such as TOA, TDOA, AOA and so on between anchors and target node, and then to estimate the position of the target through proper processing of the measured parameters. Given a set of measured data, location estimators adjust the model parameter values such that the distance between an objective function and the observation data is minimal. This is usually done by applying numerical optimization algorithms to the objective function used to represent the problem. Often the objective function is non-convex and therefore the solution is only a local minima which in turn implies the non-optimality of the solution. In particular, given the observation vector $\mathrm{z} \in \mathrm{R}^{\mathrm{n_z} \times 1}$ and $f(\cdot)$ as the function relating measurements and the vector parameter $\mathrm{x} \in \mathrm{R}^{\mathrm{n_x} \times 1}$; most of the formulations used to do parameter estimation rely on either of the following:

- minimization of a least squares (LS) function:

$$\widehat{\mathbf{x}}_{LS} \stackrel{\Delta}{=} \arg\min_{\mathbf{x}} \|\mathbf{z} - f(\mathbf{x})\|^2 \tag{4.1}$$

- maximization of the likelihood function $p(\mathbf{z}|\mathbf{x})$:

$$\widehat{\mathbf{x}}_{ML} \stackrel{\Delta}{=} \arg\max_{\mathbf{x}} p(\mathbf{z}|\mathbf{x}) \tag{4.2}$$

Consequently, the most widely applied algorithms in localization systems are least squares and maximum likelihood (ML). Lately, semidefinite programming methods are also developed to solve localization problems. But essentially, the SDP technique

is to convert a nonconvex ML problem to a convex optimization program. In this chapter, a thorough review of the commonly used position estimation algorithms is presented with a focus on LS, ML and SDP methods. In addition, two new algorithms are proposed to solve location estimation problem for the A-TDOA system. The first algorithm is a two-step algorithm that uses the SDP technique to get an approximate estimation on the target node coordinate, and then feed it to a Taylor estimator as an initial guess to achieve superior accuracy. The second algorithm is a constrained least squares (CLS) estimator which has low complexity and fast convergence while maintaining good performance.

4.1 Overview of the Localization Estimators

4.1.1 Maximum Likelihood Estimator

Assuming that the range measurements errors are Gaussian distributed, the maximum likelihood methods can be applied for node localization. The concept of the ML method is straightforward: given the observed data and a model of interest, find the probability density function, among all the probability densities that the model prescribes, that is most likely to have produced the data. This is the principle of the ML estimator, which seeks the value of the parameter vector that maximizes the likelihood function $p(\mathbf{z}|\mathbf{x})$. The likelihood function can be expressed as a multiplication of PDFs for individual observations

$$p(\mathbf{z}|\mathbf{x}) = \mathbf{p}(\mathbf{z_1}|\mathbf{x}) \cdot \mathbf{p}(\mathbf{z_2}|\mathbf{x}) \cdots \mathbf{p}(\mathbf{z_M}|\mathbf{x}), \tag{4.3}$$

when individual observations $\mathbf{z}$ are statistically independent of one another. Fig. 4.1 shows an example likelihood function created based on a TDOA localization system [58].

When measurement error distribution is available, the maximum likelihood estimator (MLE) is commonly used. An approximate maximum likelihood algorithm was developed in [59] to achieve near-optimal performance without the complexity of "full" maximum likelihood estimation. In [60], an MLE is applied on a set of RSS measurements showing excellent positioning accuracy. A maximum likelihood based algorithm was proposed in [61], and simulation results reveal that the solution closely approaches the fundamental bounds. In spite of attaining optimum estimation per-

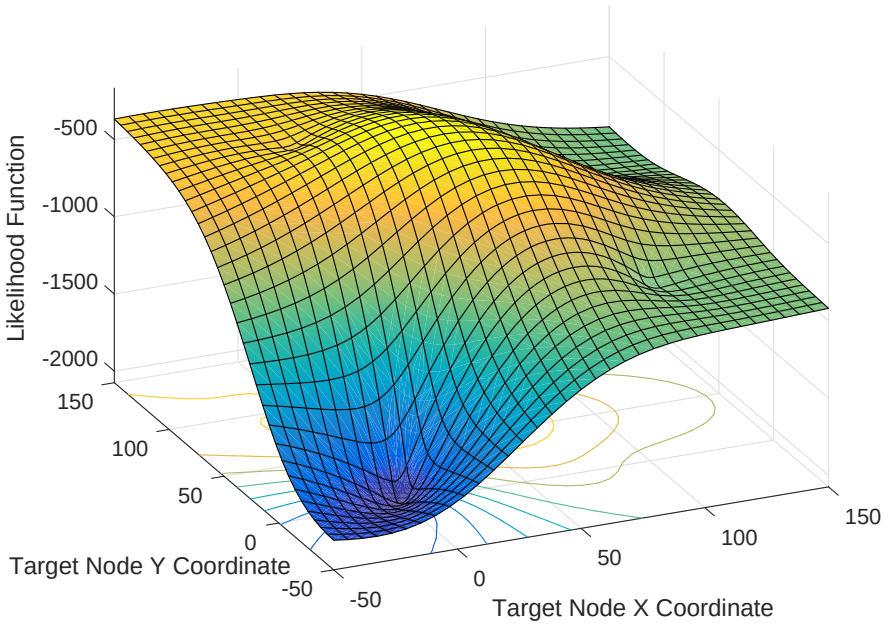

Figure 4.1: An example objective function of the TDOA MLE.

formance, the ML approach requires sufficiently precise initial estimates for global convergence. In [62], it has been shown that the positioning accuracy of the ML methodology attains Cramer-Rao lower bound at sufficiently small noise conditions. However, it is difficult to implement in practice because the ML cost function is highly nonlinear and contains multiple local minima and maxima. Hence its maximization is sensitive to initial conditions and there is no guarantee of global optimality [6]. In [63], results show that even when the ML estimator is initialized by a weighted least squares estimate, which is close to the global solution, it still converges occasionally to a local minimum. The only way to achieve the global optimality is to perform a dense grid search but its computational complexity is very demanding. To overcome the convergence issue, the SDP method is often applied to map the original non-convex ML problem to a convex problem, such that convergence guarantee can be obtained. Section 4.1.3 provides details of the SDP algorithm.

4.1.2 Least Squares Estimator

Unlike the maximum likelihood approach, the least squares approach does not assume any characterization of the noise statistic affecting the observations; hence it

is deemed a suboptimal method [64]. However, it has low computational complexity and therefore is easy to implement in a practical system.

Basically, there are two approaches for solving the nonlinear equations. The first approach is to solve them directly in a nonlinear least squares (NLS) or weighted least squares (WLS) framework [65–67]. The common procedure is linearization followed by gradient searches. Although optimum estimation performance can be attained, it requires sufficiently precise initial estimates for global convergence because the corresponding cost functions are multimodal. The second approach is to reorganize the nonlinear equations into a set of linear equations so that real-time implementation is allowed and global convergence is ensured [1, 6, 31, 68–70].

In [66], a WLS approach is devised to apply smaller weights to the measurements which are likely to be biased due to non-line of sight (NLOS) transmission. Linearized least squares method is applied in [65] [67] to linearize the error equations about a point sufficiently close to the target so that the linearization errors are negligible compared to the root mean squared (RMS) errors. In [69], the nonlinear cost functions are reorganized into a set of linear equations by introducing an intermediate variable, which is a function of the source position, and this technique is commonly called spherical interpolation (SI). The SI method provides closed-form solution which helps to ease implementation difficulties, but it does not consider the known relation between the intermediate variable and the position coordinate, and therefore the estimation accuracy is relatively low. An improved algorithm is presented in [31] to exploit this relation via a relaxation procedure. Further improvement was made in [1, 70] by minimizing a constrained LS function. These linear equations are then solved in an optimum manner with the use of weighted least squares and Lagrange multipliers.

4.1.3 Semidefinite Programming

The basic idea of the SDP technique is to approximate the nonconvex ML formulation to a convex optimization program which always guarantees a global solution [71]. In a lot of cases it converts the nonconvex quadratic distance constraints into convex constraints by introducing a relaxation to remove the quadratic term in the formulation. Generally speaking, when the relaxation is sufficiently tight, the SDP solution is an approximate ML estimate. However, as will be pointed out in Section 4.3, the SDP formulation for A-TDOA system is not perfectly tight, and therefore, its solution is then used as a starting point for descent based local optimization techniques that can

further refine the solution. In fact, the SDP solution turns out to be an excellent starting point for the local optimization and provides good convergence.

In [72], techniques to solve the sensor network localization problem using semidefinite programming were presented by minimizing the ℓ_1- norm of estimation error. Extensions of the SDP formulation to TDOA scenarios were proposed in [73]. In [74], RSS based ML problems have been relaxed to a convex optimization problem in the form of a SDP, so that global convergence is always attained. By applying a RSS measurement under the well-known lognormal fading model, the authors of [75] also derived efficient SDP approaches to source localization based on a min-max criteria. In [76], two semidefinite relaxation algorithms were developed by adopting a min-max principle under colored measurement noise. The methods are insensitive to the source locations and can be used either as the final location estimate or as the initial point for more traditional search algorithms.

4.1.4 Other Methods

In addition to these conventional approaches, particle swarm optimization (PSO) is also employed for position estimation [77]. But in comparison with conventional approaches, PSO has many user defined parameters that can affect the performance significantly. Also, when a massive amount of particles are involved, the computing time is unduly high. Another commonly used method is centroid localization technique [78], in which the source location is approximated as the weighted average of all receivers within its transmission range. Although it is simple to implement and robust to variations in the propagation environment, its positioning accuracy is generally low.

4.1.5 Localization Algorithms Summary

Table 4.1 summarizes the advantages and disadvantages of the commonly used algorithms mentioned above.

4.2 Linear Least Squares Algorithm

In this section, we briefly describe the basics of the linear least squares (LLS) estimator, as it can provide a closed-form solution and hence is commonly used in

Table 4.1: Summary of the commonly used algorithms.

Estimator	Advantages	Disadvantages
LLS	• Global solution is guaranteed. • Simple and computationally efficient. • Noise statistics are not needed.	• Accuracy is generally low.
NLS	• Accuracy is generally high. • Noise statistics are not needed.	• Global solution may not be guaranteed. • Complexity is high if grid or random search is involved.
MLE	• Accuracy is highest.	• Global solution may not be guaranteed. • Complexity is high if grid or random search is involved. • Noise statistics are needed.
SDP	• Global solution is guaranteed. • Highest accuracy can be achieved with constraints.	• Complexity is high.

localization systems. In addition, it is applied in our proposed two-step localization algorithm as one of the steps to expedite the convergence speed.

Essentially, the LS method attempts to minimize the power of an error function, and different error functions can be defined by comparing the difference between the observed data and true values (noiseless) which are derived by manipulating the system model. For the proposed A-TDOA system, the localization problem can be stated mathematically as follows.

Without loss of generality, let anchor Rx be anchor node x_1, which is placed at the origin of the coordinate system, i.e., $\mathbf{x_1} = [\mathbf{0}, \mathbf{0}]^{\mathbf{T}}$. The distance from the origin to the i_{th} anchor Tx node and the target node are denoted by R_i and R_s, respectively, where

$$R_i \triangleq \sqrt{x_i^2 + y_i^2}, \quad i = 2, 3, \ldots, M, \tag{4.4}$$

and

$$R_s \triangleq \sqrt{x^2 + y^2}. \tag{4.5}$$

The distance between the target and the i_{th} anchor Tx is denoted by

$$D_i \triangleq \|\mathbf{x} - \mathbf{x_i}\|. \tag{4.6}$$

The measured range difference d_{i1} is defined in Section 3.2 and is reiterated here for

the sake of clear expression:

$$\begin{aligned} d_{i1} &= \|\mathbf{x}-\mathbf{x_i}\| + \|\mathbf{x}-\mathbf{x_1}\| - \|\mathbf{x_i}-\mathbf{x_1}\| + n_i \\ &= D_i + R_s - R_i + n_i. \end{aligned} \tag{4.7}$$

We define a new parameter $\hat{D}_i$ that is based on the measured range difference d_{i1} as

$$\hat{D}_i = d_{i1} - R_s + R_i. \tag{4.8}$$

From the law of cosines, we can derive the true value for D_i^2 as

$$D_i^2 = R_i^2 + R_s^2 - 2\mathbf{x_i}^\mathbf{T}\mathbf{x}. \tag{4.9}$$

Therefore the error function can be defined as the squared difference between the measured and true values expressed as

$$\begin{aligned} e_i &\triangleq \frac{1}{2}(\hat{D}_i^2 - D_i^2) \\ &= \frac{1}{2}(d_{i1}^2 - 2d_{i1}R_s + 2d_{i1}R_i + R_s^2 - 2R_sR_i + R_i^2 - R_i^2 - R_s^2 + 2\mathbf{x_i}^\mathbf{T}\mathbf{x}) \\ &= \mathbf{x_i}^\mathbf{T}\mathbf{x} - (d_{i1}+R_i)R_s - \frac{1}{2}(-d_{i1}^2 - 2d_{i1}R_i) \quad i = 2,3,\ldots,M \end{aligned} \tag{4.10}$$

Combining the M errors together and writing them in a vector form gives

$$\mathbf{e}(\mathbf{x}) = \mathbf{A}\boldsymbol{\theta} - \mathbf{b}, \tag{4.11}$$

where

$$\mathbf{A} = \begin{bmatrix} x_2 & y_2 & -(d_{21}+R_2) \\ x_3 & y_3 & -(d_{31}+R_3) \\ \vdots & \vdots & \vdots \\ x_M & y_M & -(d_{M1}+R_M), \end{bmatrix} \tag{4.12}$$

$$\boldsymbol{\theta} = \begin{bmatrix} x \\ y \\ R_s, \end{bmatrix} \tag{4.13}$$

and

$$\mathbf{b} = \frac{1}{2}\begin{bmatrix} -d_{21}^2 - 2d_{21}R_2 \\ -d_{31}^2 - 2d_{31}R_3 \\ \vdots \\ -d_{M1}^2 - 2d_{M1}R_M. \end{bmatrix} \tag{4.14}$$

The estimated parameter can be written as

$$\hat{\boldsymbol{\theta}} = \begin{bmatrix} \hat{x} \\ \hat{y} \\ \widehat{R_s} \end{bmatrix} = \left(\mathbf{A^T A}\right)^{-1} \cdot \mathbf{A^T} \cdot \mathbf{b} \tag{4.15}$$

4.3 Two-step Localization Algorithm

In this chapter, we present a two-step localization algorithm that combines the semidefinite programming and Taylor series methods to achieve high estimation accuracy. Introduced in Section 4.1.1, the MLE is highly non-linear and does not assure global convergence. Common methods to solve an ML problem include gradient descent algorithms and linearizion techniques using Taylor series expansion. However, none of these methods guarantees global minimal. Alternatively, it is possible to relax the ML formulation to a SDP problem in order to provide a high-fidelity approximate solution that can be obtained in a globally optimum fashion with reduced computational efforts. Hence, we develop a two-step algorithm that takes advantage of the SDP's global convergence property as well as the Taylor series method's high accuracy to achieve superior performance.

We denote the measured distance difference between a direct path and a retransmitted path as

$$r_i = d_i + n_i, \quad i = 2, 3, ..., M, \tag{4.16}$$

where d_i is the true distance difference of arrival

$$d_i = \|\mathbf{x} - \mathbf{x_i}\| + \|\mathbf{x} - \mathbf{x_1}\| - \|\mathbf{x_i} - \mathbf{x_1}\| \tag{4.17}$$

and $n_i \sim \mathcal{N}(0, \sigma_i^2)$ is a zero mean Gaussian error, whose variance is modeled as

$$\sigma_i^2 = K_E(\|\mathbf{x} - \mathbf{x_i}\| + \|\mathbf{x} - \mathbf{x_1}\|)^\beta + K_E(\|\mathbf{x_i} - \mathbf{x_1}\|)^\beta. \tag{4.18}$$

The probability density function for r_i is expressed as

$$f\left(r_i|d_i\right) = \frac{1}{\sqrt{2\pi\sigma_i^2}} \exp\left(-\frac{\left(r_i - d_i\right)^2}{2\sigma_i^2}\right). \tag{4.19}$$

For the A-TDOA system, each anchor Tx emits a pulse which is received by anchor Rx directly. The pulse is also received and re-transmitted by the target and later acquired by the same anchor Rx node. Therefore, the anchor Rx receives two pulses in a row and their time difference of arrival can be measured. A set of $M-1$ anchor Tx nodes can generate $M-1$ time difference measurements r_i, $i = 2, 3, ..., M$, and most importantly, these measurements are independent of each other. This is essentially different from a regular TDOA system, where the time of arrival is measured by each anchor node so that the time difference measurements are derived by subtracting a pair of time of arrivals. Consequently, the TDOA system's time difference measurements are not independent and a correlated Gaussian error model must be used [79].

These $M-1$ equations can be written as a single equation for $(M-1)$-dimensional column vectors:

$$\mathbf{r} = \mathbf{d} + \mathbf{n}. \tag{4.20}$$

The measurement error $\mathbf{n}$ is assumed to be a multivariate random vector with an $(M-1) \times (M-1)$ positive-definite covariance matrix

$$\mathbf{N} = \mathbb{E}\left[(\mathbf{n} - \mathbb{E}[\mathbf{n}])(\mathbf{n} - \mathbb{E}[\mathbf{n}])^T\right], \tag{4.21}$$

where $E[\cdot]$ denotes the expected value and the superscript T denotes the transpose. As explained above, the time difference measurements in an A-TDOA system are independent, and therefore the error covariance matrix can be expressed as

$$\mathbf{N_{A-TDOA}} = \begin{bmatrix} \sigma_2^2 & 0 & \cdots & 0 \\ 0 & \sigma_3^2 & \cdots & 0 \\ \vdots & \vdots & \ddots & \vdots \\ 0 & 0 & \cdots & \sigma_M^2 \end{bmatrix}, \tag{4.22}$$

while the covariance matrix for a TDOA system is not diagonal due to correlation

between different TDOA measurements:

$$\mathbf{N_{TDOA}} = \begin{bmatrix} \sigma_2^2 + \sigma_1^2 & \sigma_1^2 & \cdots & \sigma_1^2 \\ \sigma_1^2 & \sigma_3^2 + \sigma_1^2 & \cdots & \sigma_1^2 \\ \vdots & \vdots & \ddots & \vdots \\ \sigma_1^2 & \sigma_1^2 & \cdots & \sigma_M^2 + \sigma_1^2 \end{bmatrix}. \tag{4.23}$$

If target node coordinate $\mathbf{x}$ is regarded as an unknown but nonrandom vector, then the conditional density function of $\mathbf{r}$ given $\mathbf{x}$ is

$$p(\mathbf{r}|\mathbf{x}) = \frac{1}{(2\pi)^{\frac{M}{2}}|\mathbf{N}|^{\frac{1}{2}}} \cdot \exp\left\{-\frac{1}{2}[\mathbf{r}-\mathbf{d}]^T\mathbf{N}^{-1}[\mathbf{r}-\mathbf{d}]\right\} \tag{4.24}$$

where $|\mathbf{N}|$ denotes the determinant of $\mathbf{N}$ and the superscript -1 denotes the inverse. Because $\mathbf{N}$ is diagonal, its inverse exists. The maximum likelihood estimator is that value of $\mathbf{x}$ which maximizes (4.24). Thus the maximum likelihood estimator minimizes the quadratic form

$$[\mathbf{r}-\mathbf{d}]^T\mathbf{N}^{-1}[\mathbf{r}-\mathbf{d}]. \tag{4.25}$$

From (4.22) and (4.25), the ML estimator can be obtained as

$$\arg\min_{\mathbf{x}} \sum_{i=2}^{M} \frac{(r_i - \|\mathbf{x}-\mathbf{x}_i\| - \|\mathbf{x}-\mathbf{x}_1\| + \|\mathbf{x}_i-\mathbf{x}_1\|)^2}{\sigma_i^2}. \tag{4.26}$$

Note that the expression of (4.26) is identical to a least squares error function, and the weights are inversely proportional to the variance of the measurements since a larger variance means a less reliable measurement. An example of the A-TDOA MLE cost function is shown in Fig. 4.2.

As can be observed from Fig. 4.2 and (4.26), the MLE objective function is highly non-linear and non-convex, hence an improper selection of the initial guess may lead to a local convergence which is deviated from a global minimal. Next we will be using SDP to relax the non-convex optimization problem to a convex optimization problem to provide approximate position estimation in a globally optimum fashion [73].

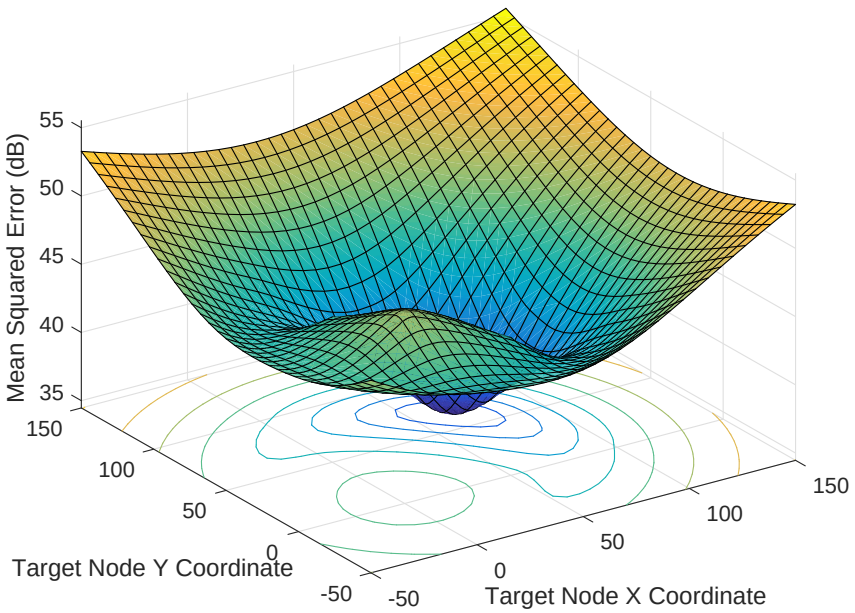

Figure 4.2: MLE cost function of an A-TDOA localization system.

We start by expanding (4.26) as

$$\arg\min_{\mathbf{x}} \sum_{i=2}^{M} \quad \frac{\|\mathbf{x}-\mathbf{x}_i\|^2 + 2\cdot\|\mathbf{x}-\mathbf{x}_i\|\cdot\|\mathbf{x}-\mathbf{x}_1\| + \|\mathbf{x}-\mathbf{x}_1\|^2}{\sigma_i^2} - \frac{2\cdot\|\mathbf{x}-\mathbf{x}_i\|\left(\|\mathbf{x}_i-\mathbf{x}_1\|+r_i\right) + 2\cdot\|\mathbf{x}-\mathbf{x}_1\|\left(\|\mathbf{x}_i-\mathbf{x}_1\|+r_i\right)}{\sigma_i^2} + \frac{r_i^2 + \|\mathbf{x}_i-\mathbf{x}_1\|^2 + 2r_i\|\mathbf{x}_i-\mathbf{x}_1\|}{\sigma_i^2}. \tag{4.27}$$

By denoting $h_i = \|\mathbf{x}-\mathbf{x}_i\|$ and $\mathbf{h} = [h_1, h_2, \cdots, h_M]^T$, and dropping the terms in (4.27) that have no effects on the minimization, the ML cost function can be expressed as

a constrained optimization problem,

$$\arg\min_{\mathbf{x},\mathbf{h}} \sum_{i=2}^{M} \frac{{h_i}^2 + 2\cdot h_i \cdot h_1 + {h_1}^2}{\sigma_i^2} - \frac{2\cdot h_i\left(\|\mathbf{x}_i - \mathbf{x}_1\| + r_i\right) + 2\cdot h_1\left(\|\mathbf{x}_i - \mathbf{x}_1\| + r_i\right)}{\sigma_i^2} \tag{4.28a}$$

subject to:

$$h_i = \|\mathbf{x} - \mathbf{x}_i\|. \tag{4.28b}$$

The cost function in (4.28a) remains nonlinear because of the terms $h_i^2, h_i \cdot h_1$ and h_1^2. By introducing a parameter $\mathbf{H} = \mathbf{h}\mathbf{h}^T$ and letting $h_i h_1 = h_{i1}$, the problem at hand becomes

$$\arg\min_{\mathbf{x},\mathbf{h},\mathbf{R}} \sum_{i=2}^{M} \frac{h_{ii} + 2\cdot h_{i1} + h_{11}}{\sigma_i^2} - \frac{2\cdot h_i\left(\|\mathbf{x}_i - \mathbf{x}_1\| + r_i\right) + 2\cdot h_1\left(\|\mathbf{x}_i - \mathbf{x}_1\| + r_i\right)}{\sigma_i^2} \tag{4.29a}$$

subject to:

$$\mathbf{H} = \mathbf{h}\mathbf{h}^T \tag{4.29b}$$

$$h_{ii} = \mathbf{x}^T\mathbf{x} + \mathbf{x}_i^T\mathbf{x}_i - 2\mathbf{x}_i^T\mathbf{x}, i = 1, 2, \ldots, M. \tag{4.29c}$$

Furthermore, by introducing a new variable $z = \mathbf{x}^T\mathbf{x}$ to linearize constraint (4.29c), the above problem can be relaxed to a standard SDP problem as

$$\arg\min_{\mathbf{x},\mathbf{h},\mathbf{R},z} \sum_{i=2}^{M} \frac{h_{ii} + 2\cdot h_{i1} + h_{11}}{\sigma_i^2} - \frac{2\cdot h_i\left(\|\mathbf{x}_i - \mathbf{x}_1\| + r_i\right) + 2\cdot h_1\left(\|\mathbf{x}_i - \mathbf{x}_1\| + r_i\right)}{\sigma_i^2} \tag{4.30a}$$

subject to:

$$\begin{bmatrix} \mathbf{H} & \mathbf{h} \\ \mathbf{h}^T & 1 \end{bmatrix} \succeq \mathbf{0}_{(m+1)\times(m+1)} \tag{4.30b}$$

$$\begin{bmatrix} z & \mathbf{x}^T \\ \mathbf{x} & \mathbf{I}_2 \end{bmatrix} \succeq \mathbf{0}_{3\times 3} \tag{4.30c}$$

$$h_{ii} = z + \mathbf{x}_i^T\mathbf{x}_i - 2\mathbf{x}_i^T\mathbf{x}, i = 1, 2, \ldots, M, \tag{4.30d}$$

In minimizing the objective function in (4.30a), h_{i1} tends to decrease while h_i and h_1 tend to increase, hence the relaxation made above is not tight. Nevertheless, (4.30) is a convex problem whose global solution can readily be computed. In addition, simulation studies have indicated that the approximate solution to problem (4.30) is typically close to the true location. Based on these, we propose a two-step algorithm in that the SDP solution serves as an initial estimation to allow a Taylor-series based method step a quick convergence to an accurate location estimation.

To describe the Taylor-series based approach, we denote $f_i(\mathbf{x}) = \|\mathbf{x}-\mathbf{x}_i\|+\|\mathbf{x}-\mathbf{x}_1\|$, and express the error function as

$$e_i(\mathbf{x}) = r_i + \|\mathbf{x}_i - \mathbf{x}_1\| - f_i(\mathbf{x}), i = 2, 3, \ldots, M. \tag{4.31}$$

Let $\mathbf{x}_0 = [x_0, y_0]^T$ be the initial guess of the target location and $\Delta\mathbf{x} = [\delta x, \delta y]^T$ be the small increment on $\mathbf{x}$.

By applying Taylor expansion to the equations in (4.31), these equations can be linearized as

$$e_i(\mathbf{x}) \approx r_i + \|\mathbf{x}_i - \mathbf{x}_1\| - f_i(\mathbf{x}_0) - \left.\frac{\partial f_i(\mathbf{x})}{\partial x}\right|_{\mathbf{x}_0} \cdot \delta x - \left.\frac{\partial f_i(\mathbf{x})}{\partial y}\right|_{\mathbf{x}_0} \cdot \delta y, \tag{4.32}$$

which can be expressed in vector form as

$$\mathbf{e} = \mathbf{b} - \mathbf{A} \cdot \boldsymbol{\Delta}\mathbf{x}, \tag{4.33}$$

where

$$\mathbf{A} \triangleq \begin{bmatrix} \frac{\partial f_2(\mathbf{x})}{\partial x} & \frac{\partial f_2(\mathbf{x})}{\partial y} \\ \frac{\partial f_3(\mathbf{x})}{\partial x} & \frac{\partial f_3(\mathbf{x})}{\partial y} \\ \vdots & \vdots \\ \frac{\partial f_M(\mathbf{x})}{\partial x} & \frac{\partial f_M(\mathbf{x})}{\partial y} \end{bmatrix}, \tag{4.34}$$

$$\mathbf{b} \triangleq \begin{bmatrix} r_2 + \|\mathbf{x}_2 - \mathbf{x}_1\| - f_2(\mathbf{x}_0) \\ r_3 + \|\mathbf{x}_3 - \mathbf{x}_1\| - f_3(\mathbf{x}_0) \\ \vdots \\ r_M + \|\mathbf{x}_M - \mathbf{x}_1\| - f_M(\mathbf{x}_0) \end{bmatrix}. \tag{4.35}$$

The least-squares estimate for (4.33) is given by

$$\Delta\mathbf{x} = (\mathbf{A}^\mathbf{T}\mathbf{A})^{-\mathbf{1}}\mathbf{A}^\mathbf{T}\mathbf{b}, \tag{4.36}$$

and the target location is updated to

$$\mathbf{x} = \mathbf{x}_0 + \Delta\mathbf{x}. \tag{4.37}$$

The updated target location is utilized in the next iteration until the magnitude of $\Delta\mathbf{x}$ becomes less than a prescribed tolerance.

4.4 Constrained Least Squares Algorithm

The two-step algorithm presented in Section 4.3 provides accurate solutions at a cost of considerable computational complexity, thus it may not be an ideal approach for applications where computational resources are limited. In this section we present a constrained least-squares estimator that provides good solution accuracy with reduced complexity for A-TDOA positioning systems.

We start by rewriting the error functions in (4.31) in vector forms as

$$\hat{\mathbf{e}}(\mathbf{x}) = \mathbf{A}\mathbf{r} - \mathbf{p}, \tag{4.38a}$$

where

$$\mathbf{A} = \begin{bmatrix} 1 & 1 & 0 & \dots & 0 \\ 1 & 0 & 1 & \dots & 0 \\ \vdots & \vdots & \vdots & \ddots & \vdots \\ 1 & 0 & 0 & \dots & 1 \end{bmatrix}_{(M-1)\times M}, \tag{4.38b}$$

$$\mathbf{r} = \begin{bmatrix} r_1 \\ r_2 \\ \vdots \\ r_M \end{bmatrix}, \tag{4.38c}$$

$$\mathbf{p} = \begin{bmatrix} p_2 \\ p_3 \\ \vdots \\ p_M \end{bmatrix}, \tag{4.38d}$$

with

$$r_i = \|\mathbf{x} - \mathbf{x}_i\|, \tag{4.38e}$$

$$p_i = d_{i1} + \|\mathbf{x}_i - \mathbf{x}_1\|, \tag{4.38f}$$

and d_{i1} representing the measured range differences.

Consequently, the localization problem at hand can be formulated as a constrained least squares problem

$$\min_{\mathbf{x},\mathbf{r}} \|\mathbf{A}\mathbf{r} - \mathbf{p}\|^2 \tag{4.39a}$$

subject to:

$$r_i = \|\mathbf{x} - \mathbf{x}_i\|, i = 1, 2, \cdots, M. \tag{4.39b}$$

Below we propose to solve (4.39) in two steps: the first step treats $\mathbf{r}$ as the variable of (4.39a) only and finds all minimizers $\mathbf{r}^*$ that are parameterized in terms of a free parameter ϕ (see (4.43)); the second step then deals with the constraints in (4.39b).

Let the singular value decomposition [80] of matrix $\mathbf{A}$ be given by

$$\mathbf{A} = \mathbf{U}\mathbf{\Sigma}\mathbf{V}^T, \tag{4.40}$$

where $\mathbf{U} \in \mathcal{R}^{(M-1)\times(M-1)}$ and $\mathbf{V} \in \mathcal{R}^{M\times M}$ are orthogonal matrices. Matrix $\mathbf{\Sigma}$ has the same dimension as matrix $\mathbf{A}$ and is written as

$$\mathbf{\Sigma} = [\mathbf{S}\ \mathbf{0}] = \left[\begin{array}{cccc|c} \sigma_1 & & & & 0 \\ & \sigma_2 & & & 0 \\ & & \ddots & & 0 \\ & & & \sigma_{M-1} & 0 \end{array}\right]_{(M-1)\times M}, \tag{4.41}$$

with $\{\sigma_1, \sigma_2, \cdots, \sigma_{M-1}\} > \mathbf{0}$.

Using (4.40) and (4.41), we can write

$$\begin{aligned} \|\mathbf{A}\mathbf{r} - \mathbf{p}\| &= \|\mathbf{U}\mathbf{\Sigma}\mathbf{V}^T\mathbf{r} - \mathbf{p}\| \\ &= \|\mathbf{U}\| \cdot \|\mathbf{\Sigma}\mathbf{V}^T\mathbf{r} - \mathbf{U}^T\mathbf{p}\| \\ &= \|\mathbf{\Sigma}\mathbf{V}^T\mathbf{r} - \mathbf{U}^T\mathbf{p}\| \\ &= \|\mathbf{\Sigma}\mathbf{z} - \tilde{\mathbf{p}}\| \end{aligned} \tag{4.42}$$

where $\mathbf{z} = \mathbf{V}^T\mathbf{r}$ and $\tilde{\mathbf{p}} = \mathbf{U}^T\mathbf{p}$.

Note that in (4.41) the last column is a $\mathbf{0}$ vector, hence the product of $\mathbf{\Sigma}\mathbf{z}$ is not affected by the last element of the vector $\mathbf{z}$. Therefore we treat the last element

separately in $\mathbf{z}$ and denote

$$\mathbf{z} = \begin{pmatrix} \hat{\mathbf{z}} \\ \phi \end{pmatrix}. \tag{4.43}$$

Then (4.42) becomes

$$\begin{aligned} \|\mathbf{A}\mathbf{r} - \mathbf{p}\| &= \|\mathbf{\Sigma}\mathbf{z} - \tilde{\mathbf{p}}\| \\ &= \|\mathbf{S}\hat{\mathbf{z}} - \tilde{\mathbf{p}}\|. \end{aligned} \tag{4.44}$$

It can be observed that (4.44) reaches its minimum if $\hat{\mathbf{z}} = \mathbf{S^{-1}}\tilde{\mathbf{p}}$, and the optimal $\mathbf{z}$ is given by

$$\mathbf{z}^* = \begin{pmatrix} \mathbf{S^{-1}}\tilde{\mathbf{p}} \\ \phi \end{pmatrix}, \tag{4.45}$$

with ϕ as a free scaler parameter. Therefore the optimal $\mathbf{r}$ for (4.39a) is given by

$$\begin{aligned} \mathbf{r}^* &= \mathbf{V}\mathbf{z}^* \\ &= [\underbrace{\mathbf{V}_1}_{(M\times M-1)} \underbrace{\mathbf{v}_M}_{(M\times 1)}] \begin{bmatrix} \mathbf{S^{-1}}\tilde{\mathbf{p}} \\ \phi \end{bmatrix} \\ &= \mathbf{V}_1\mathbf{S^{-1}}\mathbf{U^T}\mathbf{p} + \mathbf{v}_M\phi \\ &\triangleq \mathbf{r_s} + \mathbf{v}_M\phi \end{aligned} \tag{4.46}$$

where parameter ϕ will be optimally tuned in the next step in dealing with (4.39b).

With the optimal $\mathbf{r}$ determined in (4.46), the constraints in (4.39b) can be written as

$$\mathbf{h}(\mathbf{x}) - \mathbf{v}_M\phi - \mathbf{r_s} = 0, \tag{4.47}$$

where

$$\mathbf{h}(\mathbf{x}) = \begin{bmatrix} \|\mathbf{x} - \mathbf{x}_1\| \\ \|\mathbf{x} - \mathbf{x}_2\| \\ \vdots \\ \|\mathbf{x} - \mathbf{x}_M\| \end{bmatrix}. \tag{4.48}$$

The ℓ_2-optimal approximate solution of (4.47) can be obtained by solving

$$\min_{\mathbf{x},\phi} b(\mathbf{x}, \phi) = \frac{1}{2}\|h(\mathbf{x}) - \mathbf{v}_M\phi - \mathbf{r_s}\|^2. \tag{4.49}$$

Eq.(4.49) is a typical non-linear least squares problem, and it can readily be solved by

Gauss-Newton algorithm [81]. Unlike Newton's method, the Gauss-Newton algorithm can be used to minimize a sum of squared function values, and it has the advantage that second derivatives, which can be challenging to compute, are not required. The Gauss-Newton iteration for minimizing $b(\mathbf{x}, \phi)$ is given by

$$\begin{bmatrix} \mathbf{x}^{k+1} \\ \phi^{k+1} \end{bmatrix} = \begin{bmatrix} \mathbf{x}^{k} \\ \phi^{k} \end{bmatrix} - \alpha_k \cdot \mathbf{H}^{-1}(\mathbf{x}_i) \cdot \nabla b(\mathbf{x}^k, \phi^k) \tag{4.50}$$

where α_k can be determined by an inexact line search [81], and

$$\nabla b(\mathbf{x}^k, \phi^k) = \mathbf{J}^T(\mathbf{x}^k) \cdot (h(\mathbf{x}^k) - \mathbf{v}_M \phi^k - \mathbf{r}_s) \tag{4.51}$$

$$\mathbf{H}(\mathbf{x}^k) = \mathbf{J}^T(\mathbf{x}^k)\mathbf{J}(\mathbf{x}^k) + \epsilon, \tag{4.52}$$

with ϵ a small positive constant, and the Jacobian matrix

$$\mathbf{J}(\mathbf{x}) = \left[\begin{array}{c|c} \frac{\mathbf{x}-\mathbf{x}_1}{\|\mathbf{x}-\mathbf{x}_1\|} & \\ \vdots & -\mathbf{v}_M \\ \frac{\mathbf{x}-\mathbf{x}_M}{\|\mathbf{x}-\mathbf{x}_M\|} & \end{array}\right]. \tag{4.53}$$

We remark that matrix $\mathbf{A}$ in (4.38b) is independent of measurements, hence $\mathbf{V_1}, \mathbf{S}, \mathbf{U}$ and $\mathbf{v}_M$ can be pre-calculated; and for 2-dimensional location problems the Hessian matrix $\mathbf{H}(\mathbf{x}^k)$ is of size 3×3, hence the complexity of computing $\mathbf{H}^{-1}(\mathbf{x}^k)$ as required in (4.50) is insignificant. The algorithm is found insensitive to its initial point $[\mathbf{x}_0^T \ \phi_0]^T$ as long as it is a reasonable one, e.g., $\mathbf{x}_0 = \frac{1}{M}\sum_{i=1}^{M} \mathbf{x}_i$ and $\phi_0 = 0$. Typically the algorithm converges in less than five iterations.

4.5 Simulation Results

Computer simulations have been conducted to corroborate the theoretical development and to evaluate the performance of the two-step and the CLS estimators. Four algorithms, namely, the two-step algorithm, the CLS algorithm, the LLS algorithm, as well as the SDP algorithm are compared. In addition, a comparison to the CRLB is provided to showcase the great accuracy achieved.

We adopted a consistent system geometry as shown in Section 2.2, with four anchor nodes placed at the vertex of a square, i.e., at (0, 0) m, (0, 100) m, (100, 100)

m and (100, 0) m. To fully evaluate the performance of the estimators, the target node is set to sweep a 100 m × 100 m grid with a step size of 1 m moving towards either x or y direction. The starting location is (0, 0) m and the stopping location is (100, 100) m. To solve the SDP problem involved, the convex solver CVX [82] is applied. The initial guess point of the CLS algorithm is set to the mean value of the anchor nodes coordinate $\frac{1}{N} \cdot \sum_{k=1}^{N} \mathbf{x}_k$. Receiver re-selection technique is applied in all simulations to achieve the best possible performance. Mean-square error (MSE), namely

$$\text{MSE} = \mathbb{E}\big\{\|\hat{\mathbf{x}}_k - \mathbf{x}_k\|^2\big\}, \tag{4.54}$$

was employed as the performance measure, with $\mathbf{x}_k$ the k_{th} true target position and $\hat{\mathbf{x}}_k$ its estimation.

Measurement error was assumed to be Gaussian distributed with zero mean. By conducting extensive simulation, we observed that the performance of each estimator varies significantly depending on the measurement error variance. Therefore, we selected three typical error standard deviations, i.e., $\sigma_0 = 0.1$ m, $\sigma_0 = 1$ m and $\sigma_0 = 10$ m to study each estimator's performance under different conditions, where σ_0 is the error standard deviation when the target node is at the center of the square, i.e., at (50, 50)m. Note that the measurement error model is still distance dependent based on (3.6), and the constant K_E is determined by σ_0. In real applications, a relative ranging error is usually more significant than an absolute error. For instance, 0.1 m ranging error in a 1 m distance measurement is considered inaccurate, while the same ranging error in a 100 m distance measurement is considered highly accurate. Therefore, we define a relative error percentage $P_e = \frac{\sigma}{d_0} \times 100\%$, where d_0 is the distance between an anchor to the center of the measurement area, which in our layout is $d_0 = 50\sqrt{2}$.

These three error magnitudes represent three typical real life scenarios:

- Low ranging error ($\sigma_0 \leq 0.1$): The ranging error is within ± 0.2 m in 95% of the time. The relative error percentage is approximately $P_e = 0.1/50\sqrt{(2)} \cdot 100\% = 0.14\%$. Such high ranging accuracy is rarely reported in literature. It was only achieved in carefully controlled experiment environments where high cost and high precision lab instruments were employed [83–85].

- Medium ranging error ($0.1 < \sigma_0 < 10$): The relative error percentage is within 0.14% to 14%. Most published works using TOA, TDOA and two-way ranging

techniques fall within this range [86–91]. As will be shown in Section 5.4, the A-TDOA system belongs to this category as well.

- High ranging error ($\sigma_0 \geq 10$): The ranging error is greater than ± 20 m in 95% of the time. The relative error percentage is greater than 14%. Many system employing RSS ranging method come into this category [7, 92, 93].

To the best of the author's knowledge, there were no other works that thoroughly study the localization algorithm performance according to practical achievable ranging accuracy. This analysis method allows us to fully understand the advantages and disadvantages of each estimators, and hence is of great importance to guide the selection of the algorithms in a real life system.

From Section 4.5.1 to Section 4.5.3, simulated performance of each algorithm under the aforementioned three scenarios are presented. Remarks regarding the two-step algorithm is made in Section 4.5.4. Section 4.5.5 provides a comparison of algorithms with varying error magnitudes. A short conclusion is drawn in Section 4.5.6.

4.5.1 Low Ranging Error Simulation Results

This section presents simulation results with an error standard deviation of 0.1 m in a 100 m $\times$ 100 m area. The relative error percentage is extremely low, and such scenario is not very common in practical systems. Nevertheless, it well represents a system with a high signal to noise ratio.

Fig. 4.3 to Fig. 4.6 demonstrate the simulated MSE for the LLS, SDP, CLS and the two-step estimators. The X- and Y- axis define the position of the target node. Color-coded squares indicate the MSE of the estimators and the cooler the color, the better the accuracy. All four figures use the same color scale for easy comparison. In addition, Table 4.2 provides a summary of the simulated MSE statistics for each estimator.

Table 4.2: Summary of the simulated MSE with a ranging error of 0.1 m.

Low Ranging Error Simulation Results Summary				
	Mean (dB)	STD	Maximum (dB)	Minimum (dB)
LLS	-3.1	0.6	7.6	-8.1
SDP	-2.2	0.5	4.5	-9.9
CLS	-5.1	0.5	3.7	-9.1
Two-step	-9.3	0.2	-5.2	-11.9

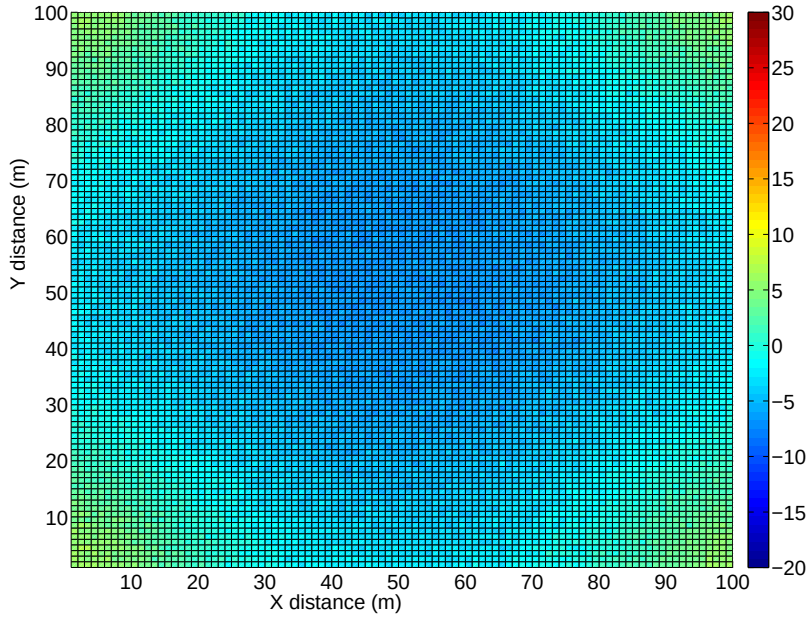

Figure 4.3: MSE of the LLS estimator with a ranging error of 0.1 m.

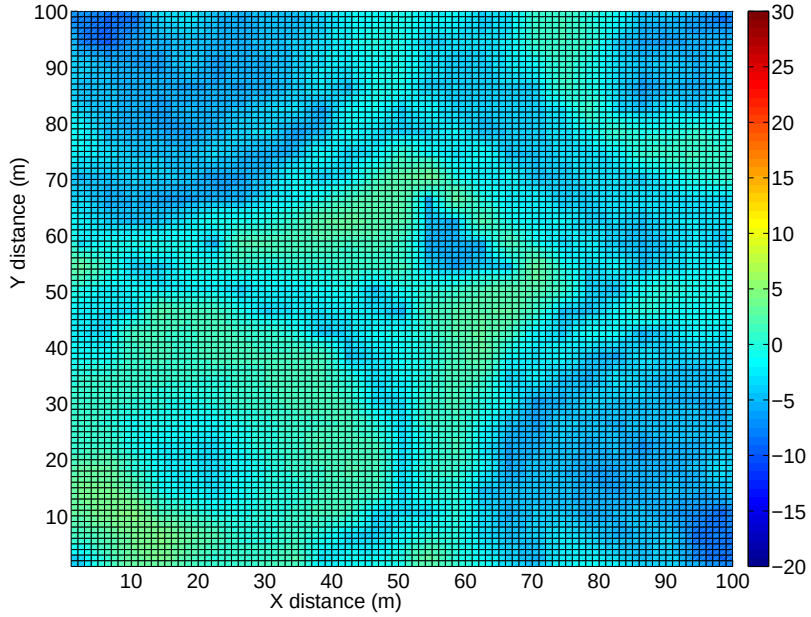

Figure 4.4: MSE of the SDP estimator with a ranging error of 0.1 m.

As observed from Fig. 4.3 to Fig. 4.6, it is very obvious that the two-step (SDP

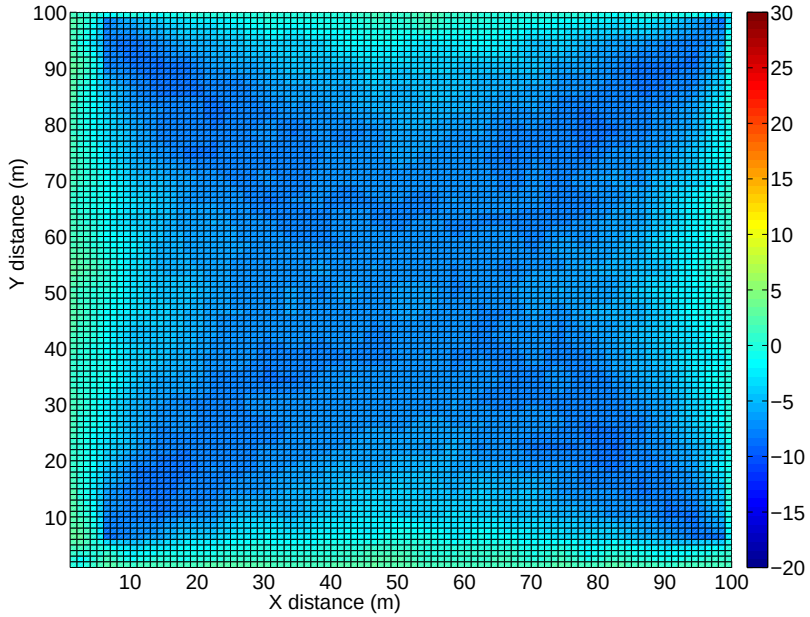

Figure 4.5: MSE of the CLS estimator with a ranging error of 0.1 m.

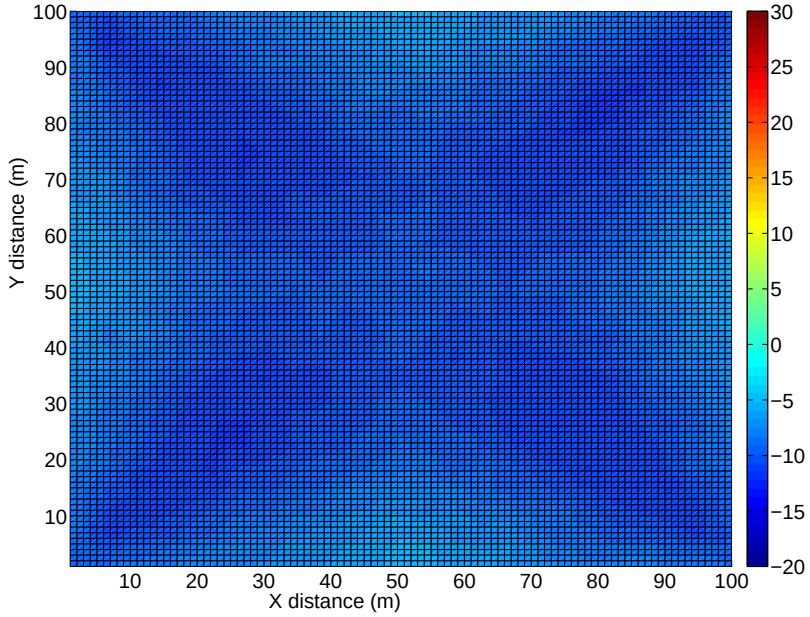

Figure 4.6: MSE of the two-step estimator with a ranging error of 0.1 m.

+ Taylor) estimator outperforms all the other estimators. The average MSE over the

entire 100 m × 100 m grid is several dB lower. In addition, the two-step estimator's performance is rather consistent across the entire area. The CLS estimator has the second lowest MSE in all four estimators. Its average MSE is 4.2 dB higher than the two-step estimator, but 2 dB lower than the LLS estimator. Hence, the CLS estimator is a good compromise between the need for high accuracy and the demands of low complexity. The LLS estimator's performance is reasonably satisfactory given it has the lowest complexity and an analytical solution. It, however, has the worst performance on four corners where the geometric dilution of precision (GDOP) is poor. The SDP estimator performs the worst when the ranging error is low, yet we will see in Section 4.5.3 that it outperforms all the other algorithms when the ranging error is high. Another observation is that the MSE on the 100 m × 100 m square edge is significantly higher than other positions for LLS, CLS and the two-step estimators, and this is consistent with the CRLB as shown in Section 3.2.

4.5.2 Medium Ranging Error Simulation Results

This section presents simulation results with an error standard deviation of 1 m in a 100 m × 100 m area, and it well represents a practical system using time based localization techniques such as TOA, TDOA, and etc. In addition, as will be shown in Section 5.4, the implemented A-TDOA system has a P_e of around 3.6% and fits well in this category.

Fig. 4.7 to Fig. 4.10 demonstrate the simulated MSE for the LLS, SDP, CLS and the two-step estimators and Table 4.3 provides a summary of the simulated MSE statistics for each estimators.

Table 4.3: Summary of the simulated MSE with a ranging error of 1 m.

Medium Ranging Error Simulation Results Summary				
	Mean (dB)	STD	Maximum (dB)	Minimum (dB)
LLS	16.8	0.6	28.3	12.0
SDP	11.8	0.2	15.9	7.4
CLS	17.2	1.0	24.3	10.2
Two-step	10.9	0.2	14.3	8.5

Evidently, the two-step estimator still outperforms all the others, and is still robust regardless of the target location. The SDP estimator performs the worst when the measurement error standard deviation is 0.1 m, however, its superiority is convincingly demonstrated as the error standard deviation increases to 1 m. There is

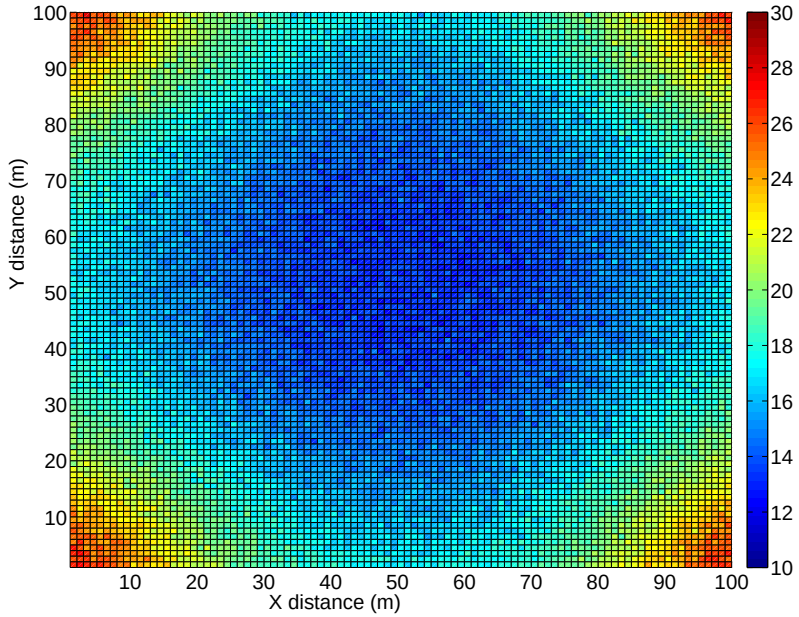

Figure 4.7: MSE of the LLS estimator with a ranging error of 1 m.

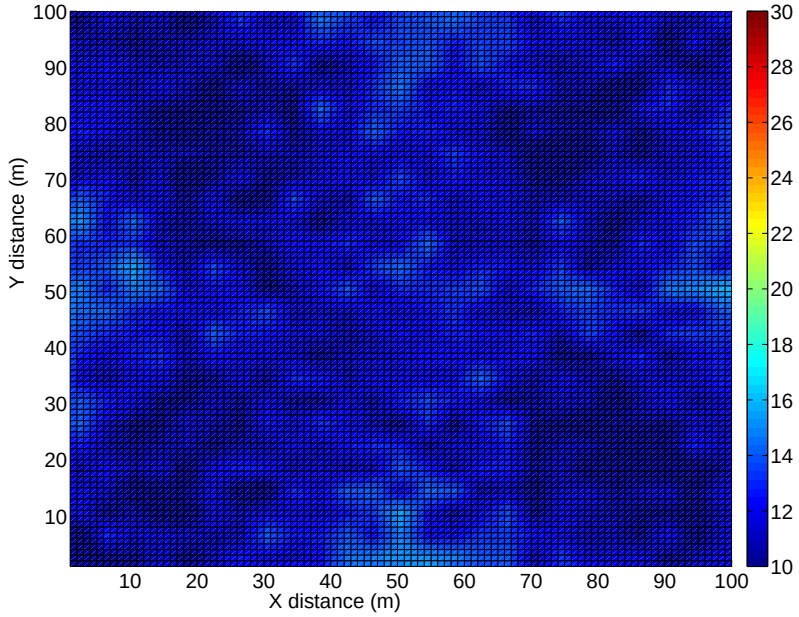

Figure 4.8: MSE of the SDP estimator with a ranging error of 1 m.

only less than 1 dB difference between the SDP and the two-step estimator. The

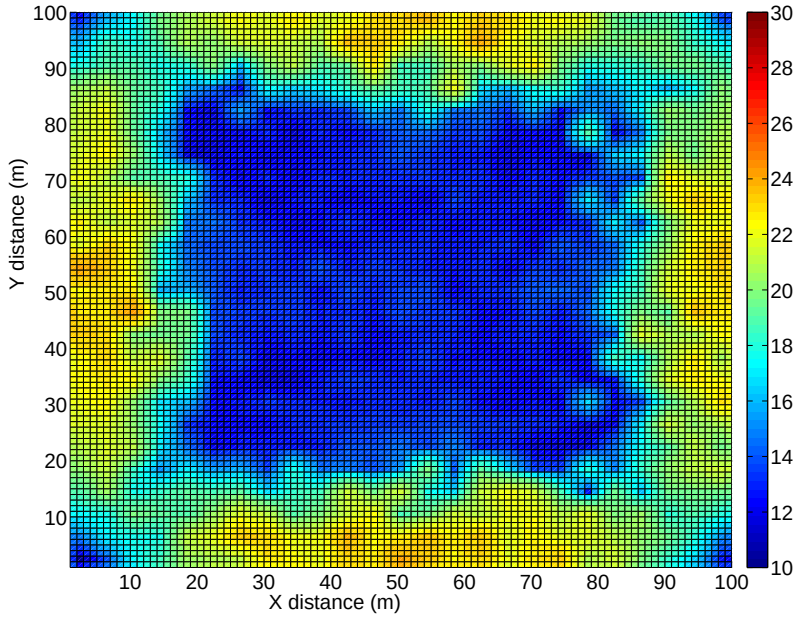

Figure 4.9: MSE of the CLS estimator with a ranging error of 1 m.

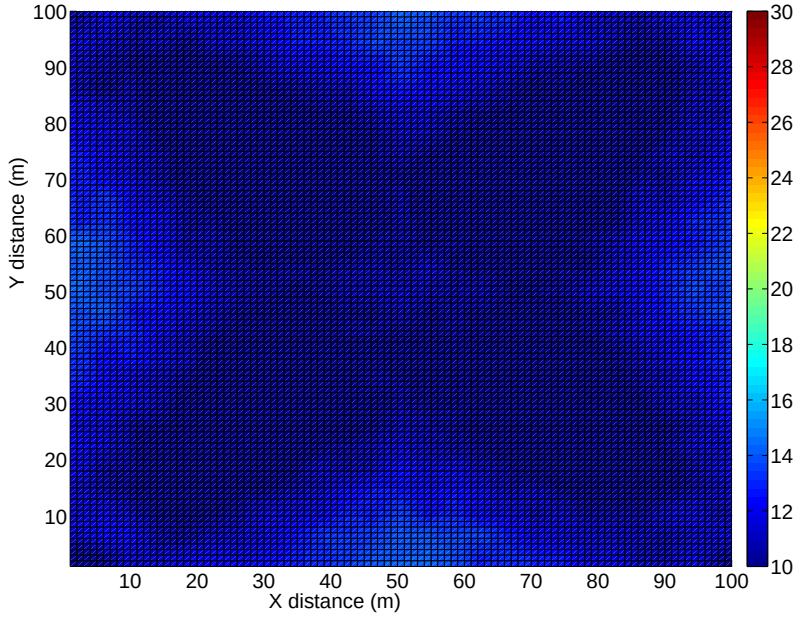

Figure 4.10: MSE of the two-step estimator with a ranging error of 1 m.

average MSE of the LLS and the CLS estimators are comparable, while the CLS

provides a more accurate estimation in the square center, and the LLS is generally better on the edge.

4.5.3 High Ranging Error Simulation Results

This section presents simulation results with an error standard deviation of 10 m in a 100 m $\times$ 100 m area, to study each estimators' performance in a high relative error percentage condition, i.e., $P_e > 14\%$. Although the A-TDOA system generally has less than 14% relative percentage error as shown in Section 5.4, it is still worthwhile to study its performance under high ranging error condition. It is because the wireless channel varies with high dynamic range by shadowing and fading effects, which can cause the ranging accuracy to change significantly.

Fig. 4.11 to Fig. 4.14 demonstrate the simulated MSE for the LLS, SDP, CLS and the two-step estimators and Table 4.4 provides a summary of the simulated MSE statistics for each estimators.

Table 4.4: Summary of the simulated MSE with a ranging error of 10 m.

Medium Ranging Error Simulation Results Summary				
	Mean (dB)	STD	Maximum (dB)	Minimum (dB)
LLS	34.8	1.2	65.2	30.4
SDP	29.4	0.7	34.0	21.5
CLS	33.1	0.4	35.9	28.7
Two-step	31.7	0.9	56.1	28.1

As ranging error increases to 10 m, the SDP estimator's average error becomes 2.3 dB less than the two-step estimator, and hence the SDP estimator is the most accurate among all estimators. Although the two-step estimator loses its leading position under high ranging error condition, it still performs satisfactorily well. However, as shown in Fig. 4.14, at several locations, the positioning error is obviously worse, indicating that the Taylor series method is not very good at combating high ranging error. The CLS estimator performs consistently well regardless of the ranging error level. It has the lowest variation across the 100 m $\times$ 100 m area, showcasing its strong robustness. The LLS estimator does not work well in a high error condition. Its lowest estimation error is comparable to the maximum estimation error of the other estimators. Besides, its estimation error is particularly dependent on the target location.

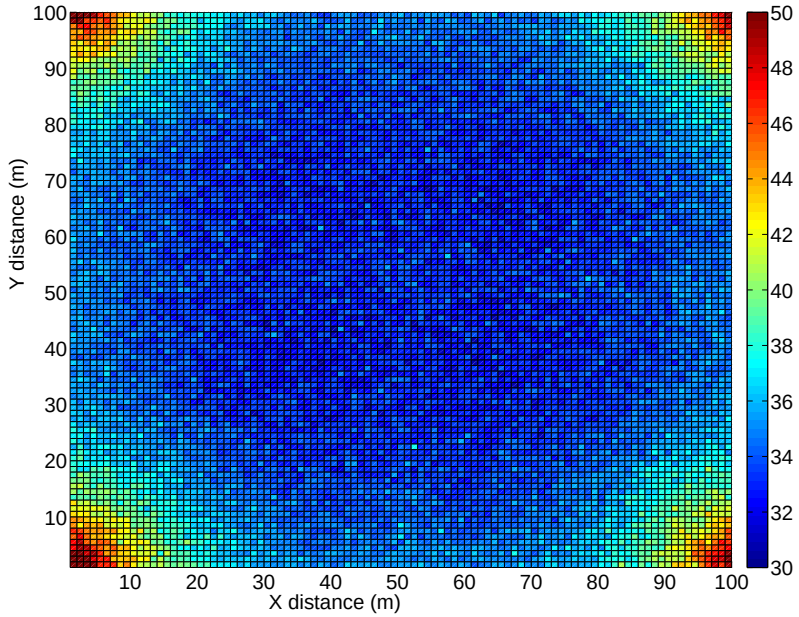

Figure 4.11: MSE of the LLS estimator with a ranging error of 10 m.

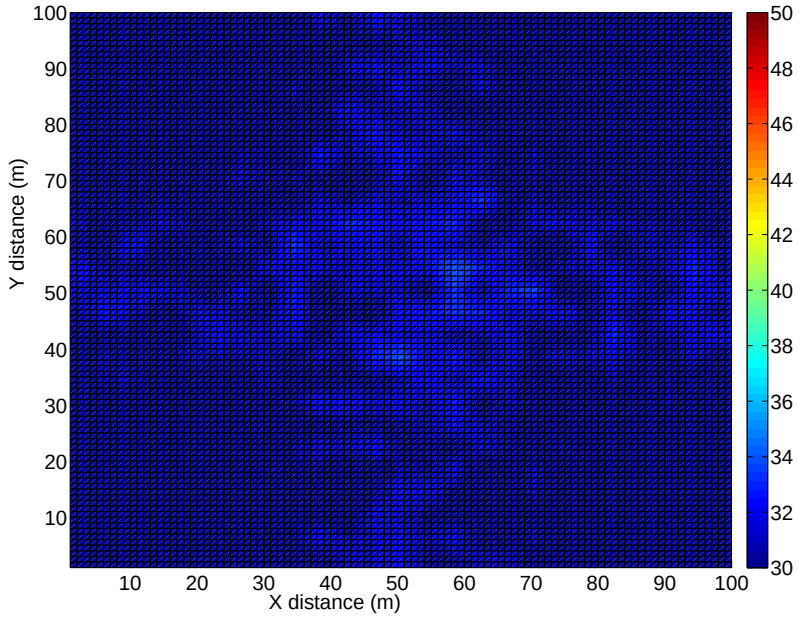

Figure 4.12: MSE of the SDP estimator with a ranging error of 10 m.

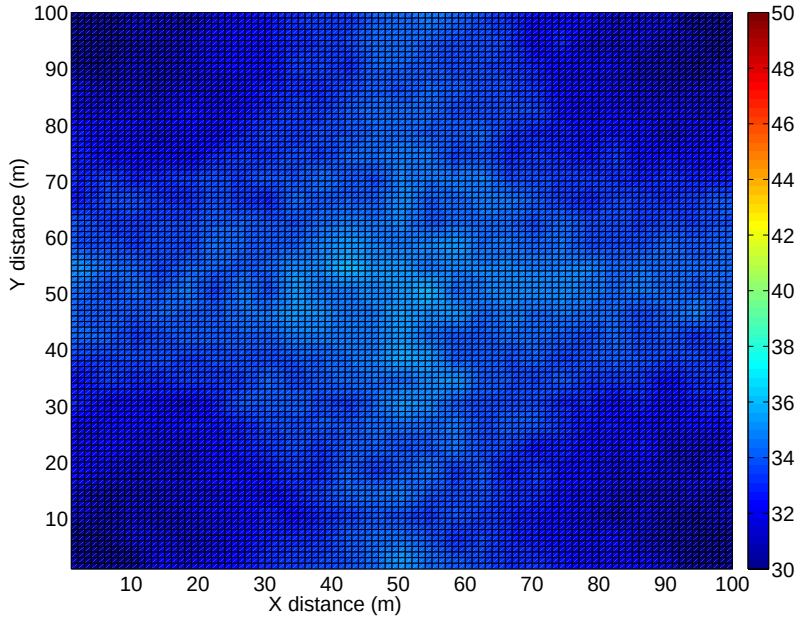

Figure 4.13: MSE of the CLS estimator with a ranging error of 10 m.

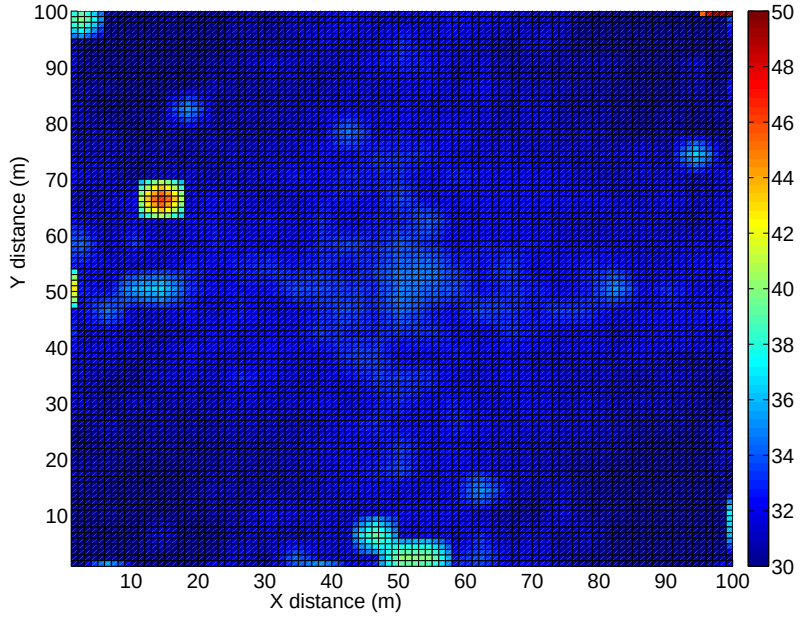

Figure 4.14: MSE of the two-step estimator with a ranging error of 10 m.

4.5.4 Remarks Regarding the Two-step Estimator

As introduced in Section 4.1, the LLS estimator is able to ensure the global convergence, which is the characteristic that is critical to the two-step algorithm. One may argue why use the SDP as opposed to the LLS in the two-step estimator to acquire an initial estimate for the Taylor series estimator? We can find the answer from the simulation results demonstrated in Section 4.5.1 and Section 4.5.2.

When the error standard deviation is low, i.e., $\sigma = 0.1$ m, both LLS and SDP achieve a reasonably accurate estimate, which can be used for the Taylor series estimator to fine search the absolute minimum. Therefore, the performance of a LLS + Taylor and a SDP + Taylor estimators are almost identical, as shown in Fig. 4.15 and Fig. 4.16. Note that we setup a scenario where the possible target node is within a 300 m $\times$ 300 m area, with both X- and Y- axis covering 0 m to 300 m. Four anchor nodes are located at coordinate (100, 100) m, (100, 200) m, (200, 100) m and (200, 200) m. Therefore, the sweeping area is 9 times of that in Section 4.5.1.

As the error standard deviation increases, for instance, when $\sigma = 1$ m, the SDP estimator still achieves a reasonably accurate estimate. However, sometimes, the LLS's estimate is considerably deviated from the true location and causes serious location error. This is demonstrated in Fig. 4.17 and Fig. 4.18. As can be observed from Fig. 4.17, there are several spikes poking out, indicating significant MSE. Therefore, to assure consistently accurate performance, we used the SDP + Taylor estimator, as it is more robust in combating measurement error.

4.5.5 Estimation Accuracy versus Ranging Error

Extensive simulations have been conducted to evaluate the performance of the two-step and the CLS algorithm under varying ranging errors, and to compare their performance against the LLS, SDP and the CRLB. Unlike Section 4.5.1 to Section 4.5.3, we fix the target node location and vary the ranging error magnitude, so we can compare their performance from a different angle.

Fig. 4.19 and Fig. 4.20 depict the MSE versus ranging error standard deviation with the target node located at (30, 40) m and (80, 20) m respectively.

It is observed that when the ranging error is relatively small, the two-step estimator closely follows the CRLB and outperforms the other estimators. When the ranging error becomes large, the two-step estimator's performance is still highly satisfactory. The CLS algorithm achieves high accuracy but with slightly degraded performance

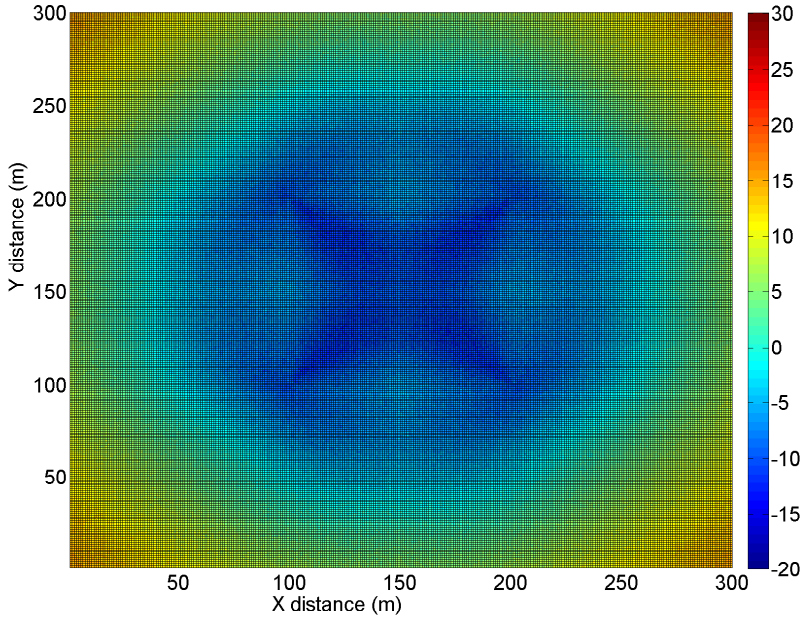

Figure 4.15: MSE of the LLS + Taylor estimator with a ranging error of 0.1 m.

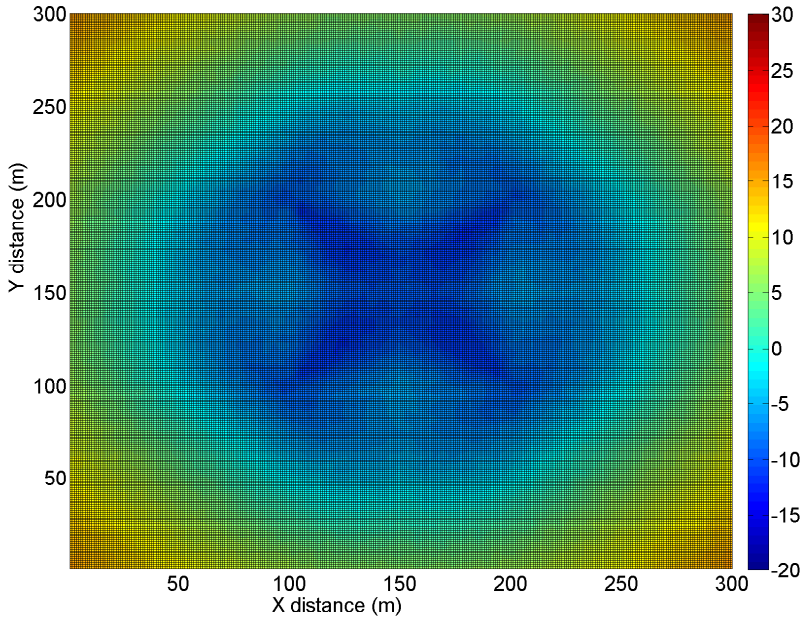

Figure 4.16: MSE of the SDP + Taylor estimator with a ranging error of 0.1 m.

relative to the two-step estimator. The greatest advantage of the CLS estimator is

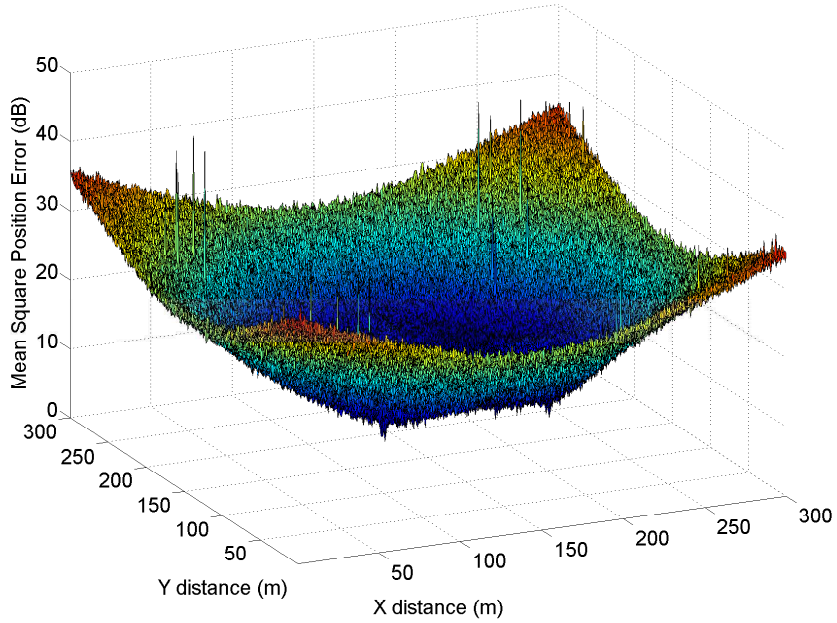

Figure 4.17: MSE of the LLS + Taylor estimator with a ranging error of 1 m.

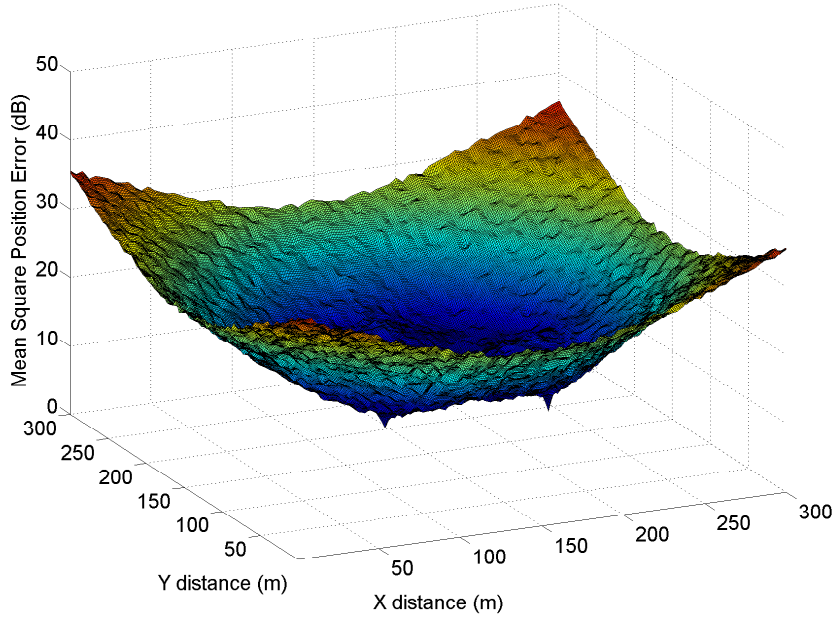

Figure 4.18: MSE of the SDP + Taylor estimator with a ranging error of 1 m.

its simplicity and relatively good performance. In addition, its fast convergence adds

high potential for real-time tracking. The SPD estimator performs poorly when the ranging error is below -7 dB, but at high ranging error condition, it achieves better accuracy than the two-step estimator and the others. The LLS estimator's MSE curve is almost a straight line, implying its accuracy being tightly dependent on the ranging error. In general, the LLS estimator's performance is poor.

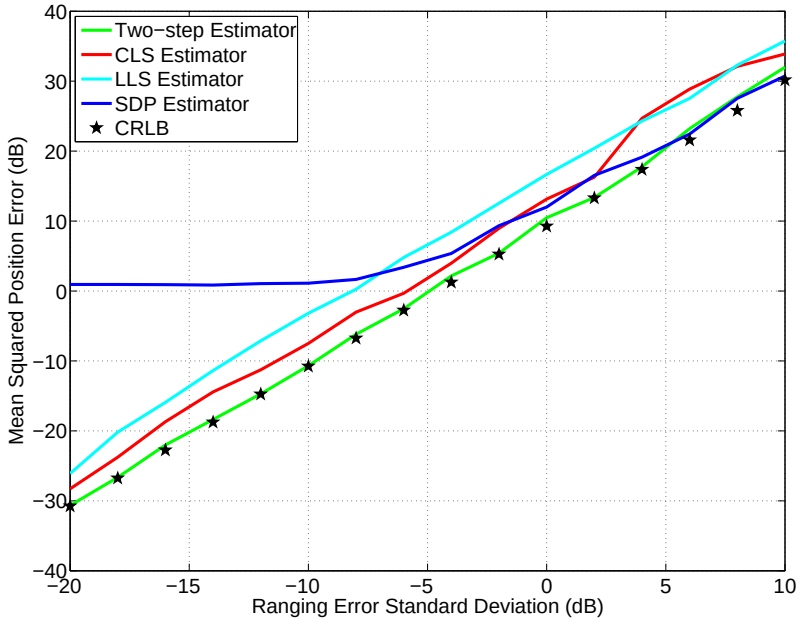

Figure 4.19: Algorithms comparison measured at (30 m, 40 m).

4.5.6 Simulation Summary

Simulation results indicate that the proposed two new estimators, namely, the two-step and the CLS estimator, are able to achieve great performance regardless of the measurement error level. For the time based localization systems, such as TOA, TDOA, A-TDOA, and so on, the ranging error is relatively low, and under this condition, the two-step estimator achieves the best accuracy. In addition, its estimation accuracy is quite consistent regardless of the target node location. The CLS estimator's performance is slightly worse than the two-step estimator, nevertheless, it consumes less CPU time and requires lower computational complexity. In this regard, these two algorithms may be considered as a complementary pair of solution tools that provide the system designer with more than one option for an appropriate

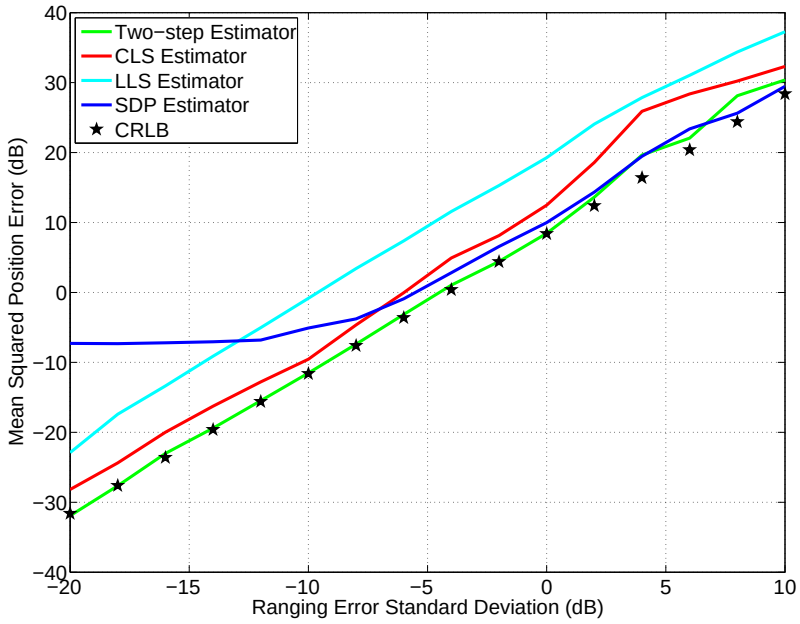

Figure 4.20: Algorithms comparison measured at (80 m, 20 m).

trade-off between accuracy and complexity.

Accuracy is an important but not the only standard to evaluate the performance of various estimators. Table 4.5 summarizes the major properties of each estimator to present a comprehensive review of the different estimators. The system designer should choose the most fitted algorithm that leaves sufficient margin without overkill.

Table 4.5: Localization algorithms comparison.

Algorithm	Closed-form expression	Computational Complexity	Accuracy
LLS	Yes	Low	Low
SDP	No	High	Low when ranging error is small. High when ranging error is large.
Two-step	No	High	High
CLS	No	Low	Medium

Chapter 5

A-TDOA System Implementation

A prototype system is presented in this chapter with the aim to provide an experimental characterization of the proposed A-TDOA positioning system. The requirements for the system development have essentially been low cost and low complexity. Furthermore, the complete prototype is realized by designing its fundamental building blocks based on elementary off-the-shelf components. To achieve accurate performance, the impulse UWB technology is used.

5.1 Introduction

The aforementioned localization methods such as RSS, AOA, TOA and TDOA are applied in various localization platforms. The RSS method is attractive because the signal strength indicator is readily available in existing radio hardware and no additional localization infrastructures are required. However, its localization accuracy is relatively low and [94] reports a median localization error of 10 feet and 97th percentile of 30 feet being an expected bound when a good algorithm and much sampling are applied. The AOA method is not widely used mainly due to its system complexity. That is, a common approach to obtain AOA measurements is to use an antenna array on each anchor node [39]. Besides, the AOA measurement is significantly biased in an NLOS radio environment. The most commonly used and studied methods are time-based localization techniques thanks to their high accuracy. However, both TOA and TDOA approaches require perfect clock synchronization which is hard to realize. As a result, many researches choose to adopt a two-way ranging technique [95], [96] to implement an experimental platform. The two-way ranging eliminates the error

due to imperfect synchronization between nodes, yet this approach is sensitive to clock non-idealities as pointed out in [2] and [3]. Propagation delay is typically on the order of tens of ns while the response delay can be of a few microseconds due to bit synchronization and channel estimation delays. Therefore a small clock offset between the target and anchor nodes could cause a large error. Generally, the further down in the communication protocol stack to draw the response delay, the smaller the time variation. The presented A-TDOA prototype implements a processing delay in physical layer to minimize delay variation.

Ultra-wideband impulse radio (UWB-IR) has several unique characteristics that make it an ideal candidate for time-based localization systems. The impulse signal is spread over a large frequency bandwidth, hence it benefits from very high temporal resolution. For instance, a time resolution on the order of hundreds of picoseconds translates to a spatial resolution on the order of centimeters. Also, the very fine time resolution allows a direct path to be easily distinguished from the reflected paths. This is of paramount importance in indoor environments where other localization systems suffer from the multipath phenomenon. In addition, for sub-GHz UWB systems, the presence of low frequency components in the signal spectrum enables better penetration through the walls. While an UWB system has great potential to achieve centimeter accuracy, it also brings in new challenges for the transceiver design. For example, a low insertion loss L-C matching circuit cannot cover sufficient bandwidth, and a high loss resistive matching becomes inevitable. In addition, although coherent receivers are rather typical in data communications, it gets particularly complicated in an UWB system as it is difficult to implement cross-correlation either in analog or digital domain. Hence, many researches chose to use non-coherent energy detection based architectures [97], [98].

Drawing accurate position is not straightforward, particularly in an asynchronous wireless environment. The aim of this chapter is to present an A-TDOA localization platform and experimentally characterize its performance in a variety of radio environments. The complete design process was conducted in house using commercial off-the-shelf (COTS) components, including antenna, pulse generator, receiver and target node designs. These blocks have been developed from scratch and undergone fairly extensive modification. To the extent of the authors' knowledge, this is the first realized platform that is designed to verify the A-TDOA localization system. Also, different from many proof-of-concept prototypes found in the literature, this platform is self-contained, i.e., no external modules and equipment are required to initiate test,

capture results and process data. In addition, significant efforts have been devoted to designing a low complexity and low power architecture, making the platform highly portable and battery operated. Moreover, the platform has been extensively tested in different radio environments, including outdoor residential area and indoor laboratory, and the results collected in these environments are presented in this thesis. It achieves superior localization precision and behaves robustly. Ultimately, localization errors due to thermal noise, hardware limitation, and radio propagation channel are investigated, and mitigation methods are proposed to further improve the performance.

5.2 Related Work

The wide and diverse range of location-based applications and services has led to a growing academic and business interest in researching and developing various positioning systems during the last decade. Papers [99, 100] provide readers with a comprehensive review of the wireless localization techniques, together with a comparison and performance evaluation of numerous systems, including both commercial products and research-oriented solutions. Fundamental limit of localization accuracy for an UWB system operating in dense cluttered environments was derived in [101]. Nowadays, internet-of-things (IOTs) applications are becoming particularly popular and many of them require location awareness. Cooperative localization technology is a great potential enabler, and as a consequence, researchers have studied it extensively [102, 103]. The application of the precise localization system also stimulates considerable interest in commercial society, such as [104] and [105].

Despite extensive research efforts on UWB ranging and localization modeling and simulation, knowledge about practical implementations is limited. Nonetheless, there are research groups who have implemented prototypes and reported measurement results. In [106], a commercial UWB localization system from Ubisense was mounted on top of several robots to evaluate the localization performance. The study shows that the performance is heavily affected by the dynamics of the radio environment, which is in line with our observation and analysis. Both [107] and [108] employ high speed four channel oscilloscope as a receiver for the deployed TDOA system. Due to that all channels within the oscilloscope are inherently synchronized, it skips the challenging design obstacle of time synchronization. With a high speed oscilloscope, although it is easier to identify the critical timing of the input signal, it is not suitable

for commercialization. Similarly, the platform presented in [109] uses a FPGA to sequentially trigger four transmitters to emit pulses as well as providing trigger signal to the receiver, which in this platform is an oscilloscope. This setup essentially is a fully wired synchronous network, and it completely omits the clock synchronization challenge that a practical TOA based localization system shall face.

IEEE 802.15.4a compliant UWB RFICs are used in implementing the localization systems in [110] and [111]. Both platforms use the decaWave DWM1000 transceiver module which is optimized for indoor precision location and data communications for real time location systems (RTLS) and wireless sensor networks (WSN). Implementations in [112] and [113] are considered down-scaled versions of real systems as they require very high sampling rates ADC that are not realistic in practical applications. Both platforms use more than 2 Gsamples/s ADCs. ADCs at this high rate and resolution are expensive and power-consuming. Besides, it also drives a need of high speed processing capability to process the great amount of ADC samples. The advantage, as indicated by the author, is the flexibility to accommodate various estimation algorithms.

One of the widely used and practical architectures is non-coherent energy detection. Several prototypes [96, 114, 115] are based on this technique and so is the work presented in this thesis. It has very low complexity and power consumption while achieving relatively good performance. The drawback though is that it is more vulnerable to multipath fading than a high sampling based architecture. Other than impulse based (carrier-free) UWB and carrier-based UWB technology, frequency modulated continuous wave (FMCW) radar principle is also used in a positioning system. In [116], a FMCW system is described to achieve a ranging error less than 20 cm in 91 percent of cases. To achieve millimeter order accuracy, a high speed sampling system is required. Instead of using an ultra-high speed ADC, [83] applies an equivalent time sampling technique to effectively reduce ADC sampling rate. The drawback, though, is lower update rate, as the target node must remain its position for many periods. Besides, high stability oscillators must be used to maintain accurate timing reference. For the completeness of the review, a non-UWB but relatively wide bandwidth localization platform is included for comparison [117]. It operates at 2.4GHz industrial scientific and medical (ISM) frequency band and occupies 125 MHz bandwidth using a wireless LAN RFIC. It achieves better than 0.5 m accuracy 85 percent and 65 percent of the time in LOS and NLOS environments respectively. The major drawback of this system is that it is very susceptible to other 2.4 GHz radio interferences, such

as Wi-Fi and Bluetooth.

The accuracy achieved in this work is comparable to the above mentioned platforms, with the advantage of having a fully integrated system instead of using oscilloscopes and transceiver modules. Moreover, all building blocks are developed and optimized in house to achieve a low complexity and low power consumption system design. It is worthwhile to emphasize that the work presented in this thesis is the first implemented A-TDOA prototype to the best of our knowledge.

5.3 System Overview

This section gives the insight into the A-TDOA system architecture and basic operations, as well as a detailed description of each building block.

5.3.1 System Architecture

The A-TDOA system architecture is shown in Fig. 5.1. It contains three major building blocks, namely, an anchor Tx, a target node, and an anchor Rx. The implementation details of these three building blocks as well as the antenna are studied and presented in subsequent sections.

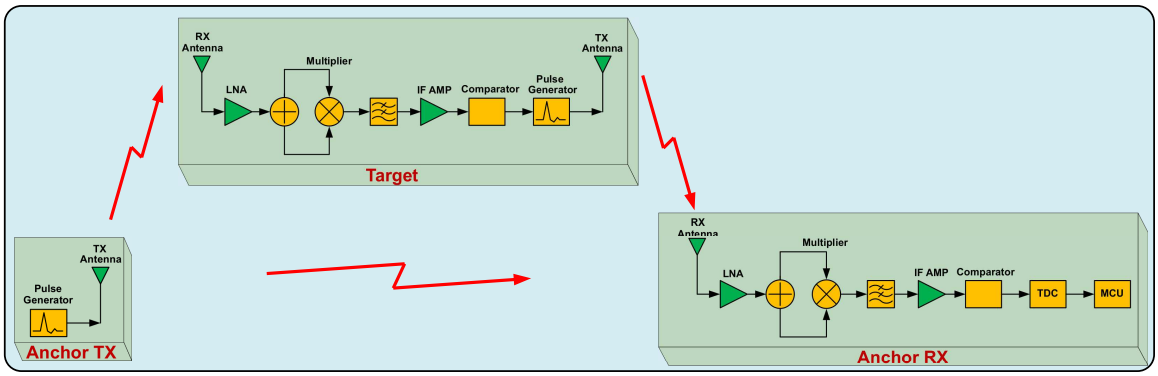

Figure 5.1: A-TDOA system architecture.

There are two ways to achieve re-transmission at the target node. One is to "reflect" the incoming signal, and the other is to "receive and re-transmit" the signal. To "reflect" the incoming signal, one can take advantage of impedance mismatch of a transmission line to bounce the incoming signal back. An antenna with an open-ended transmission line can be used as a reflector. However, in reality, due to the

return loss and insertion loss of the reflector, the received signal at the anchor Rx is rather weak, and hence it poses significant challenge to the anchor Rx design to have high dynamic range. The anchor Rx design was based on energy detection, and when the received signal amplitude is too weak, the detector suffers severely from noise and causes significant ranging error. One effective method is to use high speed ADC to sample the received signal a number of times and apply time average in order to raise the SNR. However, a high speed ADC is quite costly and consumes large amount of power, which contradicts the goal of the A-TDOA system being low cost and low power consumption. Furthermore, the simple signal reflection method has been verified not working well in lab environment. Consequently, we decided to implement a "receive and re-transmit" target node which is more complicated yet robust.

5.3.2 Anchor Tx Implementation

The A-TDOA system adopts a very low power, self-contained transmitter design, which consists of a pulse generator and a transmitting antenna. The transmitter is powered by a 1.5 V AA battery, and does not require an external trigger to operate. This enables a simple and fast deployment of the A-TDOA localization system.

There are several practical approaches to implement a sub-nanosecond pulse generator which can be potentially employed in a positioning system. Six pulse generator prototypes were implemented and evaluated in [118]. We carefully selected the avalanche pulse generator for the following reasons:

- It does not require an external trigger signal, and therefore it is self-contained. Having said that, it can be configured to react on a trigger signal when multiple user access control is required.
- The pulse repetition time T_r can be easily adjusted by changing the circuit's time constant.
- It has a -10 dB bandwidth covering from DC to 1 GHz, and therefore, it does not require an up-conversion circuit. In addition, it avoids the LO feed-through problem reported in [118].
- It has a peak amplitude of 17 V, and therefore it does not require a power amplifier to further boost up the signal power. This allows a significant power saving compared to other designs.

- With a boost converter, it can operate on a 1.5 V AA battery for days.

The pulse generator is based on the transistor avalanche mode operation. To operate in the avalanche mode, a transistor is biased such that the collector-to-emitter voltage is beyond the collector-to-emitter breakdown voltage. Operating in the breakdown region allows the transistor to switch very high currents within less than a nanosecond. The detailed operating principal of an avalanche pulse generator can be found in [119].

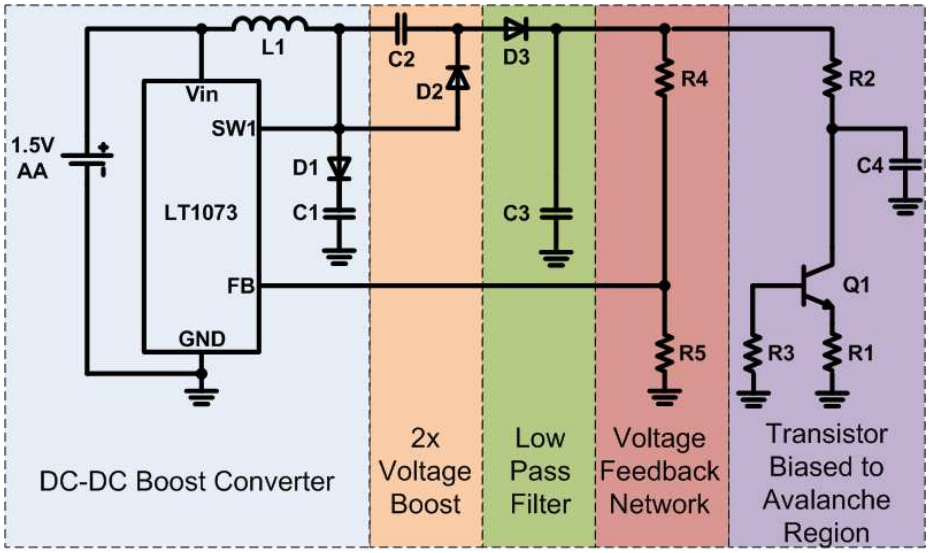

Figure 5.2: Pulse generator schematic.

The schematic of the pulse generator is shown in Fig. 5.2. The design is based on Jim Williams classic application note [120]. The LT1073 DC-DC switching regulator and associated components supply the necessary high voltage to bias the transistor to avalanche breakdown region. The LT1073 forms a flyback voltage boost regulator with L1, D1 and C1. Inductor L1 periodically receives charge and its flyback discharge delivers high voltage to the step-up network. Due to that the voltage on SW1 pin cannot exceed 50 V [121], a voltage step-up network is employed to double the output voltage. The voltage doubler circuit is comprised of C2 and D2. A low pass filter (D3 and C3) then follows to convert the switching signal to a DC voltage, of which a portion is fed back to the LT1073 FB pin via R4 and R5 voltage divider network to close the control loop. This circuit boosts up the input 1.5 V voltage to approximately 90 V to supply the avalanche pulse generator.

The circuit in purple block forms an avalanche pulse generator. Capacitor C4

gets charged via R2 and then rapidly discharges when the collector-emitter voltage reaches the avalanche breakdown voltage. The discharge current flows through R1 during the avalanche and forms a fast-rise pulse between ground and the emitter. For the duration of the output pulse, over 1 amp current flows through Q1. Following the breakdown, C4 discharges and Q1's collector voltage falls below the breakdown voltage and the avalanche operation ceases. C4 is then recharged until breakdown occurs again.

The RC constant ($R2 \times C4$) determines the repetition frequency, and it can be adjusted to have a pulse repetition time T_r greater than the channel delay spread T_d to prevent interference between pulses. In our design, the repetition period is about 30 us, which is sufficiently large to accommodate most of the indoor and small range outdoor environment. Resistor R1 is chosen to match the characteristic impedance of the load, which in this case, is the transmitting antenna, therefore, R1 is set to 50 ohm.

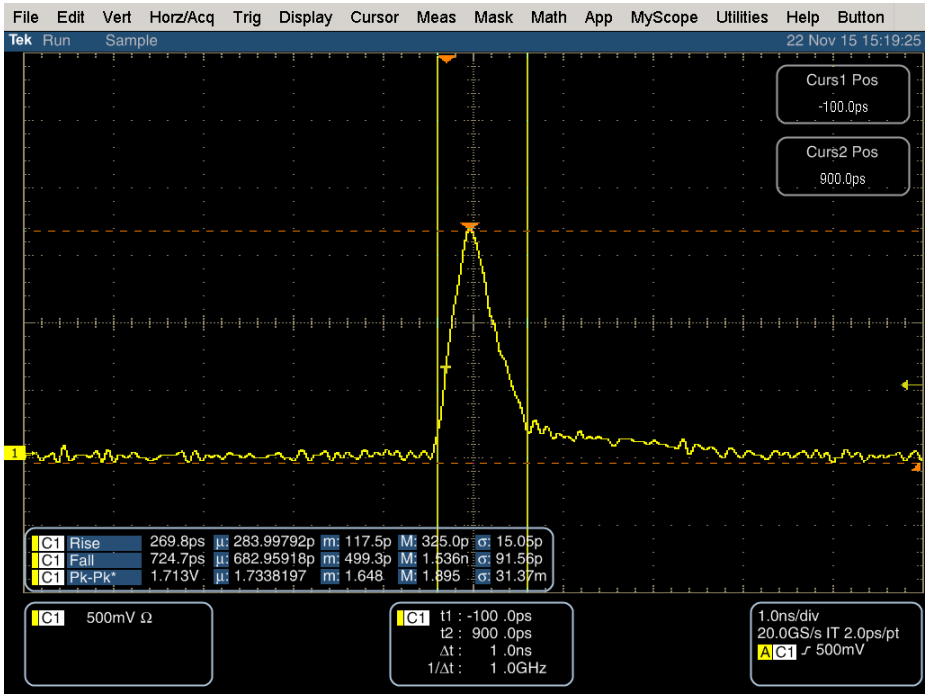

Figure 5.3: Pulse generator output (time domain).

The pulse generator output is shown in Fig. 5.3. An ultra-high speed sampling oscilloscope with 10 GHz analog bandwidth was used to measure the time domain signal. As can be observed from Fig. 5.3, the rise time and fall time are about 270 ps and 725 ps respectively. To prevent the oscilloscope from damaging, a 20 dB

wideband attenuator is inserted between the pulse generator and the input of the equipment. With the attenuator, the measured peak-peak voltage (Vpp) is 1.7 V, which suggests the transmitted pulse has a Vpp of 17 V.

Figure 5.4: Pulse generator output (frequency domain).

The signal spectrum at the output of the pulse generator has been measured with an Agilent N9030A PXA spectrum analyzer and is shown in Fig. 5.4. It shows that the -10 dB bandwidth is about 1 GHz. Operating at sub-GHz band offers several benefits, such as better obstacles penetration capability, simpler architecture and lower power consumption. It is worth emphasizing that the goal is to design a low cost and low power A-TDOA system, and by operating at baseband, it saves an up-converter for the transmitter and a down-converter for the receiver. Both up- and down- converter consist of a mixer and a local oscillator which is usually made up of a phase locked loop (PLL) and a voltage controlled oscillator (VCO) to produce stable tunable frequency outputs. Excluding a converter allows us to minimize the cost and power consumption. Nevertheless, the disadvantage is that the antenna size becomes inevitably large.

5.3.3 Anchor Rx Implementation

There are mainly three receiver architectures for UWB impulse radios: non-coherent energy detection, coherent correlation reception, and transmitted reference (TR). The non-coherent energy detection method requires a relatively high SNR, but it neither needs Nyquist speed sampling nor knowledge about the wireless channel. The coherent approach, on the other hand, is particularly complicated due to the precise phase synchronization and channel estimation requirements. The transmitted reference can be considered as a hybrid method of the aforementioned two. It transmits a reference and data signal pair separated in time. The reference signal is involved for the purpose of determining the channel response. A simple cross-correlation receiver can be applied to correlate the received data signal with the reference signal without requiring additional channel estimation and Rake reception [122, 123].

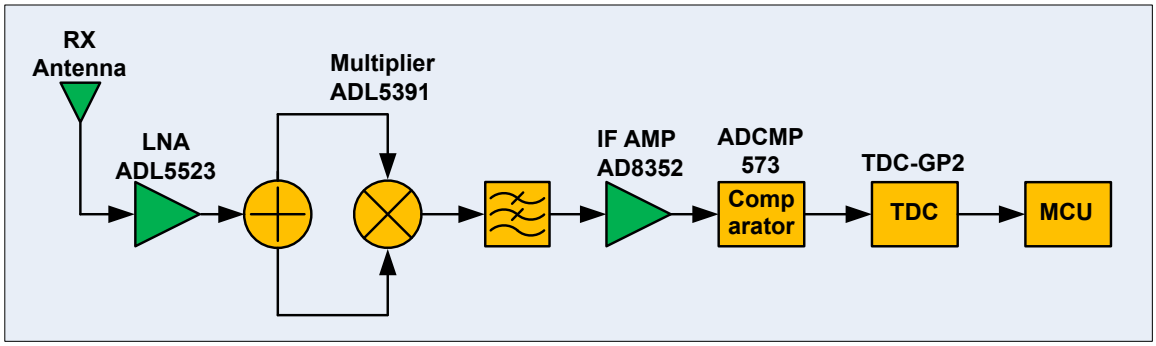

Figure 5.5: Anchor Rx architecture.

The implemented receiver architecture is shown in Fig. 5.5. We adopted a low complexity and low power energy detection approach for the receiver design. Due to its simplicity and practicalities, it is widely studied in the literature and implemented in prototypes [97, 124]. The TR system is also a good candidate; nevertheless, it requires complicated transmitter design to emit a pulse pair. The non-coherent receiver architecture used in our design is implemented purely in analog domain and it cannot provide any processing gain. A processing gain can be obtained by using high speed ADC to sample the analog waveform and apply time average or other SNR boost techniques. Nevertheless, to meet the criteria of the Nyquist sampling theorem, the ADC sampling rate must exceed twice the signal bandwidth. A high speed ADC is extremely costly and it consumes significant amount of power, and hence we have to make a trade-off between performance and cost/power. Given our design target is low cost and low power consumption, we decided to exclude ADCs.

The receiver chain has approximately 64 dB voltage gains which are distributed nearly evenly in RF and baseband domains. Having significant amount of gains in RF can reduce system noise figure, but with more than 50 dB of gains may introduce stability difficulties within amplification chain [125]. On the other hand, providing considerable gains in baseband domain is relatively easier and cheaper, but it requires the square law device to have sufficient SNR. Therefore, to compromise performance and cost, we allocate about 32 dB gain at RF domain, and another 32 dB gain at baseband domain. The anchor Rx design is rather complicated, and we break it down to several blocks and each block is described thoroughly below.

Low Noise Amplifier

After the antenna, the incoming signal is amplified by two stages of low noise amplifiers (LNA). Typically a lumped L-C matching circuit is applied in narrow band communication systems thanks to its low insertion loss and good return loss. However, according to the famous Bode-Fano equation, there is a fundamental limit to the bandwidth achievable [126]. Therefore, to achieve an ultra-wide bandwidth matching for the LNA input, a resistive matching circuit is a must. The resistive matching network can achieve a very wide bandwidth, but it has an obvious drawback of high insertion loss. We used a T matching circuit in our design and the ADS s-parameter simulation bench setup is shown in Fig. 5.6.

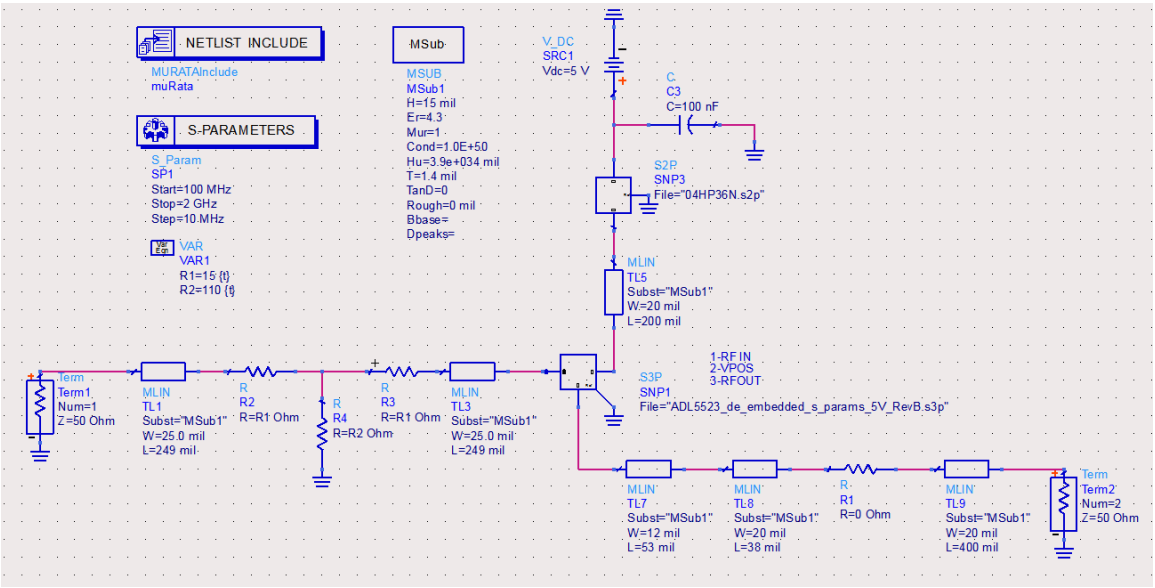

Figure 5.6: ADS test bench for LNA matching.

Simulated S11 and S22 results are shown in Fig. 5.7 and Fig. 5.8 respectively. Both S11 and S22 are below -10 dB from about 200 MHz to 1.6 GHz which covers the whole operation range.

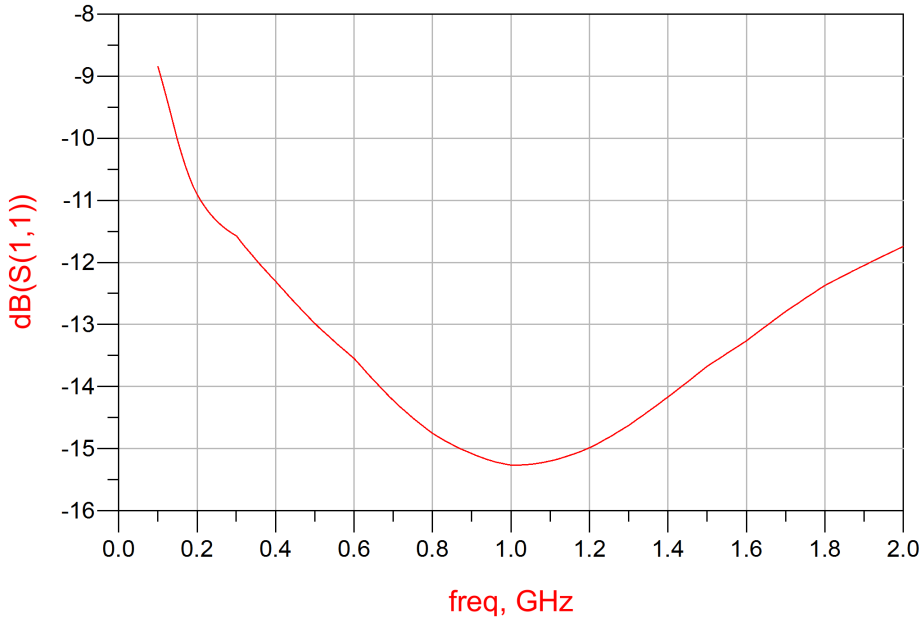

Figure 5.7: Simulated LNA S11 parameter.

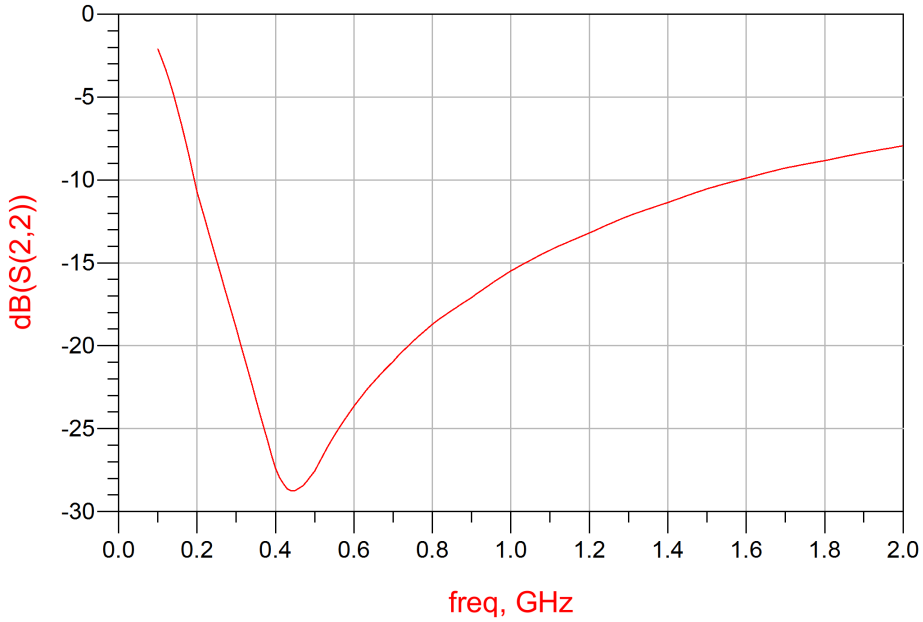

Figure 5.8: Simulated LNA S22 parameter.

The simulated transfer gain, S21, is shown in Fig. 5.9. With a resistive matching network, the LNA only provides approximately 16 dB voltage gain for the band of interest, even though the LNA is rated 21 dB gain at 900 MHz. Therefore, we cascaded two stages of LNA to provide about 32 dB of voltage gain.

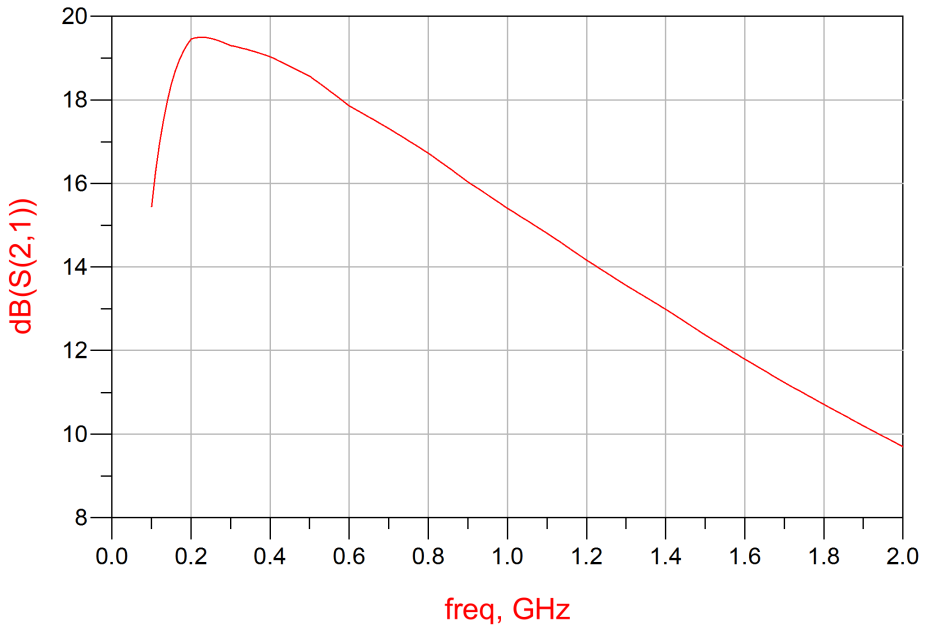

Figure 5.9: Simulated LNA S21 parameter.

Due to the resistive matching, the achievable LNA gain is reduced by 5 dB, and correspondingly the first LNA's noise figure (NF) is increased by about 5 dB. With two cascaded LNAs, the total gain is 32 dB with 6.3 dB of NF.

Wireless receivers suffer from large varying input signal levels, and as a consequence, the multiplier output can become very small such that it is swamped by the multiplier's output noise. To prevent it from happening, sufficient gains must be applied in front of the multiplier. In this design, the multiplier ADL5391 has -138 dBm/Hz output noise density, and the thermal noise level in front of the multiplier is

$$-174 + 32 + 6.3 = -135.7 \text{ dBm/Hz} \tag{5.1}$$

where -174 dBm/Hz is the thermal noise floor at room temperature. The noise is 2.3 dB higher than the multiplier output noise, and hence, the multiplier contributes

about 2 dB to the noise floor:

$$10 \cdot \log_{10}\left(10^{-\frac{135.7}{10}} + 10^{-\frac{138}{10}}\right) = -133.7 \text{ dBm/Hz} \tag{5.2}$$

Ideally if the thermal noise floor in front of the multiplier is 10 dB higher than the multiplier's noise floor, there will be negligible noise contribution due to the multiplier, and therefore no SNR degradation. Nevertheless, 2 dB SNR degradation is acceptable given the input SNR is typically tens of dB. For example, even if the input signal level is only 1 mV RMS, the SNR at the multiplier input is:

$$10 \cdot \log_{10}\left(\frac{0.001^2}{50} \cdot 1000\right) - \left(-135.7 + 10 \cdot \log_{10}10^9\right) + 32 = 30.7 \text{ dB} \tag{5.3}$$

where 50 ohm is the antenna impedance, 10^9 Hz is the signal bandwidth, and 32 is the LNA gain. The SNR of 30.7 dB is sufficient for the succeeding blocks to measure an accurate time of arrival.

The measured signal RMS amplitude is about 300 mV when the transmitter and receiver spacing is 1 meter. According to the free space path loss equation, for the received signal amplitude to drop from 300 mV to 1 mV (49.54 dB), it takes a distance of

$$10^{49.5/20} = 300 \text{ meters.} \tag{5.4}$$

In real life, the path loss exponent is normally in the range of 2 to 5. If we assume a lossy environment with a path loss exponent value of 4, it takes a distance of

$$10^{49.5/20} \approx 17 \text{ meters.} \tag{5.5}$$

to drop to an input voltage of 1 mV. This distance is in line with our measured results.

Square Law Device

Although the baseband generated pulses occupy spectrum from DC to 1.5 GHz (-10 dB bandwidth), it is impractical to design an antenna to cover the full frequency range especially the lower end. As a matter of fact, the designed log periodic toothed antenna operates between 500 MHz to 1500 MHz. When a baseband pulse is emitted by an antenna, it practically passes through a band-pass filter and is modulated to the center of the pass band. At the receiver side, to down-convert the received signal, one of the simplest methods is to use a square law device. Employing a square law

device yields a low complexity and low power implementation, as it neither requires high sampling rates ADC nor information about the channel.

The emitted signal can be represented as

$$s\left(t\right) = p\left(t\right) \cdot \cos \omega_c t \tag{5.6}$$

where $p(t)$ is the transmitted pulse and ω_c is the center of the pass band. When $s(t)$ passes through a square law device, the output can be written as

$$r\left(t\right) = \left[s\left(t\right)\right]^2 = \left[p\left(t\right)\right]^2 \cdot \left(\cos \omega_c t\right)^2 = \frac{1}{2}\left[p\left(t\right)\right]^2 + \frac{1}{2}\left[p\left(t\right)\right]^2 \cdot \cos 2\omega_c t. \tag{5.7}$$

It is derived from above that a square law device provides a lower and an upper sideband signal. By letting $r(t)$ pass through a low-pass filter, we obtain the low frequency sideband component $\frac{1}{2}\left[p\left(t\right)\right]^2$. Hence, a square law device essentially down-converts the received signal to baseband and outputs its energy.

There are several devices that present a square law characteristic, such as a diode and a transistor. When the input signal level is small, a diode acts roughly as a square law device. However, it has limited dynamic range and worse yet, it has large conversion loss and its I-V curve varies with temperature. Temperature compensation can be applied but it complicates the circuit design [127]. Another approach is based on the square-law characteristics of MOS transistors operated in the saturation region [128]. However, it has limited operation frequency due to Miller effect [129].

A square law device can also be realized by multiplying a signal with itself, and such device is called a multiplier. A mixer cannot be used as a multiplier although it is frequently described as a multiplication device. A mixer has two input ports, one linear signal input port and one carrier input port. The carrier input contains a limiting amplifier or is driven with a sufficiently large signal (5 - 10 dBm) to turn on and off an internal switch of the mixer [130]. Therefore, fundamentally, a multiplier and a mixer work differently and they cannot replace each other.

We used ADL5391 analog multiplier to implement the squaring function by connecting both inputs to the signal to be squared. It provides 2 GHz bandwidth which is perfectly feasible for our design. In addition, a gain can be applied to the multiplied signal by adjusting the voltage on the GADJ pin. The ADL5391 has a unique design that ensures absolute XY-symmetry, i.e., identical X and Y amplitude/timing responses [131]. This feature ensures the squared signal energy being maximal. Fig. 5.10

shows the output waveform of the multiplier when the anchor Tx and Rx are placed 5 meters apart. Note that before the low pass filtering, the waveform contains both low and high side band signals.

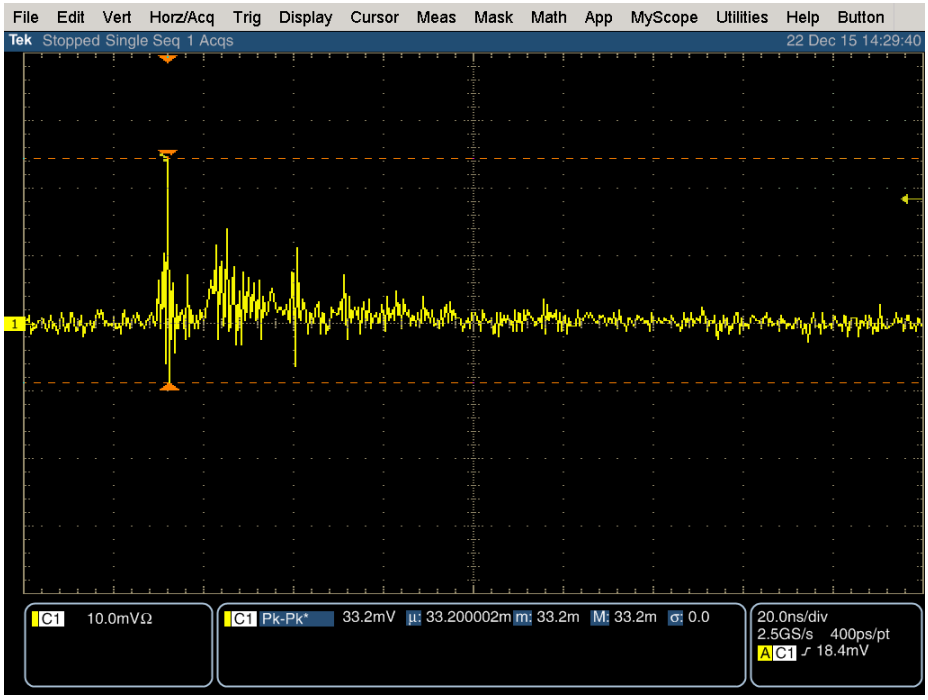

Figure 5.10: Multiplier output waveform.

Low Pass Filter

To remove the high frequency product and noise from the multiplier output, we designed a 7th order Chebychev low pass filter. Compared to popular Butterworth and Bessel filters, the primary attribute of the Chebychev filter is faster roll-off by allowing ripple in the pass-band. The Chebychev response is an optimal trade-off between ripple and roll-off. When the ripple is set to 0, the filter becomes maximally flat filter or Butterworth filter. When the ripple increases, the roll-off becomes sharper. The designed 7th order filter has approximately 0.6 dB pass-band ripple, providing approximately 200 dB/decade roll-off.

Fig. 5.11 demonstrates the simulated and measured filter S21 magnitude. The Vector Network Analyzer 8720ES has a limited capability to measure low frequency response, and therefore the blue curve starts from 50 MHz. The designed filter has a good match to simulation in the pass-band. However, it presents a narrower band-

width mainly due to the limited quality factor of the inductor. As frequency goes beyond 300 MHz, the filter response reaches a plateau of approximately -60 dB due to the capacitor's self-inductance. Above the capacitor self-resonance frequency (SRF), a capacitor acts as an inductor. Therefore at high frequencies, the L-C low pass filter effectively becomes an inductive ladder, and how many dB down at the plateau depends on ratio of the series inductor's inductance and the parallel capacitor's self-inductance. To improve the rejection at high frequency, one can choose high SRF capacitors, or alternatively, use two capacitors in parallel to replace one capacitor.

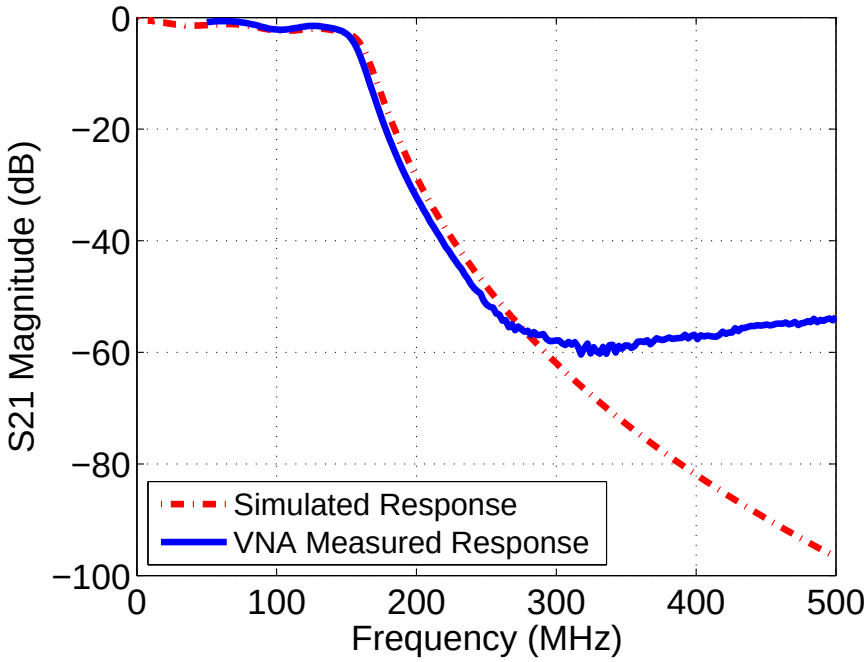

Figure 5.11: Simulated and measured LPF response.

Low pass filtering resembles an integration process. An ideal integrator has a -3 dB cut-off frequency of $\frac{\frac{2\pi}{T}}{2.24}$ [132], where T is the integration period. Given that the designed LPF has a -3 dB bandwidth of approximately 150 MHz, we can calculate an integration period of approximately 18.7 ns. An integration period of 18.7 ns typically includes the line of sight (LOS) direct path signal, as well as several multipath components. Due to the fact that the multipath components have varying amplitude, phase and time delay, the low pass filter output can differ, which causes a timing error. The detailed analysis of this kind of timing error is presented in Section 5.6.3. Fig. 5.12 demonstrates the low pass filtered waveform, and it can be observed that after low pass filtering, the high frequency side band signal is completely eliminated.

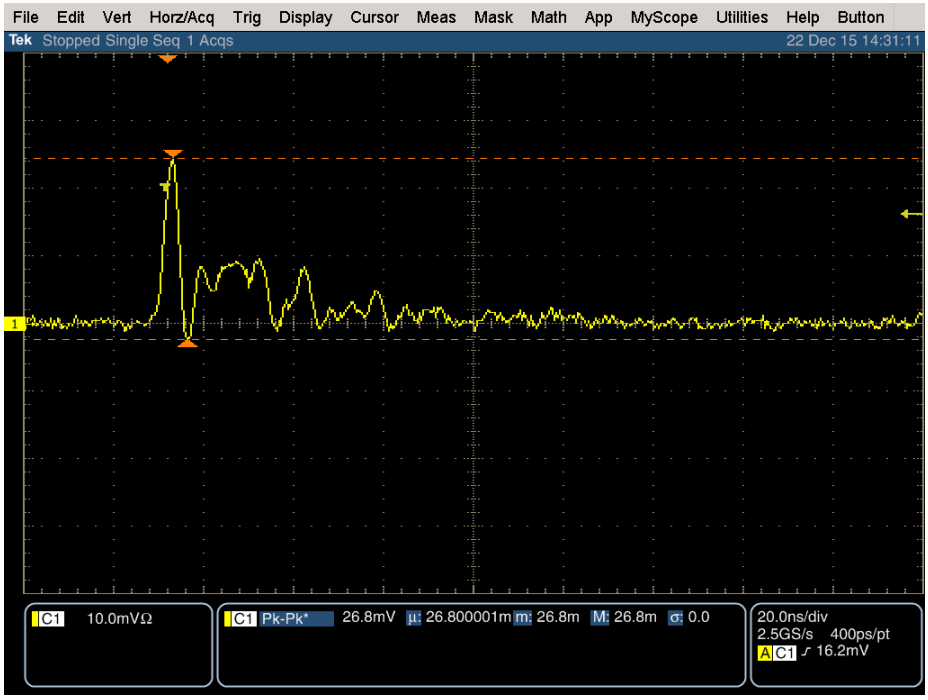

Figure 5.12: LPF output waveform.

IF Amplifier and Comparator

A two-stage intermediate frequency (IF) amplifier is employed after the LPF to increase the signal amplitude. Since there are sufficient gains at RF, the noise performance of the IF amplifiers becomes less critical. We selected ADL5535 IF gain block, which has a broadband operation frequency up to 1 GHz, and a fixed gain of about 16 dB. Two ADL5535 gain blocks are cascaded in this design to provide about 32 dB voltage gains. Fig. 5.13 demonstrates the waveform after IF amplifiers.

After the IF amplification stage, a fast comparator is employed to continuously compare the IF amplifier's output signal amplitude with a threshold voltage. The threshold voltage is set to a certain percentage of the peak value to detect the leading edge of the pulses [95]. Due to the amplitude noise on the received signal, the trigger time of the comparator can be modeled as a stochastic process with a normal distribution. The influence of this uncertainty can be minimized by performing averaging.

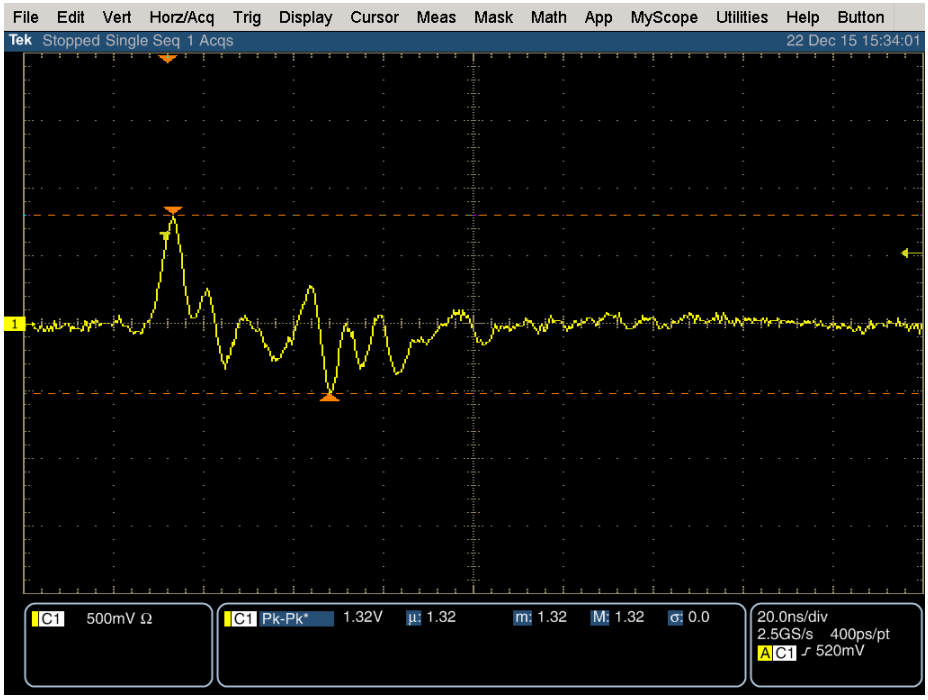

Figure 5.13: IF amplifier output waveform.

Time-to-Digital Converter

The time difference arrival measurement is performed by a time-to-digital converter (TDC) with 50 ps RMS resolution. We used a commercially available device TDC-GP2 from Acam-Messelectronic [133]. The joint use of IR-UWB technology and a TDC allows for several advantages, including the possibility of low-complexity implementation of the radio transceiver front-end and high resolution time-interval measurement [134].

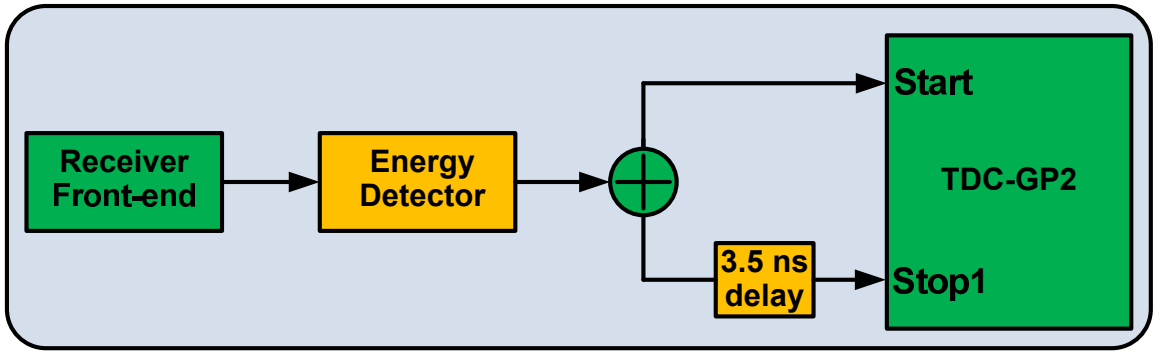

Figure 5.14: Block diagram of the TDC connection.

The block diagram of the TDC connection is shown in Fig. 5.14. The received signal passes through the front-end and the energy detector. Afterwards, it is split into two paths, with one path connecting to the TDC 'START' channel, and the other path to 'STOP 1' channel after 3.5 ns fixed delay. The 3.5 ns delay is required due to the TDC-GP2 device limitation [133]. The TDC-GP2 stop channel features a 'multi-hit' capability, i.e., it can measure up to 4 input pulses' timing consecutively. We take advantage of this feature in our design to measure the time difference between the two consecutive pulses, where the first one is from the direct path and the second one from the re-transmitted path.

Receiver Specification Summary

Table 5.1 summarizes the overall performance of the A-TDOA receiver.

Table 5.1: A-TDOA receiver specification.

Center Frequency	750 MHz
Bandwidth	500 MHz
Noise Figure	8.5 dB
RF Voltage Gain	32 dB
IF Voltage Gain	32 dB
Power Consumption	2.335 W

The implemented receiver is shown in Fig. 5.15. Low cost FR-4 material is used to fabricate a 2-layer printed circuit board (PCB). A good impedance match is critical in RF designs, as it minimizes the signal reflection. The PCB traces (microstrip) were carefully designed to present approximately 50 ohm at the frequency of operation.

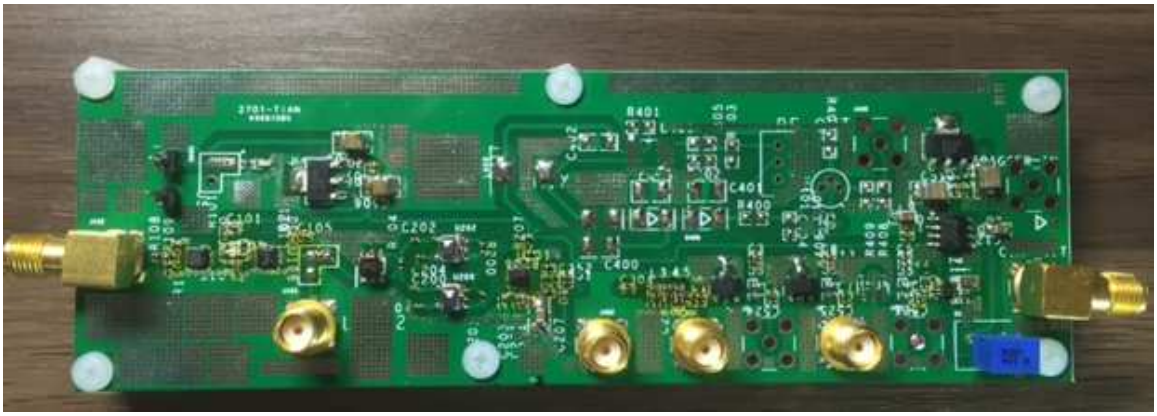

Figure 5.15: Photo of the implemented receiver.

A 2-layer PCB board design provides cost savings compared to a 4-layer PCB design and can provide comparable performance, but requires careful signal routing and component placement. These designs are generally limited to thicknesses of 0.8-1.0 mm, as using a greater thickness microstrip line causes the corresponding widths for common impedances (e.g., 50 ohms) to be too large for practical designs [135]. Given a target microstrip characteristic impedance, the trace width is inversely related to substrate thickness. To maintain a reasonable trace width, i.e., below 20 mil, we used very thin (0.4 mm) PCB in our design.

5.3.4 Target Node Implementation

One of the unique attributes of the A-TDOA system is the use of a "receive and re-transmit" method for the target node design. It acts as a radar transponder in a way that it emits a pulse in response to a received signal from the anchor Tx. The implementation is almost purely in analog domain, offering several benefits:

- It is clock-free, therefore avoids clock jitter and drifting.
- It avoids long processing delays due to bit synchronization and channel estimation [3].
- Its group delay can be calibrated and stored in memory, and retrieved when conducting position estimation.

Despite the benefit it brings, the target node design is the most challenging part of the A-TODA system implementation. Several architectures, namely reflection, amplify and forward, as well as receive and re-transmit architectures were built and tested. This section describes two failure cases and finally a successful design.

Failure analysis 1 — reflection architecture

A first attempt to use a simple reflector failed. The reflector simply consists of an antenna and an open-ended transmission line. If the end of a transmission line is not loaded with an impedance that is complex conjugate to the characteristic impedance of the transmission line, signal reflection occurs. In extreme case where a transmission line is open-ended, the entire signal will be reflected back. In RF designs, such scenarios are to be avoided but we deliberately made it happen such that an incoming pulse can be reflected to the receiver.

Unfortunately, this simple approach did not work because the reflected signal is severely attenuated. Two major factors contribute to the attenuation, one is the insufficient return loss of the antenna, and the other is the insertion loss of the transmission line. Due to the attenuation, the receiver can barely detect the reflected signal. To overcome the difficulty, a high speed ADC can be employed to repeatedly capture the incoming signal and apply time average or other digital signal processing techniques to improve SNR, yet a high speed ADC is expensive and power hungry.

Failure analysis 2 — amplify and forward architecture

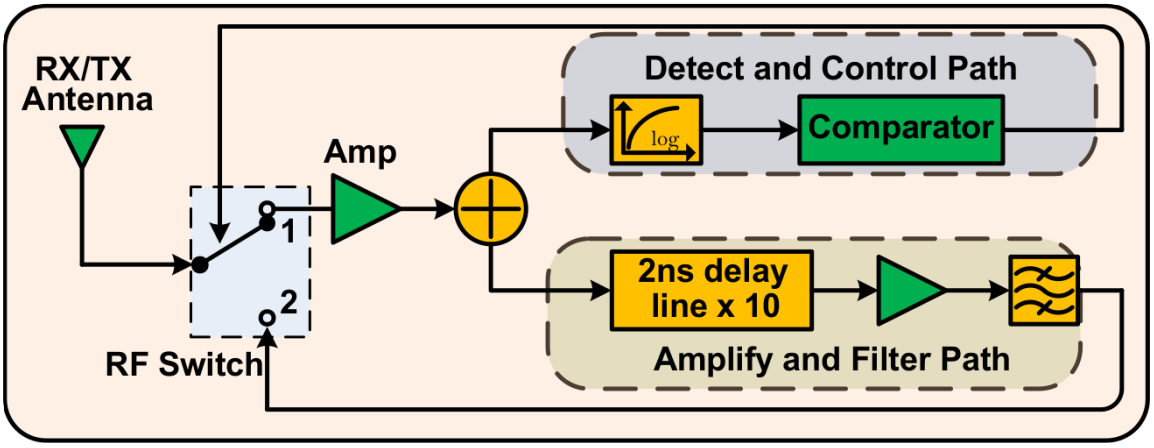

Figure 5.16: Amplify and forward architecture.

A second attempt of an "amplify and forward" architecture also failed. The block diagram of the implementation is shown in Fig. 5.16. By default, the RF switch is at position "1". When an incoming signal is received, it is amplified by an RF LNA and then fed into a splitter. After the splitter, there are two signal paths: "Detect and Control Path", and "Amplify and Filter Path". For the "Detect and Control Path", the signal first enters a logarithmic detector, which is capable of converting a RF pulse to a corresponding voltage output. The detector output compares with a pre-defined voltage threshold to generate a digital LVTTL logic signal which controls the RF switch's pole position. For the "Amplify and Filter Path", the signal first flows into 10 delay line ICs, each of which provides 2 ns of wideband delay. After the delay lines, another amplifier is employed to compensate for the delay line insertion loss. The amplified signal is then filtered by a lumped element bandpass filter and then fed back to the RF switch pole position "2". The prototype photo is shown in Fig. 5.17.

Figure 5.17: Photo of the amplify and forward implementation.

Meeting the timing constraint is absolutely critical for the success of this architecture. When a pulse arrives, it is detected by the logarithmic detector and drives the comparator to change the RF switch to position "2". In the meantime, the incoming pulse is delayed, amplified and filtered and by the time it reaches the RF switch, the pole position must be set to "2" for the signal to be re-transmitted by the antenna. In addition, during re-transmission, the RF switch must remain at position "2" for several nano-seconds before it is set back to "1" by the "Detect and Control Path".

This method fails due to the fact that it is difficult to meet the timing constraint reliably. Fig. 5.18 illustrates the timing at different nodes along the signal chain. As can be seen, the time when the RF switch changes state is solely dependent on the detector output and the comparator threshold. It must time align with the 20 ns delay properly for the amplified and filtered signal to be re-transmitted.

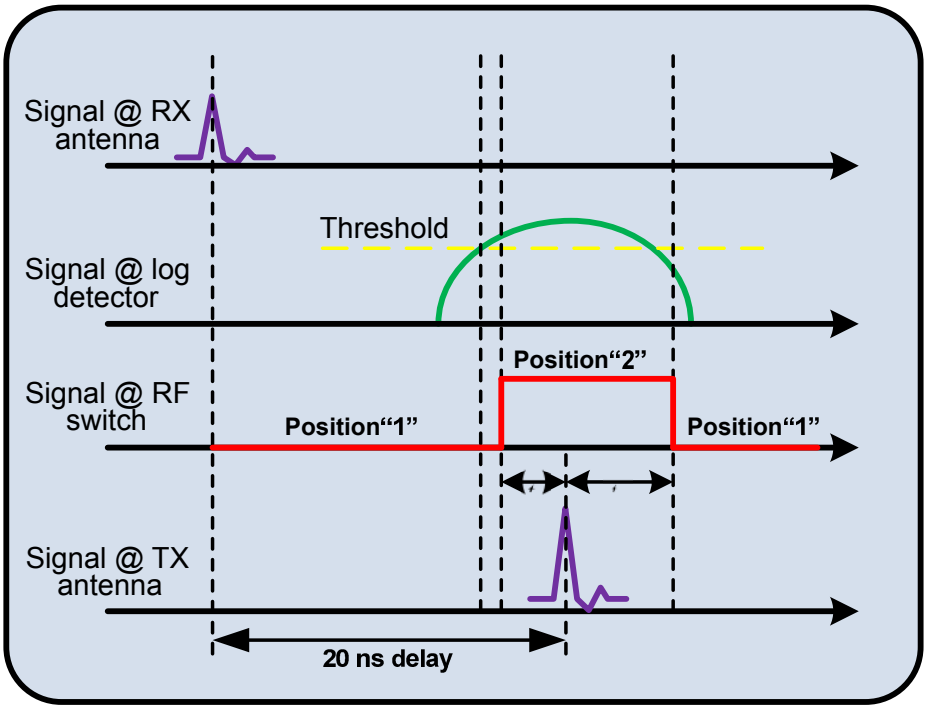

Figure 5.18: Timing diagram of the amplify and forward architecture.

Success Design

Winston Churchill once said: *“Success is the ability to go from a failure to another with no loss of enthusiasm”*. The two failures eventually lead to a successful design.

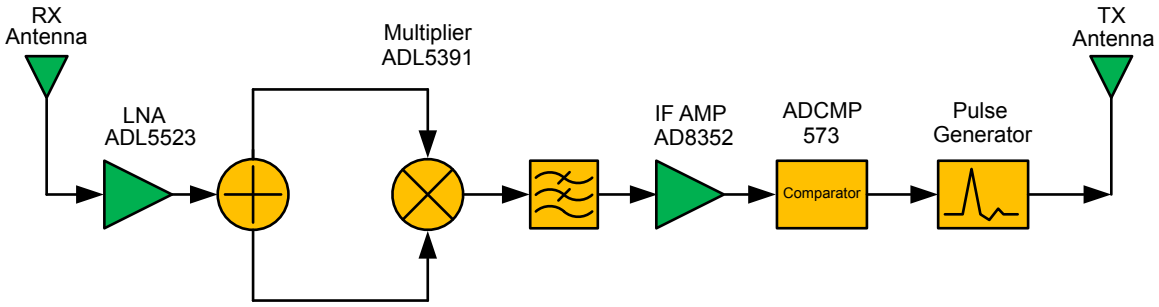

Figure 5.19: Target node architecture.

Fig. 5.19 shows the block diagram of the target node. It re-uses the receiver energy detector design to trigger a pulse generator to emit a pulse to the anchor Rx. The details of the energy detector are presented in the Section 5.3.3, and will not be reiterated here. The reflector also re-uses the transmitter design except some circuit modification to generate a pulse upon receiving a trigger signal.

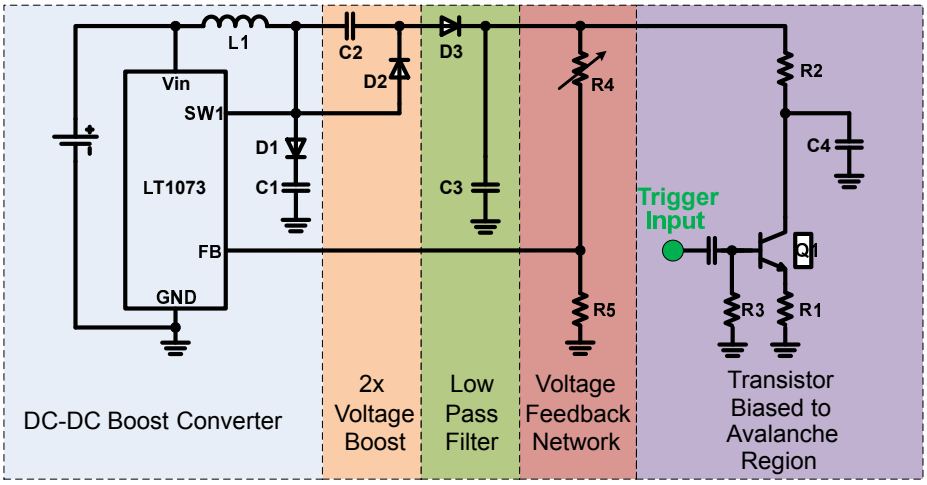

Figure 5.20: Triggered pulse generator schematic in target node.

The modified pulse generator circuit is shown in Fig. 5.20. Two major changes are R4 and Q1. Resistor R4 is replaced with a potentiometer, and Q1's base is connected to a trigger input. The high voltage bias on Q1's collector can be adjusted by R4, and it is set at the point where free running pulses across R1 just disappear. This puts Q1 slightly below its avalanche point. When an input trigger pulse is applied, Q1 avalanches. The result is a quickly rising, very fast pulse across R1. Then capacitor C4 discharges, Q1's collector voltage falls and avalanche breakdown ceases. The capacitor C4 then recharges to just below the avalanche point. At the next trigger pulse this action repeats.

One of the reasons to choose Avalanche pulse generator is that it can be configured to have a fixed pulse repetition time T_r regardless if a trigger signal is present or not. This feature is critical in avoiding the self-resonance issue, i.e., the re-transmitted signal is picked up by the same device and trigger another re-transmission.

5.3.5 Antenna

The antenna, which is of great importance in the communication channel, determines the signal quantity of the electronic output stage, operating frequency band, power level and it will also dominate the occupied area of the communication system. There are more challenges in designing an UWB antenna than a narrow band one, mainly due to the requirement of satisfying radiation properties over a wide bandwidth and maintaining a good impulse response in time domain.

The sub-GHz UWB technology has unique advantages in localization applications

thanks to its first arrival detection potential and better material penetration capability [136]. For instance, reported in [136], the attenuation to penetrate a 5.8 cm brick wall is 2.06 dB at 1 GHz, but 5.27 dB at 4 GHz. Nevertheless, for sub-GHz UWB applications, antenna design is even more challenging. Mark J. in [136] suggests use large current radiator (LCR) and electric dipole antenna. The LCR was first introduced by Harmuth and it has the advantage of preserving pulse shape and low frequency variation over wide bandwidth. However, the principal disadvantage is that they tend to be inefficient, as absorptive coating is typically used to dissipate undesired emissions [137]. To overcome the low efficiency issue, researches modified the original LCR design to devise a monoloop antenna [138]. It is more efficient but it does not have stable and consistent pattern as a function of frequency. Besides aforementioned disadvantages, LCR antennas have a 3-D structure and are difficult to manufacture. Particularly, they cannot be fabricated on a PCB. Dipole antennas are widely used in UWB applications at high frequency band [139, 140], but they are not readily applicable for sub-GHz applications due to the bandwidth limitation and physical size being too large. A dipole antenna typically has a physical size tightly related to $\lambda/2$, where λ is the wavelength of the center frequency. For instance, 500 MHz operation frequency requires a physical size close to 30 cm.

There are very few sub-GHz UWB antenna designs presented in the literature. In [141], a log-periodic antenna is presented to operate in a very wide bandwidth of 300 to 1100 MHz, yet the physical size is rather large, i.e., 398 mm by 420 mm, which is too bulky and therefore not practical. A compact UWB array antenna featuring an available bandwidth of 325 to 1000 MHz is presented in [142]. A single antenna element has a relatively small size (102 mm by 102 mm) on a significantly high contrast ceramic substrate ($\epsilon_r = 98$ compared to $\epsilon_r = 4.2$ of a FR4 substrate). The disadvantage is that such substrate is extremely costly and is expensive in mass production. A low profile discone antenna was proposed by Chen et al. to cover a bandwidth of 430 MHz to 845 MHz [143]. In spite of a reduction in height, the antenna is still too large for a portable localization system.

We designed a log-periodic toothed trapezoidal antenna for the A-TDOA system thanks to the broad bandwidth it possesses. It has an important characteristic that its pattern and impedance are independent of frequency over theoretically unlimited bandwidth [144]. Trapezoidal toothed log-periodic antenna is a modified version of logarithmic spiral antenna [145]. This modification makes the construction easy. In addition, it can be easily manufactured on a PCB, which is a highly desirable feature

for the portable A-TDOA system.

One major drawback of log-periodic antenna is ringing effect and correspondingly time domain distortions. Fig. 5.21 demonstrates the characterization of the designed antenna's time domain transient response. It was measured with a Tx-Rx distance of 1 meter. Ringing effect, caused by resonances due to energy storage or multiple reflections in the antenna, can be observed. It results in oscillations of the radiated pulse after the main peak. Ringing effect is undesirable for high data rates communication as it expands the duration of a transmitted pulse. Also, it causes distortion which impacts high resolution radar applications. However, the A-TDOA receiver architecture is based on energy detection which is able to absorb the whole duration of the ringing energy. Besides, the pulse shape distortion is perfectly tolerable with an energy detector.

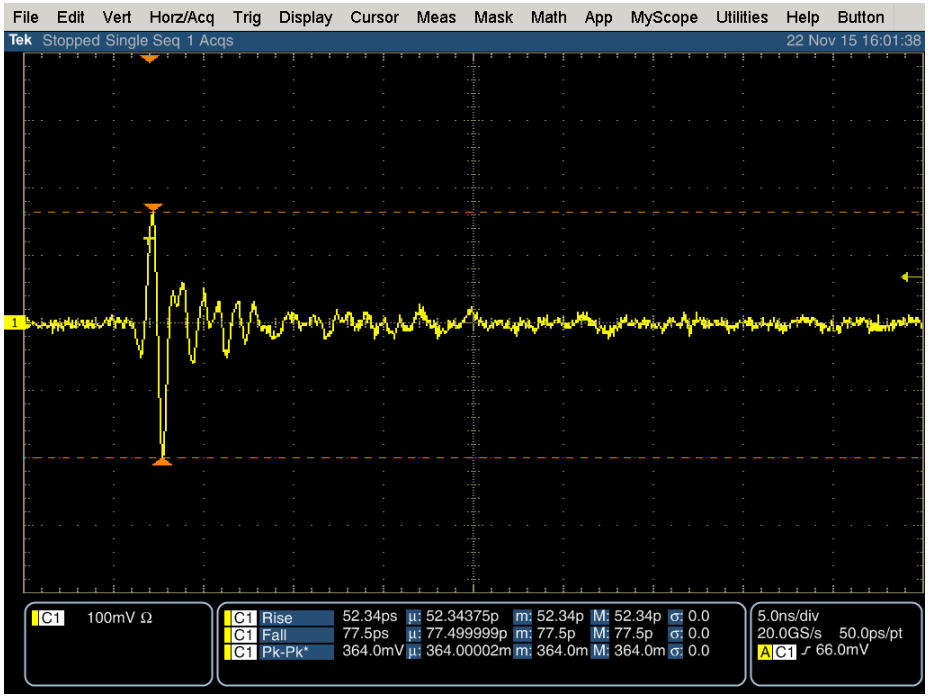

Figure 5.21: Time domain waveform of the designed antenna.

The designed antenna achieves moderately good performance over the frequency of interest. Typically a -10 dB return loss is used as a bench mark for good antenna design. Small size and reasonably good return loss can be achieved relatively easily for antennas operating at high frequencies. However, it is particularly challenging for sub-GHz antennas. The antenna size, bandwidth and radiation efficiency are interrelated, and there is no complete freedom to independently optimize each one. It needs to be

emphasized that compactness and lightweight requirements are the driving factors for the antenna design in the A-TDOA localization system. Therefore, we make trade-off between return loss and antenna size due to the frequency operation being in the hundreds of MHz range where antenna size tends to be large. Instead of trying to achieve -10 dB return loss where 10 percent of the power is reflected, we aim for -6 dB return loss where 25 percent of the power is reflected.

Due to its self-complementary structure, the designed antenna possesses an invariant input impedance of

$$Z_{in} = \frac{Z_{F0}}{2} = 60\pi \ \Omega = 188.5 \ \Omega, \tag{5.8}$$

where Z_{F0} is the free-space impedance [146]. We used a mini-circuit TCM4-14+ RF transformer to convert the differential impedance to single-ended 47 ohm, which is close enough to the receiver input impedance of 50 ohm. The TCM4-14+ operates between 200 to 1400 MHz, and has a conversion ratio of 4.

The antenna is designed with the HFSS simulation tool, and is fabricated on a 2 mm thickness FR-4 epoxy substrate, with a dielectric constant $\epsilon_r = 4.2$ and a loss tangent $\tan\delta = 0.02$. It has a dimension of 14 cm by 11 cm. Being lightweight and compact, the antenna is very easy to be deployed. Photograph of the manufactured antenna is shown in Fig. 5.22. Measurements were carried out using an Agilent 8720ES S-parameter network analyzer. The measured and simulated S-11 results are shown in Fig. 5.23.

5.4 System Performance

We conducted extensive measurements to evaluate the performance of the A-TDOA localization system. In this section, we first present test results using wired connection for the purpose of group delay calibration and functionality validation. Then the two-dimensional localization accuracy is studied in outdoor and indoor radio environment.

5.4.1 Wired Connection Ranging Measurement

We first evaluated the ranging performance of the A-TDOA system using fixed length cables connecting the anchor Tx, anchor Rx and target node. The goal of this test is twofold: (1) it validates the system functionality under ideal condition, i.e., no

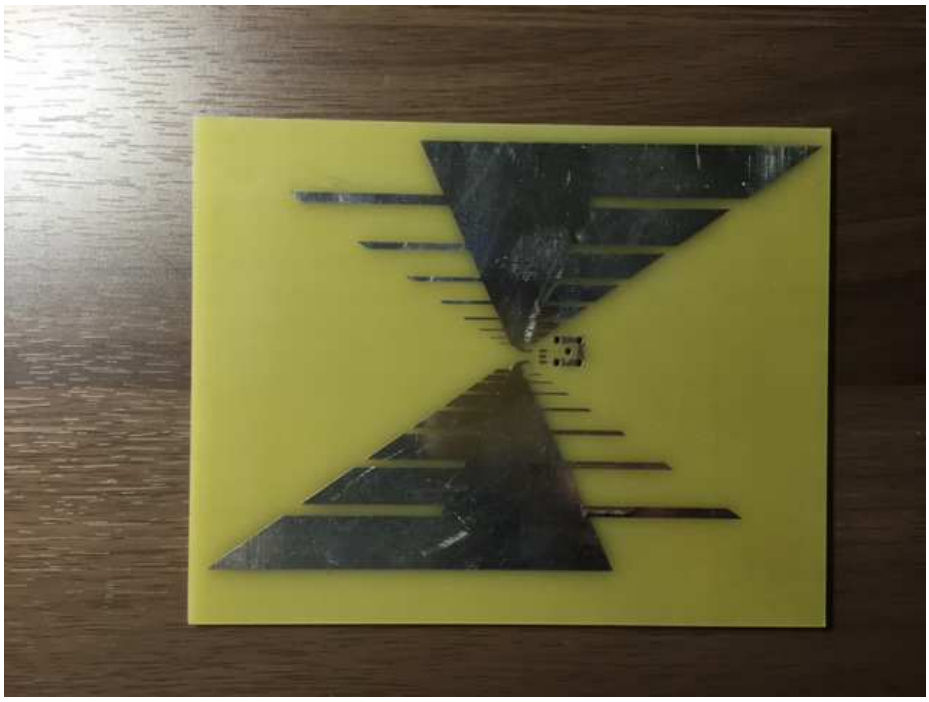

Figure 5.22: Manufactured antenna.

multipath fading, no antenna distortion and attenuation, and no path loss; (2) using wired connection allows us to precisely measure the target node's group delay, which will be calibrated out in position estimation.

The test setup is shown in Fig. 5.24. The anchor Tx, anchor Rx and target node are interconnected with SMA cables. To prevent signal saturation, variable attenuators are connected to the output of the anchor Tx and the target node. The group delay of SMA cables as well as the attenuators are precisely calibrated using a vector network analyzer, so that they can be subtracted to derive the true target node's group delay. Fig. 5.25 shows an example of the comparator output of anchor Rx.

The target node's group delay can be derived from the measured time difference of the two pulses and the pre-calibrated SMA cable group delays. Results show the target node's group delay is 21.3 ns with 300 measurements. Fig. 5.26 shows the distribution of the measured group delay. The histogram of the measured data is compared to the probability function of a Gaussian distribution (red trace). It can be observed that the measured distribution agrees relatively well with a Gaussian distribution. The target node's group delay will be deducted in the TDOA measurements.

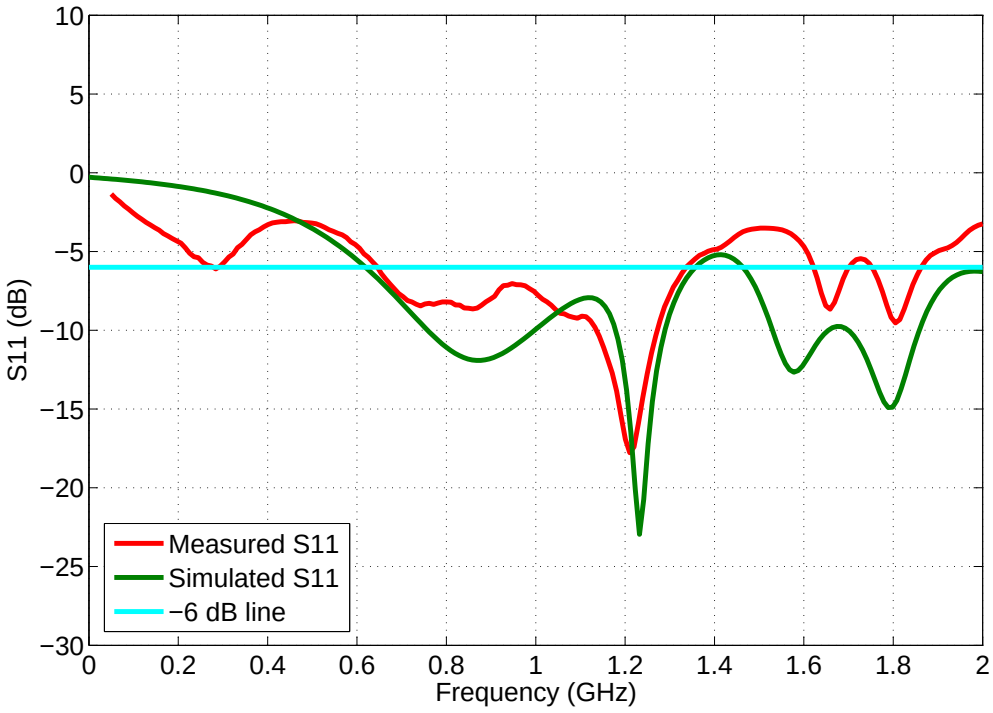

Figure 5.23: Measured and simulated antenna S11 parameter.

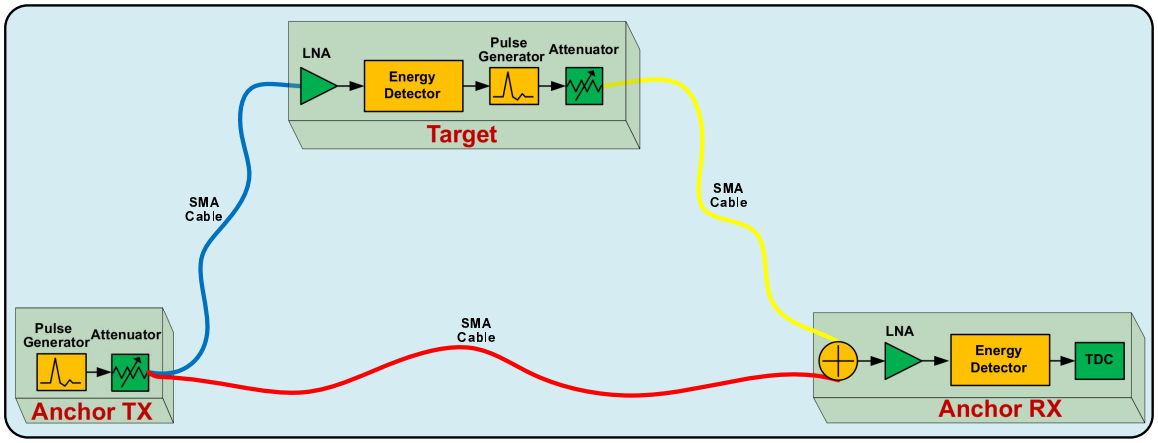

Figure 5.24: Wired connection measurement setup.

5.4.2 Outdoor Localization Measurement

We conducted localization measurement in an outdoor environment which is a typical residential area. The test environment is surrounded by houses, fences, trees, etc, and therefore the radio channel contains several significant multipath components. The

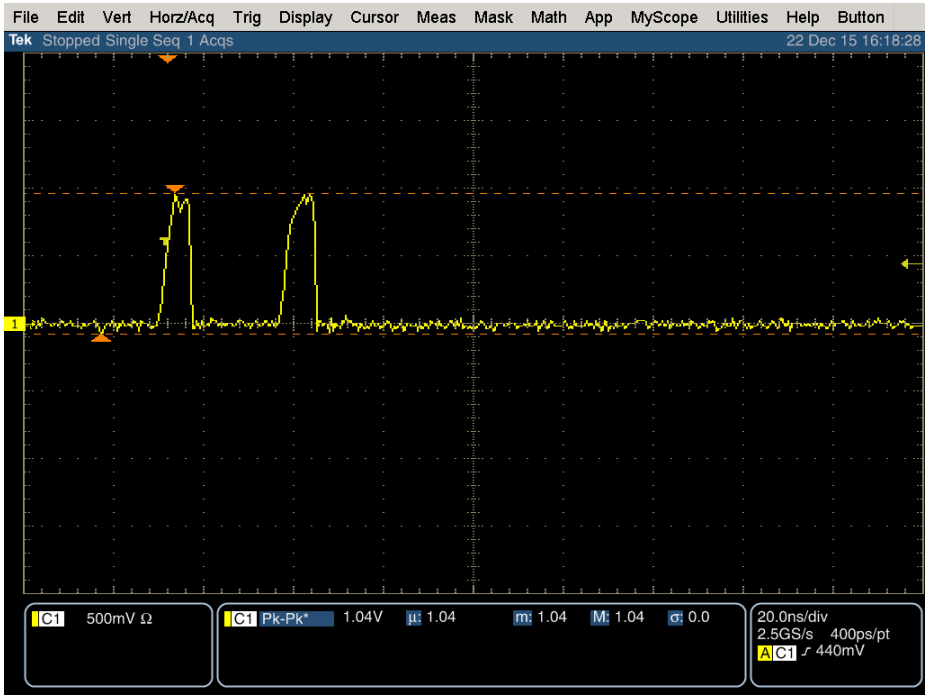

Figure 5.25: Anchor Rx output waveform.

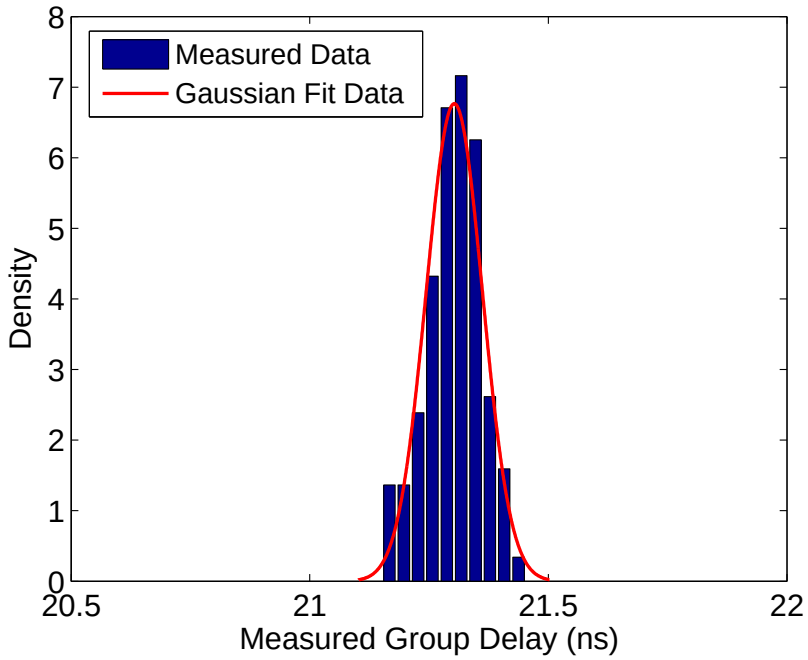

Figure 5.26: Distribution of the measured group delay.

localization system described in this section is based on the deployment layout shown in Fig. 5.27. Four anchor nodes constitute a square area of 8 m by 8 m, inside which the target node is placed at 16 locations. The experiments are performed while keeping the antennas in stationary positions, at the same height of about 1 m from the floor and in line-of-sight conditions.

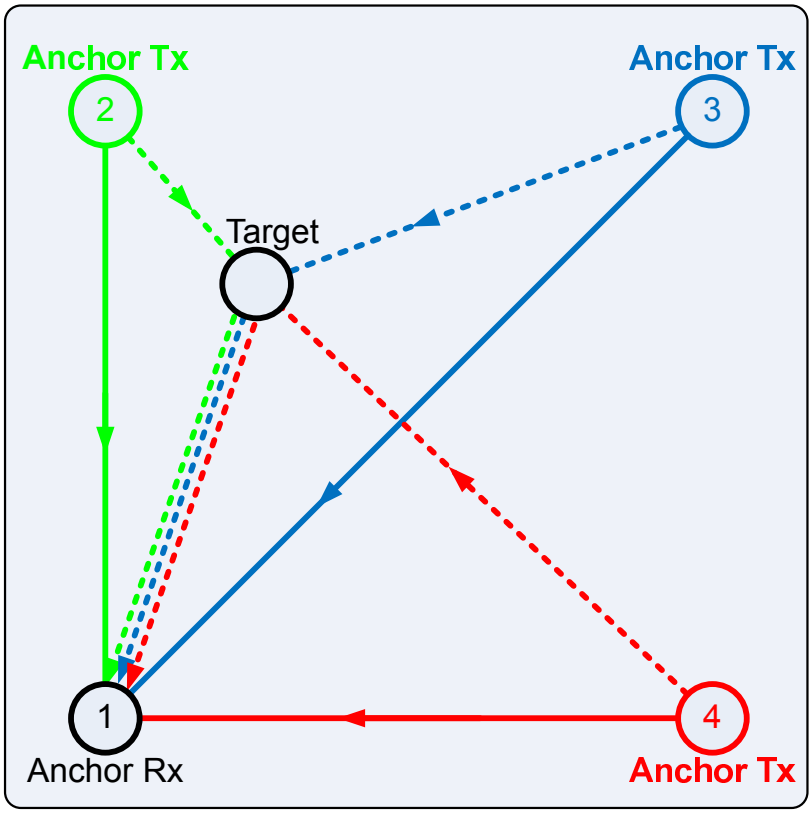

Figure 5.27: A-TDOA system deployment.

Fig. 5.28 shows the ranging error distribution obtained in the outdoor localization measurement. The distribution of the measurements has 50 percent within 7.4 cm and 90 percent within 14 cm. The distribution does not tightly follow a Gaussian distribution mainly due to that ranging errors are affected significantly by the radio propagation channel. A detailed analysis can be found in Section 5.6.3.

The measured localization accuracy is demonstrated in Fig. 5.29. Locations of the target nodes are estimated using the two-step algorithm described in Section 4.3. The red plus signs represent the target node's true positions, and the blue dots represent the measured positions. In addition, the square root of the MSE is shown right below each red plus sign. For each position, 50 measurements have been performed.

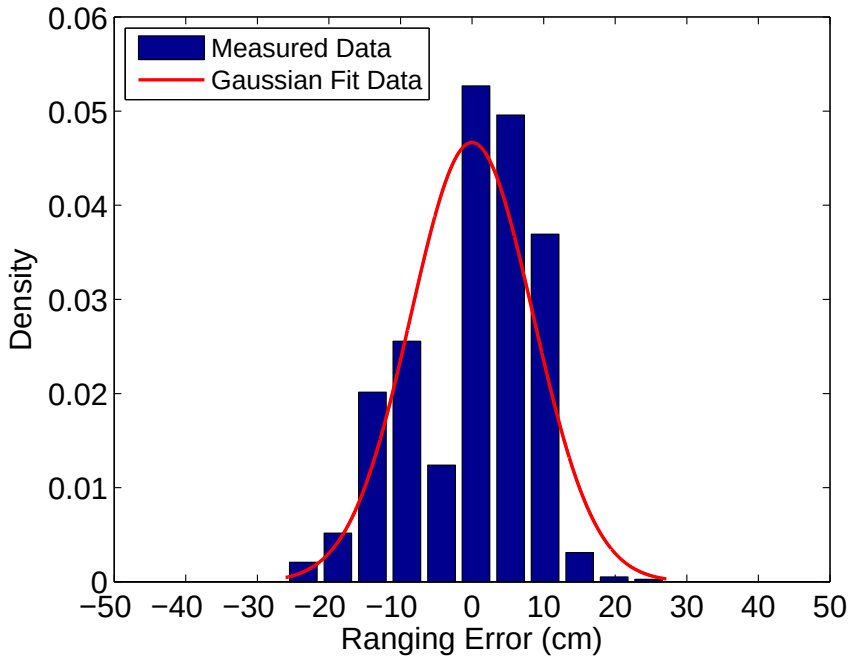

Figure 5.28: Distribution of the ranging error in an outdoor environment.

Experimental data show that good matching between true and estimated positions has been achieved with a worst case estimation error of 20.7 cm.

5.4.3 Indoor Localization Measurement

Localization in an indoor environment is a challenging task because of the harsh radio propagation conditions. The indoor radio channel is heavily site-specific and can vary significantly depending on the surrounding objects, interference sources, the mobility of people and other dynamic factors. There are various obstacles, for example, walls, equipment, human beings, influencing the propagation of electromagnetic waves, which lead to multipath effects.

We conducted extensive measurements in an indoor LOS radio condition. The measurements were carried out in a laboratory, which is a typical indoor environment that is rich in reflective and diffractive objects, as well as interference from other commonly used electronic and radio systems. Similarly, the system deployment is based on the layout shown in Fig. 5.27. Four anchor nodes constitute a square area of 6 m by 6 m, inside which the target node is placed at 9 locations.

Fig. 5.30 demonstrates the distribution of the measured ranging error in an indoor

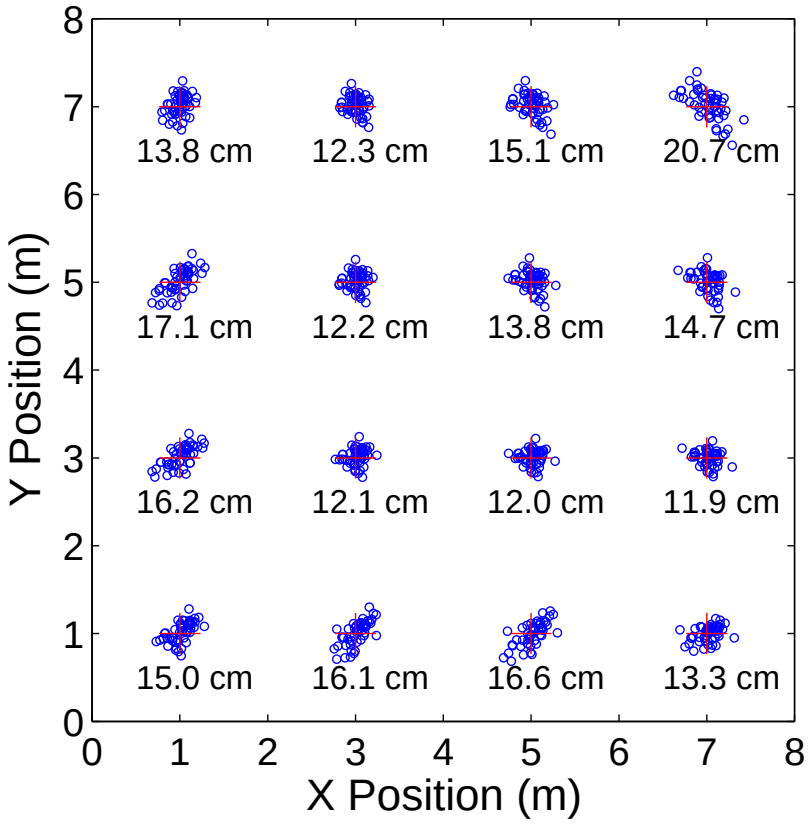

Figure 5.29: Measured localization accuracy in an outdoor environment.

environment. Results show that the ranging error is less than 4.7 cm with 50 percent, and less than 9.6 cm with 90 percent. Compared to the outdoor case, the measured data matches a Gaussian distribution more closely. It is owing to the fact that the indoor space is constrained and therefore significant multipath components arrive in the same cluster. In an outdoor environment though, some multipath components may arrive at the receiver approximately the same time as the signal from the re-transmitted path, causing a ranging bias. This scenario is studied in Section 5.6.3.

The measured localization accuracy in the indoor environment is shown in Fig. 5.31. The measured MSE is less compared to the measured MSE in the outdoor environment, due to that the experiment area is smaller and the significant multipath components arrive in the same cluster. It is obvious that the estimated position error at the upper right corner is greater than other locations. That is because the re-transmitted path travels a longer distance and therefore the SNR is lower.

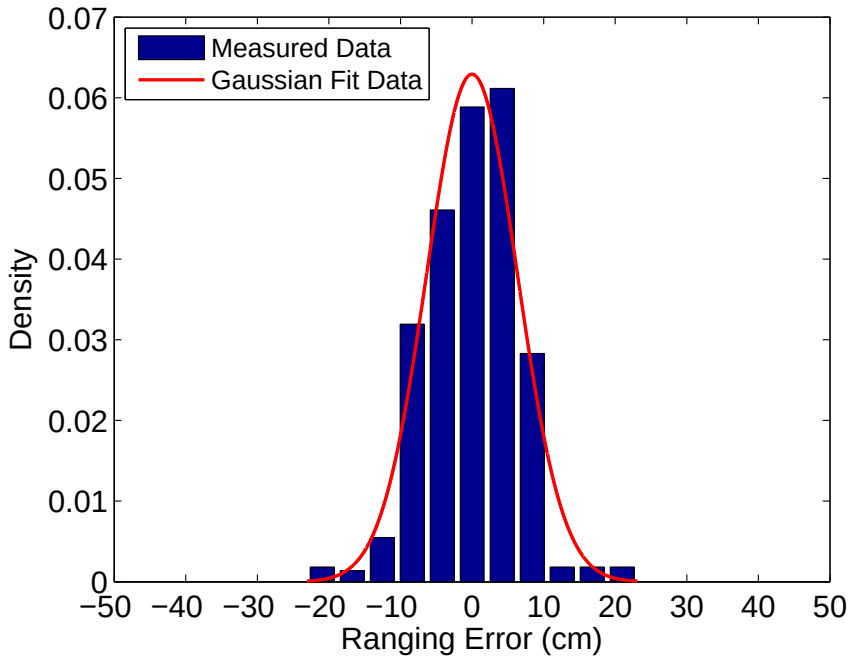

Figure 5.30: Distribution of the ranging error in an indoor environment.

5.5 Comparison to Existing Systems

In this section, we compare our results with some of those previously reported. The results of the experiments performed with indoor and outdoor UWB localization systems that were published in the recent years, are summarized in Table. 5.2. When interpreting the results, one should take into consideration that neither the radio parameters nor the environmental conditions were the same.

Table 5.2 summarizes the following information to make a high level comparison. Column 2 reports the time based ranging technology; column 3 gives a brief summary of the prototype architecture; column 4 presents an estimated cost; column 5 describes the measurements area which is a good indication of the system sensitivity; and column 6 summarizes the achieved accuracy. The entries in the table are sorted according to the system integration complexity. For instance, systems using lab instruments are presented firstly in the table, and systems using discrete components are presented lastly.

Compared to existing platforms, the implemented A-TDOA platform is completely built from scratch using discrete components. The anchor Tx, anchor Rx, target, as well as the antenna, have gone through extensive modification and optimization to

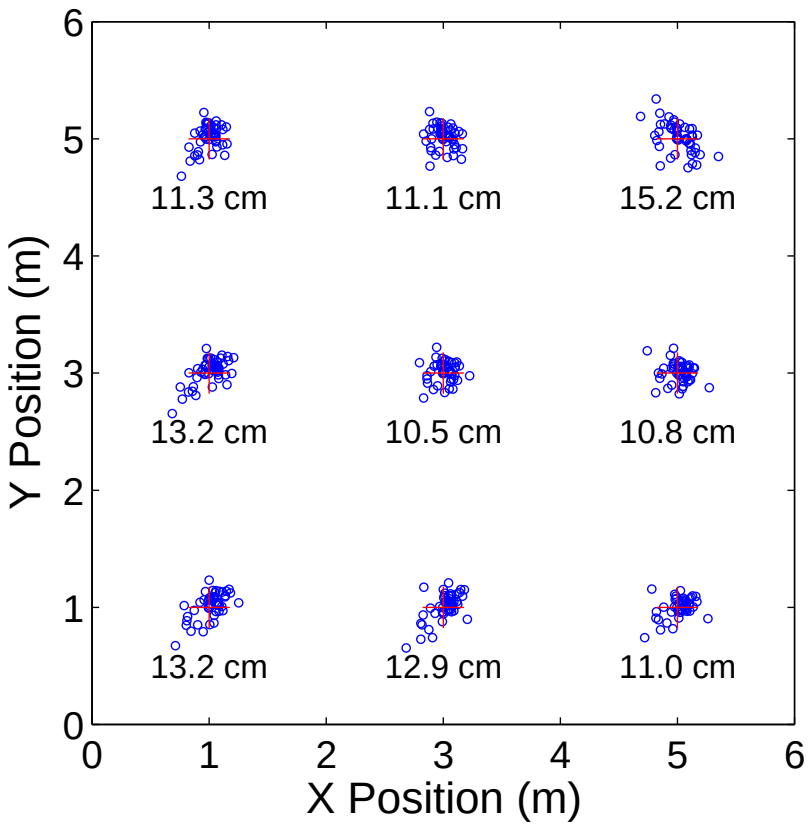

Figure 5.31: Measured localization accuracy in an indoor environment.

become more stable and reliable. Despite the low cost and low power consumption architecture, the achieved accuracy is relatively high.

5.6 Error Source Analysis

Conducting measurements in different radio conditions has revealed a number of error sources, some from non-ideal behavior of the system, and some from the environment. It is important to understand the diverse set of errors that can degrade ranging accuracy. Four sources, namely, thermal noise, unleveled detection threshold, varying propagation conditions and clock jitter, are identified and discussed along with test results to reveal the magnitude of the errors introduced in the proposed system.

Table 5.2: Comparison to the existing platforms.

Ref	Technique	Architecture	Cost	Test Area (m^2)	Accuracy (cm)
[106]	TDOA	Commercial product from Ubisense	Medium	3×3	13 – 23
[107]	TDOA	Tx: Pulse Generator Rx: Oscilloscope	High	4×9	10
[108]	TDOA	Tx: Pulse Generator Rx: Oscilloscope	High	15×15	LOS: 8.1 NLOS: 10.8
[109]	TOA	Tx: Synchronous Pulse Generator Rx: Oscilloscope	High	1.8×2.4	7.4
[110]	Two-way	802.15.4a compliant UWB RFIC	Low	5.3×11.5	5
[111]	Two-way	802.15.4a compliant UWB RFIC	Low	4.8×7.2	10
[112]	TDOA	Tx: Pulse Generator Rx: RF sampling ADC	High	8×6	30
[113]	TDOA	Tx: Pulse Generator Rx: Energy Detector and 2 GSPS ADC	Medium	6×6	10
[117]	Two-way	WLAN RFIC	Low	15×15	50
[116]	TOA	Frequency modulated continuous wave (FMCP)	Low		20
[114]	TDOA	Tx: Pulse Generator Rx: Energy Detector	Low	4×2	11.8
[115]	Two-way	Tx: Pulse Generator Rx: Energy Detector	Low	10×10	29
[96]	Two-way	Tx: Pulse Generator and Upconverter Rx: Downconverter and Energy Detector	Low	1×2	5.3
[83]	TDOA	Tx: Pulse Generator and Upconverter Rx: Downconverter and Subsampling ADC	Medium	2×7	10
This work	A-TDOA	Tx: Pulse Generator Target: Receiver and Retransmit Rx: Energy Detector	Low	8×8 6×6	20.7 15.2

5.6.1 Thermal noise

Thermal noise is identified as one of the main contributors to the overall timing error. It causes a time variation of a threshold crossing from its ideal position in time. Thermal noise is generated as a result of thermal agitation of the charge carriers which are typically electrons within an electrical conductor. It appears regardless of the quality of component used, and is dependent only upon the temperature and the value of the resistance.

The effect of broadband noise on timing jitter becomes significant as the operating bandwidth of the system is in the multiple hundreds of MHz range. The following calculations illustrate the root mean square (RMS) noise level of the A-TDOA system.

Noise at LNA Input

According to the Nyquist law, the mean-square voltage due to random thermal processes is

$$v_n = \sqrt{4kTBR}, \tag{5.9}$$

where $k = 1.38e^{-23}$ J/K is the Boltzmann's constant, T is temperature in degrees Kelvin, B is the bandwidth in Hz, and R is the resistance in ohm. At a temperature of 290 K and with an antenna load impedance of 50 ohm, the RMS noise level is $0.9\text{nV}/\sqrt{\text{Hz}}$. Due to that the LNA input impedance is matched to 50 ohm, the noise voltage applied to the LNA input is $0.45\text{nV}/\sqrt{\text{Hz}}$, and therefore, the noise power density is

$$10 \cdot \log_{10}\left(\frac{\left(0.45e^{-9}\right)^2}{50} \cdot 1000\right) = -174 \text{ dBm/Hz}. \tag{5.10}$$

Noise at LNA Output

As described earlier, we used a cascade of two ADL5523 LNA for the RF front-end amplification. Each LNA has a noise figure of 0.8 dB and a voltage gain of 21.5 dB. Due to the fact that a lossy resistive matching is used to accommodate a wide bandwidth, the noise figure of each LNA is

$$NF_{RFAMP} = NF_{LNA} + IL_{matching} \tag{5.11}$$

where NF_{LNA} is the LNA inherent noise figure, and $IL_{matching}$ is the resistive matching loss. For ADL5523, the NF_{LNA} is 0.8 dB, and $IL_{matching}$ is 5.5 dB, and therefore,

the total NF for each LNA is 6.3 dB. The cascaded NF can be calculated as

$$NF = 10 \cdot \log_{10}(F) \tag{5.12}$$

where F is the noise factor and it can be calculated with the Friis' formula:

$$F = F_1 + \frac{F_2 - 1}{G_1} + \frac{F_3 - 1}{G_1 G_2} + \ldots + \frac{F_n - 1}{G_1 G_2 G_3 \ldots G_{n-1}} \tag{5.13}$$

where F_n is the noise factor of the n_{th} device and G_n is the voltage gain (linear, not in dB) of the n_{th} device. The first amplifier in a chain has the most significant effect on the total noise figure than any other amplifiers in the chain. According to this equation, the cascaded LNA has a NF of 6.4 dB and a gain of 32 dB, and this corresponds to a noise density level of

$$-174 + 32 + 6.4 = -135.6 \text{ dBm/Hz}. \tag{5.14}$$

Noise at Multiplier Output

The multiplier ADL5391 specifies an output noise density level of -133 dBm/Hz. The combination of the LNA noise and multiplier noise is then calculated as:

$$10 \cdot \log_{10}\left(10^{-\frac{135.6}{10}} + 10^{-\frac{133}{10}}\right) = -131.1 \text{ dBm/Hz}. \tag{5.15}$$

The corresponding noise voltage spectral density is:

$$\left(10^{-\frac{131.1}{10}} \div 1000 \times 50\right)^{1/2} = 62.3 \text{ nV}/\sqrt{\text{Hz}}. \tag{5.16}$$

Noise at IF Amplifier Output

The IF amplifier ADL5535 has an NF of 3.2 dB and a voltage gain of 16 dB. The 3.2 dB NF has an input referred noise voltage spectral density of

$$\left(10^{\frac{3.2}{10}} - 1\right) \times 0.45 = 0.49 \text{ nV}/\sqrt{\text{Hz}} \tag{5.17}$$

which compares to the output noise density of the multiplier, is negligible. Therefore, for the sake of simplicity, we can ignore the noise contribution from the IF amplifier stage. Since we have two IF amplifiers cascaded with a total gain of 32 dB, the output

noise density of the IF amplifier is:

$$-131.2 + 32 = -99.1 \text{ dBm/Hz}. \tag{5.18}$$

Noise at LPF Output

The low pass filter has a bandwidth of about 150 MHz, and therefore, the total noise power is:

$$-99.1 + 10\log_{10}150e^6 = -17.3 \text{ dBm}, \tag{5.19}$$

which in terms of noise RMS voltage, is

$$\left(10^{-\frac{17.3}{10}} \div 1000 \times 50\right)^{1/2} = 31 \text{ mV}. \tag{5.20}$$

Now we have the RMS noise level present at the comparator input along with the desired signal. The next step is to calculate how much time offset caused by the thermal noise.

The thermal noise signal can be denoted as $v_n(t)$, which has a Gaussian distribution of zero mean. The probability distribution $f(v_n)$ can be written as

$$f\left(v_n\right) = \frac{1}{\sqrt{2\pi v_{nRMS}^2}} e^{-\frac{v_n^2}{2v_{nRMS}^2}}, \tag{5.21}$$

where v_{nRMS} is the RMS noise voltage.

We employed a high speed comparator to compare the input signal voltage to a predefined threshold that is set by a high accuracy voltage reference. The input signal can be written as

$$y(t) = s(t) + v_n(t), \tag{5.22}$$

where $s(t)$ is the desired signal. As depicted in Fig. 5.32, at a time offset Δt from the ideal threshold crossing time instant t_0, there is a probability that the noise signal $v_n(t_0 - \Delta t)$ superimposed onto $s(t_0 - \Delta t)$ to cause $y(t_0 - \Delta t)$ to reach the threshold. Thus it causes a jitter of Δt that is sooner or later than the anticipated ideal threshold crossing point.

We define the desired signal slew rate as S when it is sufficiently close to the threshold crossing voltage, and hence, the noise voltage can be represented as

$$v_n = S \cdot \Delta t. \tag{5.23}$$

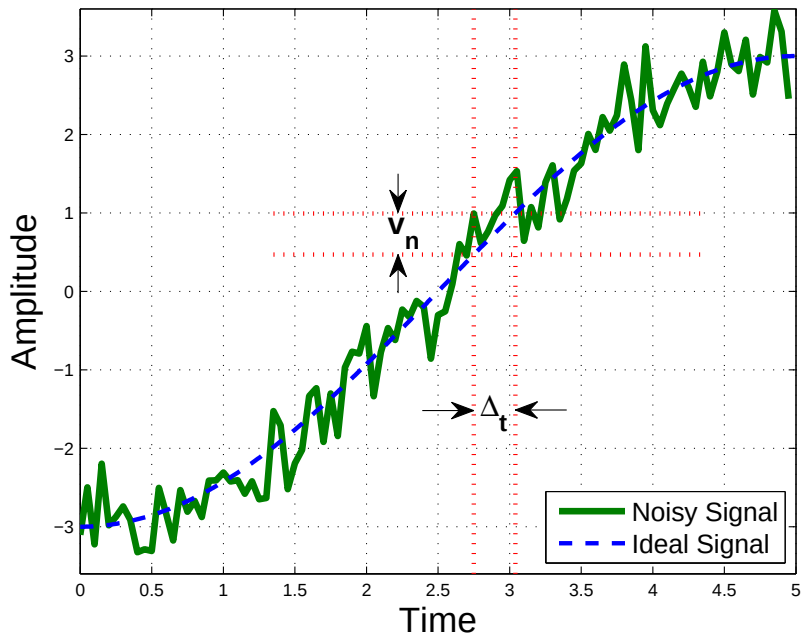

Figure 5.32: Demonstration of time jitter caused by thermal noise.

Substituting it into Eqn (5.21) yields:

$$f\left(v_n\right) = \frac{1}{\sqrt{2\pi v_{nRMS}^2}} e^{-\frac{(S\Delta t)^2}{2v_{nRMS}^2}}. \tag{5.24}$$

Dividing the numerators and denominators by S yields:

$$f\left(\Delta t\right) = \frac{1}{S} \frac{1}{\sqrt{\frac{2\pi v_{nRMS}^2}{S^2}}} e^{-\frac{\Delta t^2}{\frac{2v_{nRMS}^2}{S^2}}}. \tag{5.25}$$

Eqn (5.25) is similar to the Gaussian distribution shown in Eqn (5.21), except for the scale factor of $1/S$. Thus, the RMS jitter is:

$$Jitter_{RMS} = \frac{v_{nRMS}}{S}. \tag{5.26}$$

Fig. 5.33 illustrates that the RMS jitter varies with slew rate, given a thermal noise level of 31 mV RMS. It appears that a faster slew rate waveform results in lower jitter. The measured slew rate of the A-TDOA system is about 300 mV/ns, which corresponds to about 0.1 ns RMS jitter.

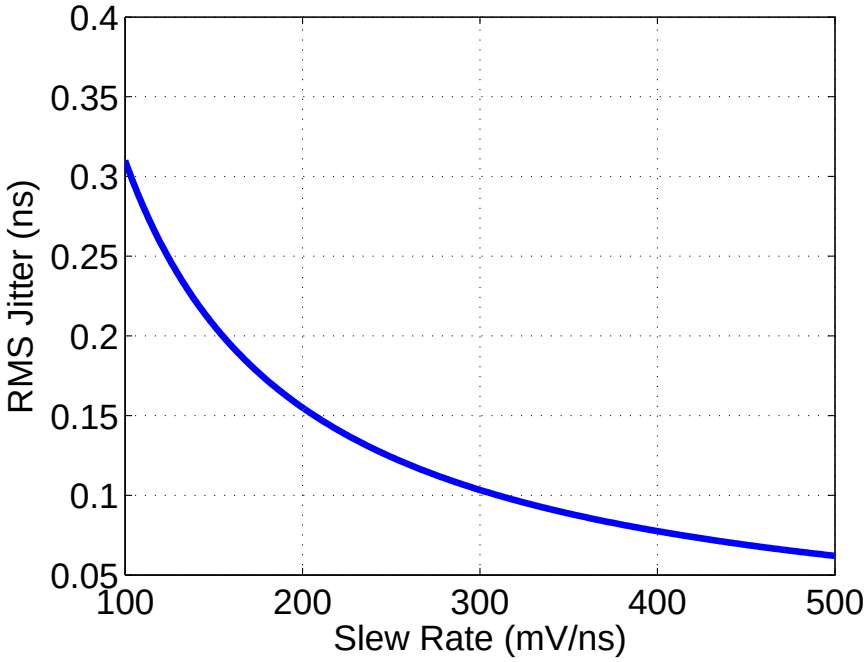

Figure 5.33: Slew rate versus RMS jitter.

The thermal noise is random in nature. It is not possible to predict the waveform and therefore it is not possible to reduce the effects by cancellation or other similar techniques. Nevertheless, by applying averaging technique, the noise variance can be reduced, which results in a reduction in threshold crossing time offset.

5.6.2 Unleveled Threshold Crossing

An A-TDOA system receiver takes two consecutive input pulses, one from an anchor transmitter and the other from the target. These two pulses undergo different signal paths and therefore their amplitudes at the receiver are different. The receiver is not able to identify and only amplify the weaker signal, and for that reason, the detector threshold must be set accordingly to accommodate the weaker signal.

Ideally, if the two pulses have equal amplitude, a threshold is set to a certain percentage of the peak amplitude, and the threshold crossing timings for both pulses are much alike. While in practice, these two pulses are unleveled, and by setting a threshold to a certain percentage of the weaker signal's peak amplitude, the threshold crossing timing for each pulse will be different, which results in a timing offset.

Fig. 5.34 demonstrates an unleveled threshold crossing scenario. Two pulses are

from an anchor transmitter and the target respectively, and they separate in time by 10 ns. Due to different channel condition and relative distance to the receiver, two pulses appearing at the receiver comparator input have different amplitude. The purple dashed line indicates a -3 dB threshold relative to the stronger pulse, while the red dashed line is relative to the weaker pulse. Ideally, the threshold is set according to each pulse's amplitude, which would result in 10.01 ns TDOA measurement. However, in practice, the red dashed line is used as the threshold for both pulses, and this leads to 10.3 ns TDOA measurement, causing 290 ps ranging error.

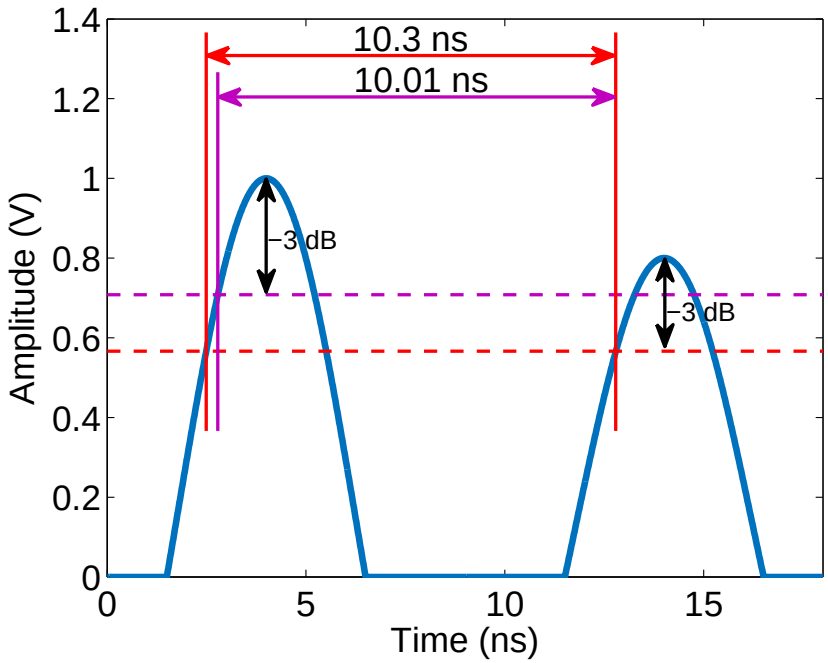

Figure 5.34: A demonstration of an unleveled threshold crossing.

To mitigate the unleveled threshold crossing, we placed sufficient gains in the receive chain in an effort to saturate both pulses to the maximum output voltage of the amplifier. This method was also studied and verified experimentally in [147]. Fig. 5.35 illustrates this method. Both pulses are amplified to a saturation voltage (in this example it is 2 V), and a -3 dB threshold is set for the comparator. This result in a TDOA ranging value of 10.13 ns, and therefore the timing error is reduced by more than 50%.

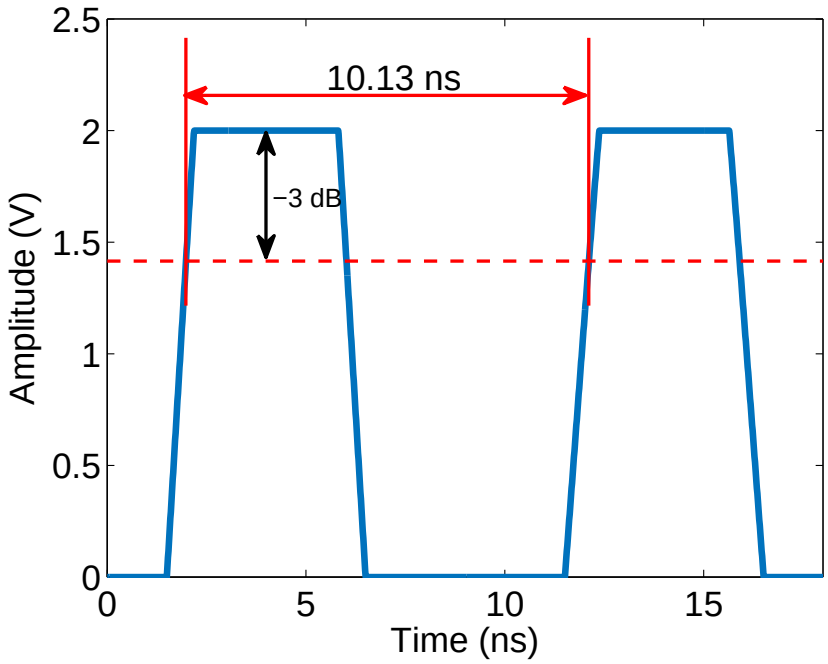

Figure 5.35: Demonstration of two pulses that are saturated.

5.6.3 UWB Propagation Channel

UWB propagation channels show fundamental differences from conventional narrow-band channels, mainly due to its fine time resolution [148]. In an UWB system, most of the multipath components (MPCs) can be distinguished, while in a narrow-band system, small scale fading occurs as a result of constructive or destructive superposition of the unresolvable multipath. Multipath is caused by three basic propagation mechanisms, namely, reflection, diffraction, and scattering of the transmitted signal. All three phenomena cause radio signal distortions and give rise to signal fades, as well as additional signal propagation losses. The impulse response of the UWB SV (Saleh-Valenzuela) model is given by [149] as

$$h(t) = \sum_{l=1}^{L} \sum_{k=1}^{K} \alpha_{k,l} \exp(j\phi_{k,l}) \, \delta(t - T_l - \tau_{k,l}), \tag{5.27}$$

where T_l denotes the delay of the l_{th} cluster, $\tau_{k,l}$ denotes the delay of the k_{th} channel tap of the l_{th} cluster relative to T_l, $\alpha_{k,l}$ and $\phi_{k,l}$ denote the magnitude and phase of the k_{th} channel tap in the l_{th} cluster, respectively.

The implemented A-TDOA prototype employs an energy detector in the receiver

to determine the received signal timing. As described earlier, a multiplier and an LPF constitute the energy detector which collects received signal energy over a time period. The LPF acts as a sliding window integrator, and the integration time is essentially determined by the LPF cut-off frequency, e.g., the wider the bandwidth, the shorter the time. The implemented LPF has approximately 18 ns integration time. Due to the fact that the received signal contains many MPCs of varying amplitudes, phase and time delays, the energy detector output varies accordingly. When significant MPCs arrive in the same integration window as the first arrived pulse, the energy detector outputs a stronger fast rising signal. In contrast, if the significant MPCs arrive in a later cluster, the energy detector outputs a gradual slope, which leads to an extra timing offset.

Fig. 5.36 and Fig. 5.37 demonstrate a scenario where an UWB pulse undergoes two different UWB channels. The blue trace is the received signal (at antenna) magnitude and the red one is the low pass filtered signal. Two vertical bars indicate the first peak of the two traces, and the time difference between the two is labeled in green text. Fig. 5.36 shows a cluster of MPCs arriving in the same integration window as the first arrived pulse, which results in 1.27 ns delay between the first pulse peak and the filtered signal peak. On the contrary, Fig. 5.37 illustrates a cluster of MPCs arriving in a later cluster, and the delay becomes 2.02 ns.

Note that the labeled time difference between the peak of the first received pulse and the filtered signal does not imply a timing error. Let us denote this time difference as Δt_{pp}. In an A-TDOA system, the time difference of the direct path and the re-transmitted path is the key measuring metrics. If a pulse undergoes identical channels for both the direct and re-transmitted path, we can expect an identical value Δt_{pp} for both paths' signals, and therefore the term Δt_{pp} cancels out in the TDOA measurement. Having said that, in practice, the direct and re-transmitted path channels are significantly different, therefore it is worthwhile to study the impact on the measured TDOA due to UWB channels.

Fig. 5.38 demonstrates received signals from both the direct path and reflected path. The time difference between the two (denoted as Δt) is the key measuring metric. For the sake of simplicity, Δt is measured at the peak of the two signals, as opposed to a fixed threshold relative to the weaker signal's peak.

We conducted Monte-Carlo simulation using IEEE 802.15.4 channel model [150] to study how much variation can be caused by the UWB propagation channel to the measured TDOA. Fig. 5.39 shows an example simulation case where channel model 1

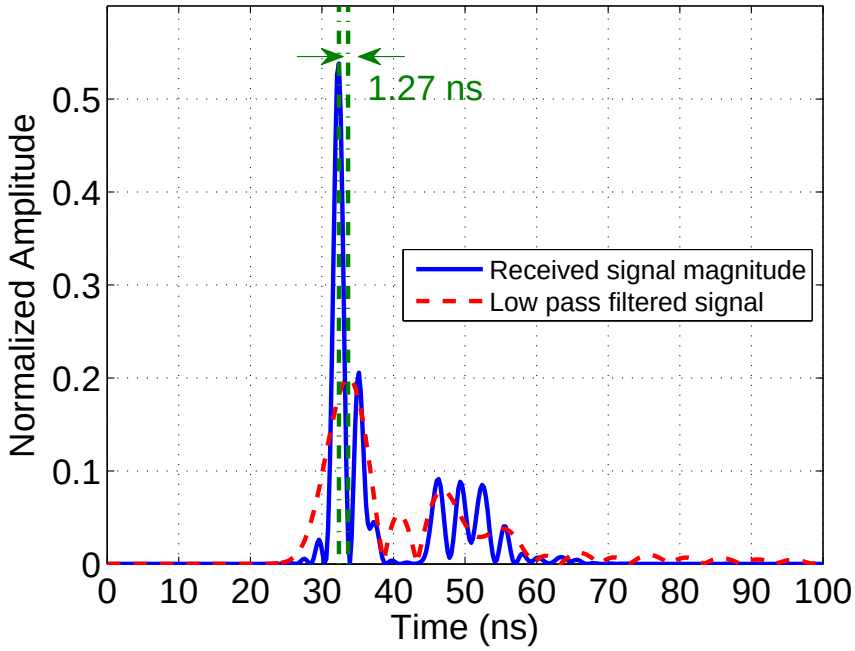

Figure 5.36: A demonstration of UWB pulse undergoes two different UWB channels.

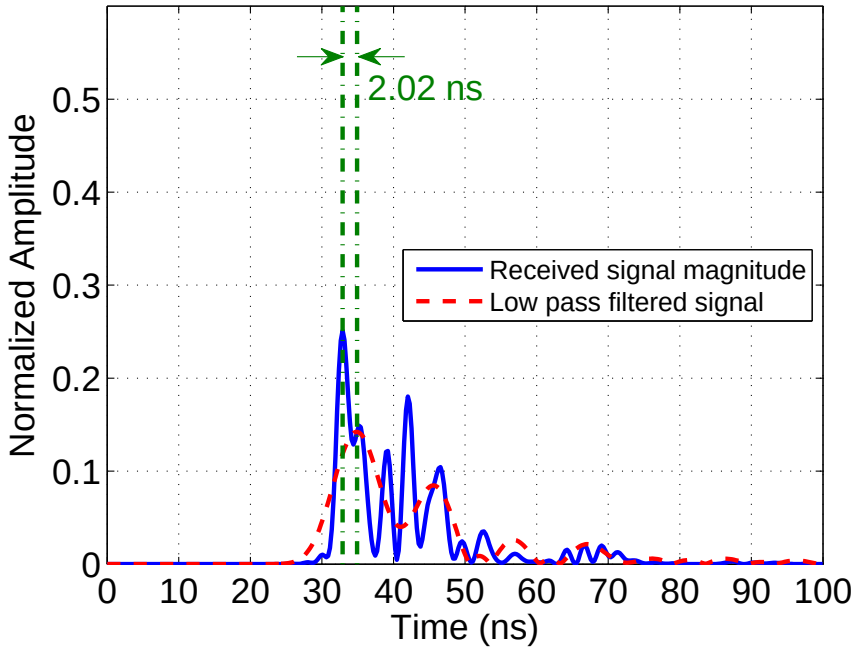

Figure 5.37: A demonstration of UWB pulse undergoes two different UWB channels.

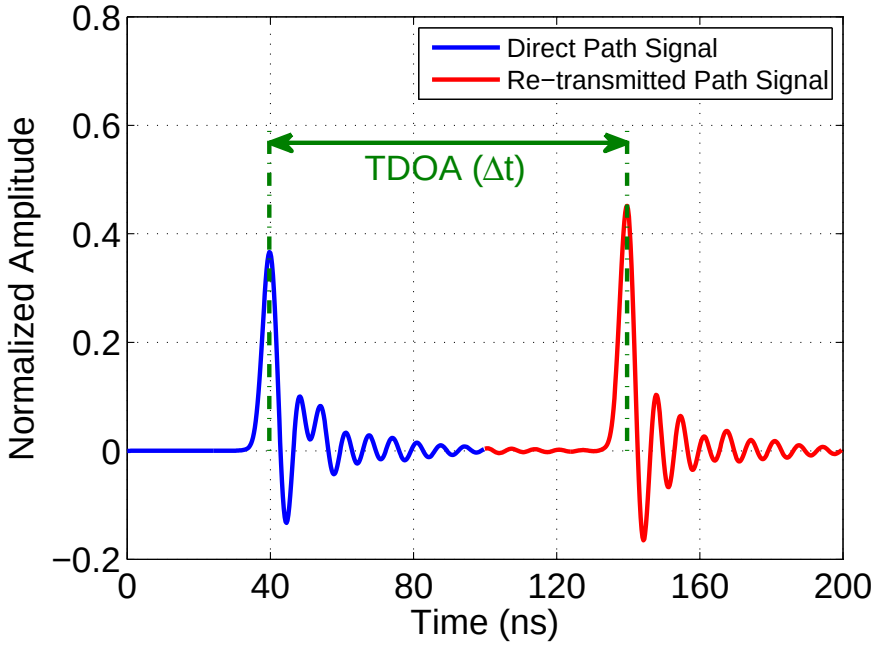

Figure 5.38: Received signal waveform from anchor Tx and target node.

(CM1) is used. Refer to [150] for the details of the channel model description. In this simulation, both direct and re-transmitted channels are CM1 and the nominal TDOA is set to 100 ns between the two received pulses. Note that for the re-transmitted path, the signal first undergoes one channel when the signal is transmitted from anchor Tx to the target, and undergoes another channel when the signal is re-transmitted from the target to anchor Rx. However, as far as the anchor Rx is concerned, only the latter channel makes impact, as the target node generates a new pulse when triggered. As can be seen, due to the fact that the two pulses undergo different propagation channels, the measured TDOA deviates from the nominal value. Fig. 5.39 shows approximately 50% of the measured TDOA is within ± 1 ns in CM1.

Table 5.3 summarizes the simulated TDOA statistics in different channel conditions. Several conclusions can be drawn from Table 5.3.

- In most cases, the mean TDOA is close to the nominal value of 100 ns, which suggests that if past data are considered in the current estimation, the error can be greatly reduced. Technique such as Kalman filter can be employed [151], as the filter constantly tracks the object position and can effectively reduce noise introduced by inaccurate detections.

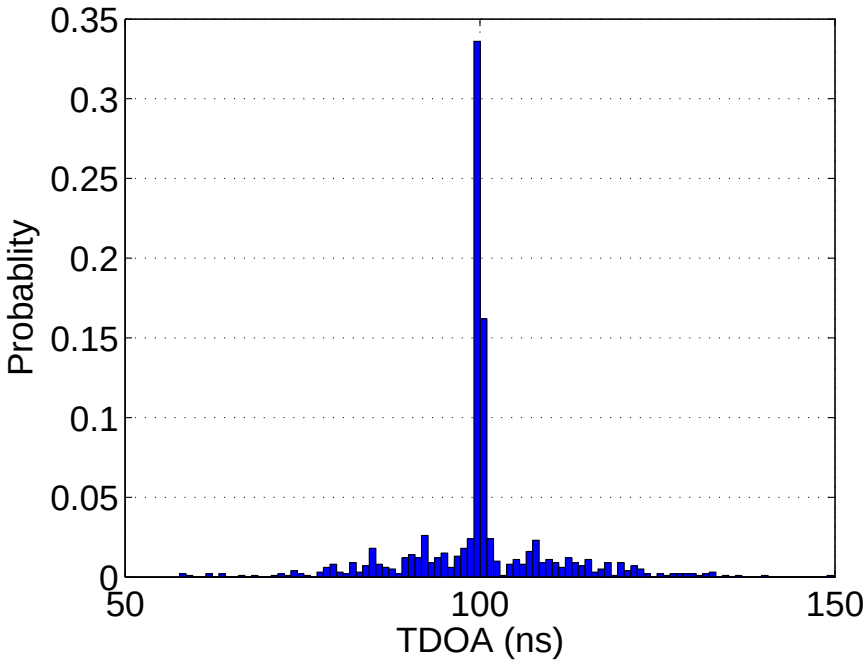

Figure 5.39: Distribution of the TDOA using CM1.

- Ideally, a receiver should react on the first received pulse regardless of its amplitude. This is particularly important especially in an NLOS condition, where the direct path signal level is weaker than an indirect one. However, in practice, it is difficult to identify a weak direct path signal, unless a very high speed sampling device is used and complex signal processing algorithms applied. As described before, we used a non-coherent receiver architecture that collects signal power not only from the direct path but also from multipath. The non-coherent approach has the practical advantage of simplicity but the direct path's arrival timing is lost. Therefore, in varying propagation conditions, the direct path may arrive before or after the non-coherent detector's threshold crossing timing, and causes timing errors. It is obvious and expected that in NLOS conditions, the standard deviation of the timing error is significantly greater than that in LOS conditions. Ranging error due to the effect of NLOS significantly degrades the position estimation accuracy. It is difficult to identify and compensate, yet there are many techniques available to mitigate [17]. In addition, the sub-GHz UWB signal possesses good obstacle penetration and excellent human tissue penetration capability [152], which helps mitigate the bias error caused by NLOS transmission.

Table 5.3: Simulated TDOA statistics in various UWB channel models.

Channel Model	Description	Mean Error (ns)	Standard Deviation (ns)	Percentage within ±1 ns
CM1	Residential LOS	99.9	9.2	52.0%
CM2	Residential NLOS	99.6	16.8	11.0%
CM3	Office LOS	100.2	6.3	27.9%
CM4	Office NLOS	100.1	10.0	10.2%
CM5	Outdoor LOS	100.3	17.1	29.1%
CM6	Outdoor NLOS	119.6	62.5	1.7%
CM7	Industrial LOS	99.9	7.4	52.7%
CM8	Industrial NLOS	105	33.1	3.0%

5.6.4 Clock Jitter

The core of the time interval measurements is the TDC, and of which the accuracy is solely determined by logical gate's propagation delay. The propagation delay in digital circuit varies significantly with fabrication process, temperature and supply voltage. Of them, temperature variations can cause delay time changes greater than 50% [153]. Nevertheless, it can be compensated by an external crystal oscillator, which has an advantage of very low frequency dependence on temperature. The TDC conducts a calibration by measuring 1 and 2 periods of the crystal oscillator, and the measured periods act as a timing reference to derive the gate's propagation delay. However, the clock period is not always constant and the deviation from the nominal periodicity is called jitter. As a result, clock jitter of the crystal oscillator impacts the calibration accuracy. We identify clock jitter as one of the error sources, and it can be modeled as an additive white Gaussian noise with zero mean and constant variance [154]. It is also noteworthy that in a short period of time, the clock jitter is relatively small. For example, a typical crystal oscillator has an accuracy of about 100 parts per million (PPM), and it drifts 100 fs in a measurement period of 1 us. Compared to the other error sources, clock jitter contribution is very small.

Chapter 6

Conclusion and Future Work

6.1 Conclusion

Accurate position information is particularly important in many applications where GPS signals are not available or the accuracy requirement cannot be met. Many solutions were proposed in the past to fill gaps. Nonetheless, they require clock synchronization to some extent or suffer from clock drifting. The main problem is to determine clock free object positions with anchor nodes' clock running asynchronously. This asynchronous feature offers great benefit of fast and post deployment in an emergency event. The aim of the work discussed in this thesis was to introduce and study an asynchronous TDOA localization system from concept to implementation.

The distinct advantage of the A-TDOA system is that no clock synchronization is needed. Therefore, the complexity of the system can be reduced significantly. Besides, by properly selecting the receiver anchor node, the A-TDOA system can achieve superior performance. In practice, as noise variance is dependent on the ranging distance, we have adopted a distance dependent noise model to derive CRLB and to conduct simulations.

More importantly, two new localization algorithms, namely the two-step (SDP+Taylor) and constrained LS algorithm have been proposed to estimate position in the A-TDOA system. The two-step estimator combines the SDP and Taylor series methods to achieve global convergence and superior estimation accuracy. In addition, its robustness has been demonstrated via providing good accuracy regardless of the noise power. The two-step algorithm can be applied in applications where accuracy is the most critical. The constrained LS algorithm obtains relatively good performance

while keeps the computational complexity low, and the convergence speed is fast. These properties are very useful in real-time systems and mobile devices where battery life and computational capability is limited. Simulations results have shown that the proposed two-step estimator's performance is close to the CRLB, while the constrained LS algorithm performs slightly worse than the two-step algorithm with the advantage of low complexity and fast convergence.

For the first time, a complete prototype based on an A-TDOA technique is implemented in hardware. The design target is low cost and low complexity, and therefore transmitter operating at avalanche mode, and non-coherent energy detection based receiver architecture was adopted. The target node design is based on receive and re-transmit technique and is prototyped in analog domain to avoid clock offset issue. In addition, a log-periodic toothed trapezoidal antenna was designed for wideband operation.

We have been able to obtain good performance using the implemented platform in various radio conditions. The measured RMS position errors are 20.7 cm and 15.2 cm in outdoor and indoor environment respectively. The comparison with the literature published results proves the excellent performance of the A-TDOA localization system presented here. Most importantly, the parameters of the hardware components as well as the UWB channel have been investigated to better understand their influence on the achievable accuracy of the system. Correspondingly, the correction and mitigation methods have been studied to help further improvement.

6.2 Future Work

- The measurement error adopted in this thesis as well as the previous works is always considered as Gaussian distributed. This is true when we only take thermal noise and random clock jitter into consideration. However, as was observed from real measurements, the radio propagation channel significantly impacts the ranging accuracy of a practical localization system. Therefore, a shift of focus can be made to the impact of wireless channel to a localization system. Studies on this topic can generate considerable practical significance.

- We employed a simple system layout with four anchor nodes placed at each vertex of a square in both the theoretical studies and practical measurements. In practice, a system layout could be very different depending on the floor

planning of the building and etc. The layout of the anchor nodes determines the geometric dilution of precision and in turn greatly impacts the achievable localization accuracy. More work can be done in future to study different layout and their impact on the system performance.

- We studied the A-TDOA localization system using four anchor nodes and one target node. In real life, it is not uncommon to have a lot more anchor nodes and target nodes. The fact that more anchor nodes are involved indicates that more ranging measurements can be conducted in a system, and potentially an improvement to the accuracy. Anchor nodes providing more accurate ranging measurements should be given a heavier weight, while the ones providing less accurate information should be given a lighter weight. Therefore, it is worthwhile to develop a technique to identify good and bad ranging measurements, and apply weights accordingly.

- The implemented platform operates in the sub-GHz range that provides several advantages such as better obstacle penetration, lower path loss, lower cost and etc. However, it also poses a challenge on antenna design, that is, designing an antenna with good return loss while keeping the size small. To reduce the antenna size, we suffered a poor return loss in the operation range, and it causes degradation in sensitivity. It would be interesting to develop a new system with a higher RF frequency, so that a smaller size antenna can be applied while having a good return loss.

- The implemented platform has the provision to adjust the voltage threshold for leading edge detection, so that the optimal threshold can be applied according to the received signal magnitude. However, the voltage threshold can only be adjusted manually. In future, it would be worthwhile to introduce an automatic gain control loop to the system to dynamically adjust the gains and the threshold depending on the input signal level.

Bibliography

[1] K. W. Cheung, H. C. So, W. K. Ma, and Y. T. Chan, "A constrained least squares approach to mobile positioning: algorithms and optimality," *EURASIP Journal on Advances in Signal Processing*, vol. 2006, no. 1, pp. 1–23, 2006.

[2] Y. Zhou, C. L. Law, Y. L. Guan, and F. Chin, "Indoor elliptical localization based on asynchronous UWB range measurement," *IEEE Trans. Instrum. Meas.*, vol. 60, no. 1, pp. 248–257, 2011.

[3] B. Zhen, H. B. Li, and R. Kohno, "Clock management in ultra-wideband ranging," in *Proc. IEEE Mobile and Wireless Communications Summit*, pp. 1–5, IEEE, 2007.

[4] S. Gezici and H. Poor, "Position estimation via ultra-wide-band signals," *Proceedings of the IEEE*, vol. 97, no. 2, pp. 386–403, 2009.

[5] A. Basu, J. Gao, J. S. Mitchell, and G. Sabhnani, "Distributed localization using noisy distance and angle information," in *Proc. ACM international symposium on Mobile ad hoc networking and computing*, pp. 262–273, ACM, 2006.

[6] H. So and L. Lin, "Linear least squares approach for accurate received signal strength based source localization," *IEEE Trans. Signal Processing*, vol. 59, no. 8, pp. 4035–4040, 2011.

[7] P. Pivato, L. Palopoli, and D. Petri, "Accuracy of RSS-based centroid localization algorithms in an indoor environment," *IEEE Trans. Instrum. Meas.*, vol. 60, no. 10, pp. 3451–3460, 2011.

[8] X. Li, "Collaborative localization with received-signal strength in wireless sensor networks," *IEEE Trans. Vehicular Technology*, vol. 56, no. 6, pp. 3807–3817, 2007.

[9] K. Kaemarungsi and P. Krishnamurthy, "Properties of indoor received signal strength for WLAN location fingerprinting," in *Proc. IEEE Conference on Mobile and Ubiquitous Systems: Networking and Services*, pp. 14–23, 2004.

[10] P. Prasithsangaree, P. Krishnamurthy, and P. Chrysanthis, "On indoor position location with wireless LANs," in *Proc. IEEE International Symposium on Personal, Indoor and Mobile Radio Communications*, vol. 2, pp. 720–724, 2002.

[11] A. W. Tsui, Y. H. Chuang, and H. H. Chu, "Unsupervised learning for solving RSS hardware variance problem in WiFi localization," *Mobile Networks and Applications*, vol. 14, no. 5, pp. 677–691, 2009.

[12] S. Aparicio, J. Pérez, A. M. Bernardos, and J. Casar, "A fusion method based on Bluetooth and WLAN technologies for indoor location," in *Proc. IEEE International Conference on Multisensor Fusion and Integration for Intelligent Systems*, pp. 487–491, IEEE, 2008.

[13] H. Cho, M. Kang, J. Park, B. Park, and H. Kim, "Performance analysis of location estimation algorithm in ZigBee networks using received signal strength," in *Proc. IEEE International Conference on Advanced Information Networking and Applications Workshop*, pp. 302–306, IEEE, 2007.

[14] N. Patwari, A. O. Hero III, and J. A. Costa, "Learning sensor location from signal strength and connectivity," in *Secure localization and time synchronization for wireless sensor and ad hoc networks*, pp. 57–81, Springer, 2007.

[15] Z. Ma and K. C. Ho, "TOA localization in the presence of random sensor position errors," in *Proc. IEEE International Conference on Acoustics, Speech and Signal Processing*, pp. 2468–2471, IEEE, 2011.

[16] A. Lewandowski and C. Wietfeld, "A comprehensive approach for optimizing ToA-localization in harsh industrial environments," in *Proc. Position Location and Navigation Symposium*, 2010.

[17] İ. Güvenç and C. C. Chong, "A survey on TOA based wireless localization and NLOS mitigation techniques," *IEEE Communications Surveys & Tutorials*, vol. 11, no. 3, pp. 107–124, 2009.

[18] E. Xu, Z. Ding, and S. Dasgupta, "Source localization in wireless sensor networks from signal time-of-arrival measurements," *IEEE Trans. Signal Processing*, vol. 59, no. 6, pp. 2887–2897, 2011.

[19] M. Sun and K. C. Ho, "Successive and asymptotically efficient localization of sensor nodes in closed-form," *IEEE Trans. on Signal Processing*, vol. 57, no. 11, pp. 4522–4537, 2009.

[20] S. Venkatesh and R. M. Buehrer, "NLOS mitigation using linear programming in ultrawideband location-aware networks," *IEEE Trans. Vehicular Technology*, vol. 56, no. 5, pp. 3182–3198, 2007.

[21] I. Guvenc, Z. Sahinoglu, and P. V. Orlik, "TOA estimation for IR-UWB systems with different transceiver types," *IEEE Trans. Microwave Theory and Techniques*, vol. 54, no. 4, p. 1876, 2006.

[22] X. Li, K. Pahlavan, and J. Beneat, "Performance of TOA estimation techniques in indoor multipath channels," in *Proc. IEEE international symposium on personal, indoor and mobile radio communications*, vol. 2, 2002.

[23] E. Kaplan and C. Hegarty, *Understanding GPS: principles and applications*. Artech house, 2005.

[24] S. Gezici, Z. Tian, G. B. Giannakis, H. Kobayashi, A. F. Molisch, H. V. Poor, and Z. Sahinoglu, "Localization via ultra-wideband radios: a look at positioning aspects for future sensor networks," *IEEE Signal Processing Magazine*, vol. 22, no. 4, pp. 70–84, 2005.

[25] X. Wei, L. Wang, and J. Wan, "A new localization technique based on network TDOA information," in *Proc. IEEE International Conference on Telecommunications*, pp. 127–130, IEEE, 2006.

[26] R. Ye and H. Liu, "UWB TDOA localization system: Receiver configuration analysis," in *Proc. IEEE International Symposium on Signals Systems and Electronics*, vol. 1, pp. 1–4, IEEE, 2010.

[27] K. C. Ho, X. Lu, and L. Kovavisaruch, "Source localization using TDOA and FDOA measurements in the presence of receiver location errors: analysis and solution," *IEEE Trans. Signal Processing*, vol. 55, no. 2, pp. 684–696, 2007.

[28] K. Yang, G. Wang, and Z. Q. Luo, "Efficient convex relaxation methods for robust target localization by a sensor network using time differences of arrivals," *IEEE Trans. Signal Processing*, vol. 57, no. 7, pp. 2775–2784, 2009.

[29] L. Yang and K. C. Ho, "An approximately efficient TDOA localization algorithm in closed-form for locating multiple disjoint sources with erroneous sensor positions," *IEEE Trans. Signal Processing*, vol. 57, no. 12, pp. 4598–4615, 2009.

[30] M. R. Gholami, S. Gezici, and E. G. Strom, "A concave-convex procedure for TDOA based positioning," *IEEE Communications Letters*, vol. 17, no. 4, pp. 765–768, 2013.

[31] Y. Chan and K. Ho, "A simple and efficient estimator for hyperbolic location," *IEEE Trans. Signal Processing*, vol. 42, no. 8, pp. 1905–1915, 1994.

[32] F. Gustafsson and F. Gunnarsson, "Positioning using time-difference of arrival measurements," in *Proc. IEEE International Conference on Acoustics, Speech, and Signal Processing*, vol. 6, pp. VI–553, IEEE, 2003.

[33] M. Kwak and J. Chong, "A new double two-way ranging algorithm for ranging system," in *Proc. IEEE International Conference on Network Infrastructure and Digital Content*, pp. 470–473, IEEE, 2010.

[34] D. Kreiser, D. Martynenko, O. Klymenko, and G. Fischer, "Simple and efficient localization method for IR-UWB systems based on two-way ranging," in *Proc. IEEE Int. Conf. on Microwaves for Intelligent Mobility*, pp. 1–4, IEEE, 2015.

[35] T. Ichikawa, "Application of high-precision two-way ranging to the spacecraft navigation," in *Proc. of SICE Annual Conference*, pp. 817–821, IEEE, 2010.

[36] D. Wang, R. Kannan, L. Wei, and B. Tay, "Time of flight based two way ranging for real time locating systems," in *Proc. IEEE Conference on Robotics Automation and Mechatronics*, pp. 199–205, IEEE, 2010.

[37] Z. Sahinoglu and S. Gezici, "Ranging in the IEEE 802.15. 4a standard," in *Proc. IEEE Wireless and Microwave Technology Conference*, pp. 1–5, 2006.

[38] T. C. Karalar and J. Rabaey, "An rf tof based ranging implementation for sensor networks," in *Proc. IEEE International Conference on Communications*, vol. 7, pp. 3347–3352, IEEE, 2006.

[39] R. Peng and M. L. Sichitiu, "Angle of arrival localization for wireless sensor networks," in *Proc. IEEE Commun. Soc. Conf. Sensor Ad Hoc Commun. Netw.*, vol. 1, pp. 374–382, IEEE, 2006.

[40] D. Niculescu and B. Nath, "Ad hoc positioning system (APS) using AOA," in *Proc. IEEE Conference on Computer and Communications*, vol. 3, pp. 1734–1743, Ieee, 2003.

[41] W. Zhang, Q. Yin, H. Chen, F. Gao, and N. Ansari, "Distributed angle estimation for localization in wireless sensor networks," *IEEE Trans. Wireless Communications*, vol. 12, no. 2, pp. 527–537, 2013.

[42] K. Doğançay and H. Hmam, "Optimal angular sensor separation for AOA localization," *Signal Processing*, vol. 88, no. 5, pp. 1248–1260, 2008.

[43] P. Kułakowski, J. Vales-Alonso, E. Egea-López, W. Ludwin, and J. García-Haro, "Angle-of-arrival localization based on antenna arrays for wireless sensor networks," *Computers & Electrical Engineering*, vol. 36, no. 6, pp. 1181–1186, 2010.

[44] J. H. Winters, "Smart antenna techniques and their application to wireless ad hoc networks," *IEEE Wireless Communications*, vol. 13, no. 4, pp. 77–83, 2006.

[45] R. T. Weverka and K. H. Wagner, "Adaptive phased-array radar processing using photorefractive crystals," in *Proc. International Society for Optics and Photonics*, pp. 173–182, International Society for Optics and Photonics, 1990.

[46] A. O. Boukalov and S. G. Häggman, "System aspects of smart-antenna technology in cellular wireless communications-an overview," *IEEE Trans. Microwave Theory and Techniques*, vol. 48, no. 6, pp. 919–929, 2000.

[47] M. Boushaba, A. Hafid, and A. Benslimane, "High accuracy localization method using AoA in sensor networks," *Computer Networks*, vol. 53, no. 18, pp. 3076–3088, 2009.

[48] V. Y. Zhang and A. K. Wong, "Combined AOA and TOA NLOS localization with nonlinear programming in severe multipath environments," in *Proc. IEEE Conference on Wireless Communications and Networking*, pp. 1–6, IEEE, 2009.

[49] L. Xiong, "A selective model to suppress NLOS signals in angle-of-arrival (AOA) location estimation," in *Proc. IEEE International Symposium on Personal, Indoor and Mobile Radio Communications*, vol. 1, pp. 461–465, IEEE, 1998.

[50] Y. Zhou, C. Law, Y. Guan, and F. Chin, "Indoor elliptical localization based on asynchronous UWB range measurement," *IEEE Trans. Instrum. Measure.*, pp. 248–257, Jan 2011.

[51] Y. Wang, X. Ma, and G. Leus, "Robust time-based localization for asynchronous networks," *IEEE Trans. Signal Process.*, pp. 4397–4410, Sept 2011.

[52] T. Wang, "Ranging energy optimization for a TDOA-based distributed robust sensor positioning system," *Intl. Journal of Distributed Sensor Networks*, pp. 1–12, Nov 2010.

[53] N. Patwari, A. Hero, M. Perkins, N. Correal, and R. O'dea, "Relative location estimation in wireless sensor networks," *IEEE Trans. Signal Processing*, vol. 51, no. 8, pp. 2137–2148, 2003.

[54] C. Chang and A. Sahai, "Estimation bounds for localization," in *Proc. IEEE Communications Society Conference on Sensor and Ad Hoc Communications and Networks*, pp. 415–424, Oct 2004.

[55] A. Goldsmith, *Wireless communications*. Cambridge University Press, 2005.

[56] T. Jia and R. M. Buehrer, "A new Cramer-Rao lower bound for TOA-based localization," in *Proc. IEEE Military Communications Conference*, pp. 1–5, IEEE, 2008.

[57] S. Kay, *Fundamentals of Statistical Signal Processing, Volume I: Estimation Theory (v. 1)*. Prentice Hall, 1993.

[58] M. Gholami, S. Gezici, and E. Strom, "TDOA based positioning in the presence of unknown clock skew," *IEEE Trans. Communications*, vol. 61, no. 6, pp. 2522–2534, 2013.

[59] Y. Chan, H. Hang, and P. Ching, "Exact and approximate maximum likelihood localization algorithms," *IEEE Trans. Vehicular Technology*, vol. 55, no. 1, pp. 10–16, 2006.

[60] A. E. Waadt, C. Kocks, S. Wang, G. H. Bruck, and P. Jung, "Maximum likelihood localization estimation based on received signal strength," in *Proc. IEEE International Symposium on Applied Sciences in Biomedical and Communication Technologies*, pp. 1–5, IEEE, 2010.

[61] G. Destino and G. Abreu, "On the maximum likelihood approach for source and network localization," *IEEE Trans. Signal Processing*, vol. 59, no. 10, pp. 4954–4970, 2011.

[62] A. Coluccia and F. Ricciato, "On ML estimation for automatic RSS-based indoor localization," in *Proc. IEEE International Symposium on Wireless Pervasive Computing (ISWPC)*, pp. 495–502, IEEE, 2010.

[63] L. Lin, H. So, and Y. Chan, "Accurate and simple source localization using differential received signal strength," *Digital Signal Processing*, vol. 23, no. 3, pp. 736–743, 2013.

[64] B. Yaakov, X. Li, and K. Thiagalingam, "Estimation with applications to tracking and navigation," *New York: Johh Wiley and Sons*, vol. 245, 2001.

[65] W. Foy, "Position-location solutions by Taylor-series estimation," *IEEE Trans. Aerospace and Electronic Systems*, vol. 2, no. AES-12, pp. 187–194, 1976.

[66] I. Güvenç, C. Chong, F. Watanabe, and H. Inamura, "NLOS identification and weighted least-squares localization for UWB systems using multipath channel statistics," *EURASIP Journal on Advances in Signal Processing*, vol. 2008, no. 1, pp. 1–14, 2007.

[67] M. Spirito, "On the accuracy of cellular mobile station location estimation," *IEEE Trans. Vehicular Technology*, vol. 50, no. 3, pp. 674–685, 2001.

[68] J. Caffery and J. James, "A new approach to the geometry of TOA location," in *Proc. IEEE Vehicular Technology Conference*, vol. 4, pp. 1943–1949, IEEE, 2000.

[69] J. Smith and J. Abel, "Closed-form least-squares source location estimation from range-difference measurements," *IEEE Trans. Acoust., Speech. Sig. Proc.*, vol. 35, no. 12, pp. 1661–1669, 1987.

[70] Y. Huang, J. Benesty, G. W. Elko, and R. M. Mersereati, "Real-time passive source localization: A practical linear-correction least-squares approach," *IEEE Trans. Speech and Audio Proc.*, vol. 9, no. 8, pp. 943–956, 2001.

[71] A. M. C. So and Y. Ye, "Theory of semidefinite programming for sensor network localization," *Mathematical Programming*, vol. 109, no. 2-3, pp. 367–384, 2007.

[72] P. Biswas, T. Liang, K. Toh, Y. Ye, and T. Wang, "Semidefinite programming approaches for sensor network localization with noisy distance measurements," *IEEE transactions on automation science and engineering*, vol. 3, no. 4, p. 360, 2006.

[73] K. Lui, F. Chan, and H. So, "Semidefinite programming approach for range-difference based source localization," *IEEE Trans. on Signal Processing*, pp. 1630–1633, April 2009.

[74] R. W. Ouyang, A. K. S. Wong, and C. T. Lea, "Received signal strength-based wireless localization via semidefinite programming: noncooperative and cooperative schemes," *Vehicular Technology, IEEE Transactions on*, vol. 59, no. 3, pp. 1307–1318, 2010.

[75] C. Meng, Z. Ding, and S. Dasgupta, "A semidefinite programming approach to source localization in wireless sensor networks," *Signal Processing Letters, IEEE*, vol. 15, pp. 253–256, 2008.

[76] E. Xu, Z. Ding, and S. Dasgupta, "Reduced complexity semidefinite relaxation algorithms for source localization based on time difference of arrival," *Mobile Computing, IEEE Transactions on*, vol. 10, no. 9, pp. 1276–1282, 2011.

[77] K. Lui, J. Zheng, and H. So, "Particle swarm optimization for time-difference-of-arrival based localization," in *Proc. European Signal Processing Conference*, pp. 414–417, Citeseer, 2007.

[78] J. Blumenthal, R. Grossmann, F. Golatowski, and D. Timmermann, "Weighted centroid localization in zigbee-based sensor networks," in *Proc. IEEE International Symposium on Intelligent Signal Processing*, pp. 1–6, IEEE, 2007.

[79] Z. Sahinoglu, S. Gezici, and I. Guvenc, "Ultra-wideband positioning systems," *Cambridge, New York*, 2008.

[80] G. Golub and C. Van Loan, *Matrix computations*. Johns Hopkins University Press, 1996.

[81] A. Antoniou and W.-S. Lu, *Practical optimization: algorithms and engineering applications*. Springer, New York, 2007.

[82] M. Grant, S. Boyd, and Y. Ye, "CVX: Matlab software for disciplined convex programming," *avialable at http://www.stanford.edu/ boyd/cvx/*, 2008.

[83] C. Zhang, M. Kuhn, B. Merkl, A. Fathy, and M. Mahfouz, "Real-time noncoherent UWB positioning radar with millimeter range accuracy: theory and experiment," *IEEE Trans. Microwave. Theory Tech.*, vol. 58, no. 1, pp. 9–20, 2010.

[84] H. A. Shaban, M. A. El-Nasr, and R. M. Buehrer, "Localization with submillimeter accuracy for UWB-based wearable human movement radar systems," *Journal of Electromagnetic Waves and Applications*, vol. 25, no. 11-12, pp. 1633–1644, 2011.

[85] C. Meier, A. Terzis, and S. Lindenmeier, "A robust 3D high precision radio location system," in *Proc. IEEE International Microwave Symposium*, pp. 397–400, IEEE, 2007.

[86] "Ubisense." `http://www.ubisense.net/en/index.html`.

[87] "DART UWB." `http://www.zebra.com`.

[88] "PulsON 410." `http://www.timedomain.com/`.

[89] "ScenSor." `http://www.decawave.com/products`.

[90] G. Ossberger, T. Buchegger, E. Schimbäck, A. Stelzer, and R. Weigel, "Non-invasive respiratory movement detection and monitoring of hidden humans using ultra wideband pulse radar," in *Proc. International Workshop on Ultra Wideband Systems Joint with Conference on Ultrawideband Systems and Technologies*, pp. 395–399, IEEE, 2004.

[91] G. Selimis, J. Romme, H. Pflug, K. Philips, G. Dolmans, and H. de Groot, "Sub-meter UWB localization: Low complexity design and evaluation in a real localization system," in *Proc. IEEE International Symposium on Personal Indoor and Mobile Radio Communications*, pp. 186–191, IEEE, 2013.

[92] K. Whitehouse, C. Karlof, and D. Culler, "A practical evaluation of radio signal strength for ranging-based localization," *ACM SIGMOBILE Mobile Computing and Communications Review*, vol. 11, no. 1, pp. 41–52, 2007.

[93] M. Sugano, T. Kawazoe, Y. Ohta, and M. Murata, "Indoor localization system using RSSI measurement of wireless sensor network based on ZigBee standard," in *Proc. IASTED Int. Conf. WSN*, pp. 1–6, 2006.

[94] E. Elnahrawy, X. Li, and R. P. Martin, "The limits of localization using signal strength: A comparative study," in *Proc. IEEE Commun. Soc. Conf. Sensor Ad Hoc Commun. Netw.*, pp. 406–414, IEEE, 2004.

[95] A. De Angelis, M. Dionigi, A. Moschitta, R. Giglietti, and P. Carbone, "Characterization and modelling of an experimental UWB pulse-based distance measurement system," *IEEE Trans. Instrum. Meas.*, vol. 58, no. 5, pp. 1479–1486, 2009.

[96] A. Cazzorla, G. De Angelis, A. Moschitta, M. Dionigi, F. Alimenti, and P. Carbone, "A 5.6-GHz UWB position measurement system," *IEEE Trans. Instrum. Meas.*, vol. 3, no. 62, pp. 675–683, 2013.

[97] G. Fischer, O. Klymenko, and D. Martynenko, "Time-of-Arrival measurement extension to a non-coherent impulse radio UWB transceiver," in *Proc. Workshop on Positioning, Navigation and Communication*, pp. 265–270, IEEE, 2008.

[98] A. Gerosa, S. Soldà, A. Bevilacqua, D. Vogrig, and A. Neviani, "An energy-detector for noncoherent impulse-radio UWB receivers," *IEEE Transactions on Circuits and Systems I*, vol. 56, no. 5, pp. 1030–1040, 2009.

[99] H. Liu, H. Darabi, P. Banerjee, and J. Liu, "Survey of wireless indoor positioning techniques and systems," *IEEE Trans. Syst., Man, Cybern.*, vol. 37, no. 6, pp. 1067–1080, 2007.

[100] Y. Gu, A. Lo, and I. Niemegeers, "A survey of indoor positioning systems for wireless personal networks," *IEEE Communications Surveys & Tutorials*, vol. 11, no. 1, pp. 13–32, 2009.

[101] D. Jourdan, D. Dardari, and M. Win, "Position error bound for UWB localization in dense cluttered environments," *IEEE Trans. Aero. Elec. Sys.*, vol. 44, no. 2, pp. 613–628, 2008.

[102] H. Wymeersch, J. Lien, and M. Z. Win, "Cooperative localization in wireless networks," in *Proc. IEEE special issue on Ultra-Wide Bandwidth (UWB) Technology & Emerging Applications*, vol. 97, pp. 427–450, IEEE, 2009.

[103] N. Patwari, J. Ash, S. Kyperountas, A. Hero, R. Moses, and N. Correal, "Locating the nodes: cooperative localization in wireless sensor networks," *IEEE Trans. Signal Process.*, pp. 54–69, July 2005.

[104] Unisense, "The unisense precise real-time location system." `http://www.ti.com/lit/ds/symlink/cd4007ub.pdf`.

[105] Time Domain, "PulsON 400 RCM data sheet." `http://www.timedomain.com`, 2011.

[106] A. Prorok, A. Arfire, A. Bahr, J. R. Farserotu, and A. Martinoli, "Indoor navigation research with the Khepera III mobile robot: An experimental baseline with a case-study on ultra-wideband positioning," in *Proc. IEEE Int. Conf. on Indoor Positioning and Indoor Navigation*, pp. 1–9, IEEE, 2010.

[107] P. Karbownik, G. Krukar, M. M. Pietrzyk, N. Franke, and T. vd Gruen, "Experimental validation of the ultra-wideband technology-based localization platform," in *Proc. Int. Conf. on Indoor Positioning and Indoor Navigation IPIN*, vol. 3, 2012.

[108] J. Xu, M. Ma, and C. Law, "Performance of time-difference-of-arrival ultra wideband indoor localisation," *IET Science, Measurement & Technology*, vol. 5, no. 2, pp. 46–53, 2011.

[109] Ö. Çetin, H. Nazli, R. Gürcan, H. Öztürk, H. Güneren, Y. Yelkovan, M. Çayır, H. Çelebi, and H. P. Partal, "An experimental study of high precision TOA based UWB positioning systems," in *Proc. IEEE Int. Conf. on Ultra-Wideband*, pp. 357–361, IEEE, 2012.

[110] B. Silva, Z. Pang, J. Akerberg, J. Neander, and G. Hancke, "Experimental study of UWB-based high precision localization for industrial applications," in *Proc. IEEE Int. Conf. on Ultra-WideBand*, pp. 280–285, IEEE, 2014.

[111] J. Tiemann, F. Schweikowski, and C. Wietfeld, "Design of an UWB indoor-positioning system for UAV navigation in GNSS-denied environments," in *proc.*

IEEE Int. Conf. on Indoor Positioning and Indoor Navigation (IPIN), pp. 1–7, IEEE, 2015.

[112] R. Merz, F. Chastellain, A. Blatter, C. Botteron, and P. Farine, "An experimental platform for an indoor location and tracking system," in *Proc. European Navigation Conference, Toulouse, France*, 2008.

[113] Y. Zhou, C. L. Law, and J. Xia, "Ultra low-power RFID tag with precision localization using IR-UWB," in *Proc. IEEE MTT-S Int. Microwave Symposium Digest (MTT)*, pp. 1–4, IEEE, 2011.

[114] L. Zwirello, M. Harter, H. Berchtold, J. Schlichenmaier, and T. Zwick, "Analysis of the measurement results performed with an ultra-wideband indoor locating system," in *Proc. German Microwave Conference (GeMiC)*, pp. 1–4, IEEE, 2012.

[115] A. De Angelis, S. Dwivedi, and P. Handel, "Characterization of a flexible UWB sensor for indoor localization," *IEEE Trans. Instrum. Meas.*, vol. 62, no. 5, pp. 905–913, 2013.

[116] B. Waldmann, R. Weigel, R. Ebelt, and M. Vossiek, "An ultra-wideband local positioning system for highly complex indoor environments," in *Proc. Int. Conf. on Localization and GNSS (ICL-GNSS)*, pp. 1–5, IEEE, 2012.

[117] T. Sathyan, D. Humphrey, and M. Hedley, "WASP: A system and algorithms for accurate radio localization using low-cost hardware," *IEEE Tran. on Syst., Man, Cyber.*, vol. 41, no. 2, pp. 211–222, 2011.

[118] A. De Angelis, M. Dionigi, R. Giglietti, and P. Carbone, "Experimental comparison of low-cost sub-nanosecond pulse generators," *IEEE Trans. Instrum. Meas.*, vol. 60, no. 1, pp. 310–318, 2011.

[119] A. Kilpelä and J. Kostamovaara, "Laser pulser for a time-of-flight laser radar," *Review of scientific instruments*, vol. 68, no. 6, pp. 2253–2258, 1997.

[120] J. Williams, "High speed amplifier techniques," *Linear Technology Corporation, Application Note*, vol. 47, pp. 35–37, 1991.

[121] Linear Technology Corporation, "LT1073-Micropower, DC and Adjustable, DC Converter." `http://www.linear.com/product/LT1073`, 2000.

[122] Y. L. Chao and R. A. Scholtz, "Ultra-wideband transmitted reference systems," *IEEE Trans. Veh. Tech.*, vol. 54, no. 5, pp. 1556–1569, 2005.

[123] X. Dong, L. Jin, and P. Orlik, "A new transmitted reference pulse cluster system for UWB communications," *IEEE Trans. Veh. Tech.*, vol. 57, no. 5, pp. 3217–3224, 2008.

[124] M. Mroué, S. Haese, G. El-Zein, S. Mallégol, and S. Paquelet, "A non-coherent multi-band IR-UWB HDR transceiver based on energy detection," in *Proc. IEEE Int. Conf. on Electronics, Circuits, and Systems (ICECS)*, pp. 898–901, IEEE, 2010.

[125] O. Klymenko, G. Fischer, and D. Martynenko, "A high band non-coherent impulse radio UWB receiver," in *Proc. IEEE Int. Conf. on Ultra-Wideband*, vol. 3, pp. 25–29, IEEE, 2008.

[126] R. M. Fano, "Theoretical limitations on the broadband matching of arbitrary impedances," *Journal of the Franklin Institute*, vol. 249, no. 1, pp. 57–83, 1950.

[127] R. W. Waugh and R. R. Buted, "The zero bias schottky diode detector at temperature extremes-problems and solutions," in *Proceedings of the WIRELESS Symposium*, pp. 175–183, 1996.

[128] C. Chen and Z. Li, "A low-power cmos analog multiplier," *IEEE Trans. Circuits and Systems Part II*, vol. 53, no. 2, p. 100, 2006.

[129] A. Naderi, H. Mojarrad, H. Ghasemzade, A. Khoei, and K. Hadidi, "Circuit implementation of programmable high-resolution rational-powered membership functions in standard cmos technology," in *Proc. IEEE EUROCON*, pp. 1236–1241, IEEE, 2009.

[130] Analog Devices.Inc, "Mixers and modulators." `http://www.analog.com/media/en/training-seminars/tutorials/MT-080.pdf`.

[131] Analog Devices.Inc, "ADL5391 datasheet." `http://www.analog.com/media/en/technical-documentation/data-sheets/ADL5391.pdf`.

[132] S. Tavares, "A comparison of integration and low-pass filtering," *IEEE Trans. Instrum. Meas.*, vol. 15, no. 1/2, pp. 33–38, 1966.

[133] ACAM, "Time-to-digital converter TDC-GP2 datasheet." http://www.acam.de/products/time-to-digital-converter/tdc-gp2/.

[134] A. De Angelis, S. Dwivedi, and P. Handel, "Application of time-to-digital converters to radio-frequency distance measurement," in *Proc. IEEE Nordic-Mediterranean Workshop on Time-to-Digital Converters*, pp. 1–5, IEEE, 2013.

[135] Texas Instruments, "Layout Review Techniques for Low Power RF Designs." http://www.ti.com/lit/an/swra367a/swra367a.pdf, 2012.

[136] J. Mark, "An overview of sub-GHz UWB technology for 802.15.4a PHY," 2005.

[137] H. G. Schantz, "UWB magnetic antennas," in *Proc. IEEE Antennas and Propagation Society International Symposium*, vol. 3, pp. 604–607, IEEE, 2003.

[138] E. M. Turner and W. P. Turner, "Scimitar antenna," Dec 1961. US Patent 3015101.

[139] H. G. Schantz and L. Fullerton, "The diamond dipole: a gaussian impulse antenna," in *Proc. IEEE Antennas and Propagation Society International Symposium*, vol. 4, pp. 100–103, IEEE, 2001.

[140] H. Schantz, "Planar elliptical element ultra-wideband dipole antennas," in *IEEE Antennas and Propagation Society International Symposium*, vol. 3, pp. 44–47, IEEE; 1999, 2002.

[141] B. H. Phu, P. M. Quang, D. T. Phuoc, and L. N. Duy, "A log-periodic saw-toothed planar antenna for UHF ultra-wideband applications," in *Proc. IEEE Int. Conf. on Advanced Technologies for Communications*, pp. 689–692, IEEE, 2013.

[142] Y. J. Ren, C. P. Lai, P. H. Chen, and R. M. Narayanan, "Compact ultrawideband UHF array antenna for through-wall radar applications," *IEEE Antennas and Wireless Propagation Letters*, vol. 8, pp. 1302–1305, 2009.

[143] A. X. Chen, T. H. Jiang, Z. D. Chen, and D. Su, "A novel low-profile wideband UHF antenna," *Progress In Electromagnetics Research*, vol. 121, pp. 75–88, 2011.

[144] R. DuHamel and F. Ore, "Logarithmically periodic antenna designs," *RN*, vol. 1, p. 7, 1958.

[145] J. D. Dyson, "The equiangular spiral antenna," *IEEE Trans. Ant. Prop.*, vol. 7, no. 2, pp. 181–187, 1959.

[146] H. G. Booker, "Slot aerials and their relation to complementary wire aerials (babinets principle)," *J. IEE*, vol. 93, no. pt III, pp. 620–626, 1946.

[147] S. Krishnan, P. Sharma, V. Kumar, L. K. Seong, and W. Wenjiang, "Reducing timing jitter in UWB-IR threshold detectors," in *Proc. IEEE Int. Conf. on Ultra-Wideband (ICUWB)*, vol. 1, pp. 1–4, IEEE, 2010.

[148] A. F. Molisch, D. Cassioli, C. C. Chong, S. Emami, A. Fort, B. Kannan, J. Karedal, J. Kunisch, H. G. Schantz, and K. Siwiak, "A comprehensive standardized model for ultrawideband propagation channels," *IEEE Trans. Ant. Prop.*, vol. 54, no. 11, pp. 3151–3166, 2006.

[149] A. A. Saleh and R. A. Valenzuela, "A statistical model for indoor multipath propagation," *IEEE Journal on Selected Areas in Communications*, vol. 5, no. 2, pp. 128–137, 1987.

[150] A. F. Molisch, K. Balakrishnan, D. Cassioli, C. C. Chong, S. Emami, A. Fort, J. Karedal, J. Kunisch, H. Schantz, and U. Schuster, "IEEE 802.15. 4a channel model-final report," *IEEE P802*, vol. 15, no. 04, p. 0662, 2004.

[151] C. D. Wann, Y. J. Yeh, and C. S. Hsueh, "Hybrid TDOA/AOA indoor positioning and tracking using extended Kalman filters," in *Proc. IEEE Vehicular Technology Conference*, vol. 3, pp. 1058–1062, IEEE, 2006.

[152] M. Stoopman and A. S. Wouter, "Sub-GHz UWB biomedical communication," in *Proc. IEEE Biomedical Circuits and Systems Conference*, pp. 25–28, IEEE, 2010.

[153] ACAM, "The TDC cookbook." `http://www.acam.de/`.

[154] Q. Rong, X. Huang, and F. Tan, "Analysis and measurement of jitter in crystal oscillator," in *Proc. Int. Conf. on Communications, Circuits and Systems*, vol. 2, IEEE, 2005.